UNIVERSITY OF ROCHESTER
LABORATORY FOR LASER ENERGETICS

Volume 101
October—December 2004
DOE/SF/19460-589

LLE Review

Quarterly Report

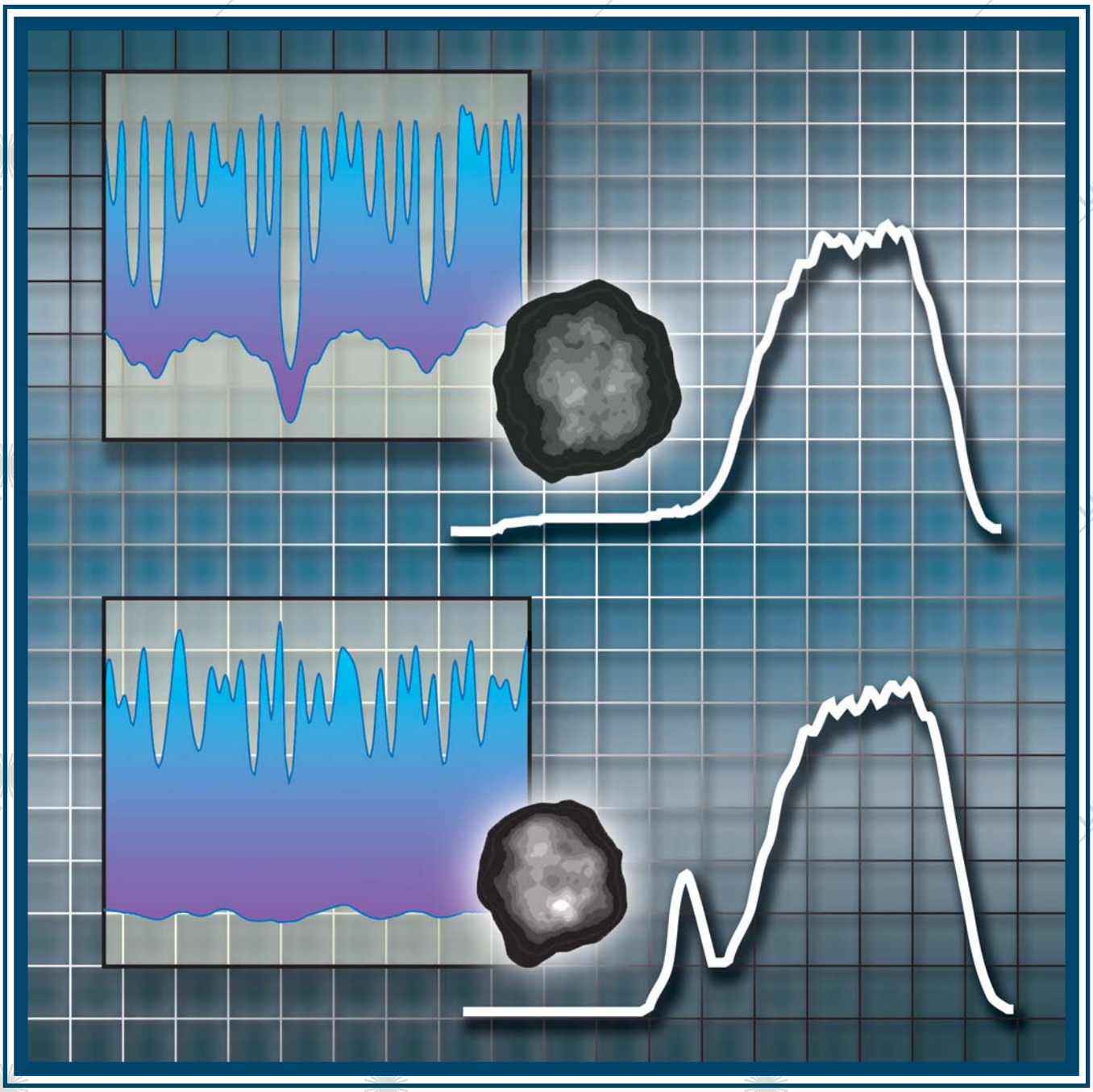

About the Cover:

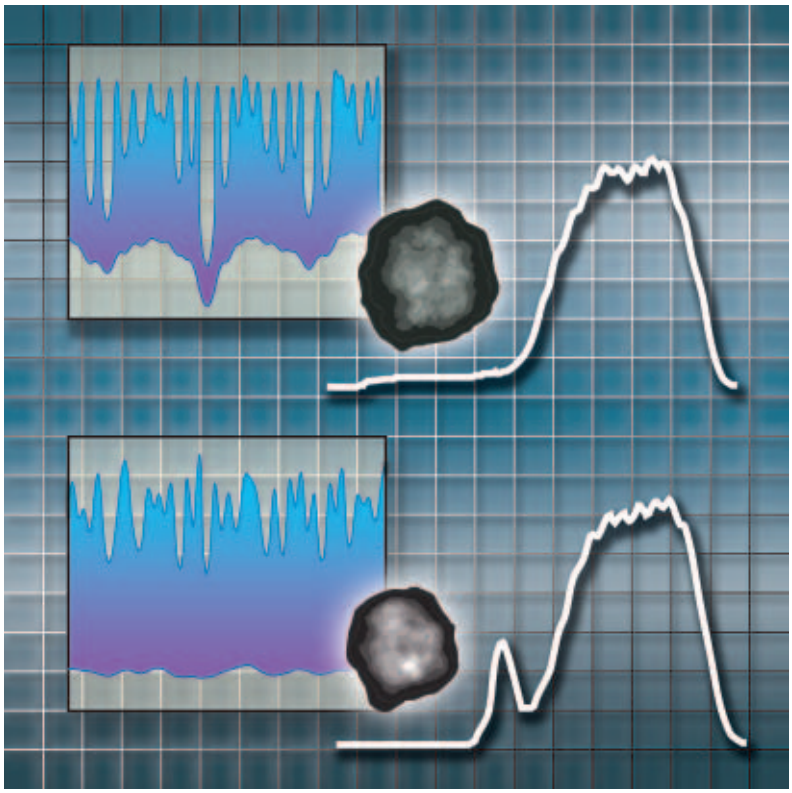

Both experiment and theory indicate that shaped adiabats improve the hydrodynamic stability and the performance of directly driven inertial confinement fusion (ICF) capsules. Pickets preceding the main target drive pulse increase and shape the ablator adiabat. The front cover compares the x-ray images of two capsules at peak compression for a laser pulse with and without a picket. The corresponding hydrodynamic simulations for these two cases are provided in the inset. It is evident that targets compressed by pulses prefaced with a picket exhibit reduced ablation-interface Rayleigh–Taylor seed and growth rate. Additionally, these targets exhibit higher compression and larger fusion yields from fusion reactions compared to the case of a pulse without a picket.

The work described in this volume includes current research at the Laboratory for Laser Energetics, which is supported by New York State Energy Research and Development Authority, the University of Rochester, the U.S. Department of Energy Office of Inertial Confinement Fusion under Cooperative Agreement No. DE-FC03-92SF19460, and other agencies.

Printed in the United States of America
Available from
National Technical Information Services
U.S. Department of Commerce
5285 Port Royal Road
Springfield, VA 22161

Price codes: Printed Copy A04
Microfiche A01

For questions or comments, contact Walter T. Shmayda, *Editor*, Laboratory for Laser Energetics, 250 East River Road, Rochester, NY 14623-1299, (585) 275-5769.

Worldwide-Web Home Page: http://www.lle.rochester.edu/

UNIVERSITY OF ROCHESTER
LABORATORY FOR LASER ENERGETICS

Volume 101
October–December 2004
DOE/SF/19460-589

LLE Review

Quarterly Report

UR LLE

Contents

In Brief

This volume of the LLE Review, covering October–December 2004, highlights, in the first two articles, the significance of shaped adiabats to inertial confinement fusion. In the first article (p. 1), R. Betti, K. Anderson, J. P. Knauer, T. J. B. Collins, R. L. McCrory, P. W. McKenty, and S. Skupsky demonstrate that inertial confinement fusion (ICF) capsules with shaped adiabats are expected to exhibit improved hydrodynamic stability without compromising the one-dimensional performances exhibited by flat-adiabat shells. Although the theoretical formulas for the adiabat profiles generated by the relaxation method of adiabat shaping have been previously derived in LLE Rev. 98 (pp. 106–121), the formulas presented in this article are simplified to power-law expressions. Simulations show good agreement with these power-law and pulse design formulas.

In the second article (p. 13), J. P. Knauer, K. Anderson, R. Betti, T. J. B. Collins, V. N. Goncharov, P. W. McKenty, D. D. Meyerhofer, P. B. Radha, S. P. Regan, T. C. Sangster, and V. A. Smalyuk along with J. A. Frenje, C. K. Li, R. D. Petrasso, and F. H. Séguin of the Plasma Fusion Center at MIT demonstrate experimentally that target stability improves when picket pulses are used to increase and shape the ablator adiabat. Hydrodynamic simulations show that a picket pulse preceding the main target drive pulse in a direct-drive ICF implosion can reduce both the ablation interface RT seed and the growth rate by increasing the adiabat while maintaining the low adiabat in the inner fuel layer for optimal target compression and a minimal drive energy for ignition. Experiments show that the Rayleigh–Taylor (RT) growth of nonuniformities is suppressed in both planar and spherical targets with picket-pulse laser illumination. Two types of picket pulses—a "decaying-shock-wave picket" and a "relaxation" picket—are used to shape the adiabat in spherical targets. Planar growth measurements using a wide, intense picket to raise the adiabat of a CH foil showed that the growth of short-wavelength perturbations was reduced, and even stabilized, by adjusting the intensity of the picket. Planar imprint experiments showed the expected reduction of imprinting when a picket pulse is used. The data show that the imprint level is reduced when a picket is added and, for short wavelengths, is as effective as 1-D, 1.5-Å SSD. A series of implosion experiments with a 130-ps-wide picket pulse showed a clear improvement in the performance of direct-drive implosions when the picket pulse was added to the drive pulse. Results from relaxation-picket implosions show larger yields from fusion reactions when the picket drive is used. These adiabat-shaping concepts make the likelihood of achieving ignition with direct-drive implosions on the National Ignition Facility significantly more probable.

Additional research developments presented in this issue include the following:

- S. Papernov and A. W. Schmid (p. 23) demonstrate that crater formation in SiO_2 thin films containing artificial defects by UV-pulsed-laser irradiation depends on the lodging depth of the defects. At laser fluences close to the crater-formation threshold and for lodging depths of a few particle diameters, the dominating material-removal mechanism is melting and evaporation. For absorbing defects lodged deeper than ~10 particle diameters, however, a two-stage material-removal mechanism occurs. The process starts with the material melting within the narrow channel volume, and, upon temperature and pressure buildup, film fracture takes place.

- I. A. Kozhinova, H. J. Romanofsky, A. Maltsev, and S. D. Jacobs along with W. I. Kordonski and S. R. Gorodkin of QED Technologies, Inc. (p. 35) discuss the polishing performance of magnetorheological (MR) fluids prepared with a variety of magnetic and non-magnetic ingredients to minimize artifact formation on the surface of CVD ZnS flats. Their results show that altering the fluid composition greatly improves smoothing performance of magnetorheological finishing (MRF). Nanoalumina abrasive used with soft carbonyl iron and altered MR fluid chemistry yield surfaces with roughness that do not exceed 20 nm p–v and 2-nm rms after removing 2 μm of material. Significantly, the formation of "orange peel" and the exposure of "pebble-like" structure inherent in ZnS from the CVD process is suppressed.

- W. R. Donaldson, M. Millecchia, and R. Keck (p. 43) designed and tested a 63-channel, high-resolution, ultraviolet (UV) spectrometer that can be used to check the tuning state of the KDP triplers. The spectrometer accepts an input energy of 1 μJ per channel, has a dispersion at the detector plane of 8.6×10^{-2} picometers (pm)/μm, and has a spectral window of 2.4 nanometers (nm) at $\lambda = 351$ nm. The wavelength resolution varies from 2.5 pm at the center of the field of view to 6 pm at the edge.

- A. Korneev, V. Matvienko, O. Minaeva, I. Milostnaya, I. Rubtsova, G. Chulkova, K. Smirnov, V. Voronov, G. Gol'tsman, W. Slysz, A. Pearlman, A. Verevkin, and R. Sobolewski (p. 49) discuss their studies on the quantum efficiency (QE) and the noise equivalent power (NEP) of the latest-generation, nanostructured NbN, superconducting, single-photon detectors (SSPD's) operated at temperatures in the 2.0- to 4.2-K range in the wavelength range from 0.5 to 5.6 μm. The detectors are designed as 4-nm-thick, 100-nm-wide NbN meander-shaped stripes, patterned by electron-beam lithography. Their active area is 10×10 μm^2. The best-achieved QE at 2.0 K for 1.55-μm photons is 17%, and the QE for 1.3-μm infrared photons reaches its saturation value of ~30%. The SSPD NEP at 2.0 K is as low as 5×10^{-21} W/Hz$^{-1/2}$. These SSPD's, operated at 2.0 K, significantly outperform their semiconducting counterparts. Together with their GHz counting rate and picosecond timing jitter, they are the devices-of-choice for practical quantum key distribution systems and quantum optical communications.

- B. Yaakobi, C. Stoeckl, W. Seka, T. C. Sangster, and D. D. Meyerhofer (p. 54) report the first measurements of electron preheat in direct-drive laser implosions of cryogenic deuterium targets. Preheat due to fast electrons generated by nonlinear laser–plasma interactions can reduce the gain in laser-imploded fusion targets. The preheat level is derived directly from the measured hard-x-ray spectrum. The fraction of the incident laser energy that preheats the deuterium fuel is found to be less than 0.1%, suggesting that the preheat will have a negligible impact on target performance. These results are encouraging for the success of the planned high-gain, direct-drive-ignition experiments planned on the National Ignition Facility.

Walter T. Shmayda
Editor

Pulse Design for Relaxation Adiabat-Shaped Targets in Inertial Fusion Implosions

Introduction

Controlling the seeds and the growth of Rayleigh–Taylor (RT) instability during the acceleration phase of imploding shells is crucial to the success of inertial confinement fusion (ICF). Since the RT growth is damped by the ablative flow off the shell's outer surface, target performances are greatly improved by target designs with enhanced ablation velocity. A significant increase in ablation velocity and shell stability can be achieved by shaping the entropy inside the shell. Following the standard ICF notation, we measure the entropy through the so-called "adiabat" defined as the ratio of the plasma pressure to the Fermi-degenerate DT pressure: $\alpha \equiv P(\mathrm{Mb})/2.18\rho(\mathrm{g/cc})^{5/3}$, where the pressure is given in megabars and the density in g/cc. The optimum adiabat shape in the shell consists of a profile that is monotonically decreasing from the outer to the inner surface as qualitatively shown in Fig. 101.8 on p. 14. Large adiabat values on the shell's outer surface increase the ablation velocity V_a, which follows a power law of the outer-surface adiabat α_{out}, $\left[V_a \sim \alpha_{\mathrm{out}}^{3/5}\right]$, while low adiabat values on the inner surface lead to improved ignition conditions and larger burn.[1–5] A more detailed history and target design implications of adiabat shaping can be found in the introduction of Ref. 6 by the same authors, which is devoted mostly to the adiabat shape induced by a strong decaying shock. Shaping by a decaying shock was introduced in Ref. 7 and requires a very strong prepulse aimed at launching a strong shock. This strong shock decays inside the shell shortly after the prepulse is turned off; the picket pulse is followed by the low-intensity foot of the main pulse. The decaying shock (DS) leaves behind a monotonically decreasing adiabat profile, which follows a power law of the mass coordinate

$$\alpha_{\mathrm{DS}} = \alpha_{\mathrm{inn}}\left(\frac{m_{\mathrm{shell}}}{m}\right)^{\delta_{\mathrm{DS}}}, \qquad (1)$$

where m is the mass calculated from the outer surface, m_{shell} is the total shell mass, and α_{inn} is the adiabat on the shell's inner surface. The value of δ_{DS}, calculated in Ref. 6, is approximately independent of the prepulse characteristics. Without accounting for the effect of mass ablation, δ_{DS} is about 1.3. If mass ablation is included, δ_{DS} varies between 1.06 and 1.13, depending on the prepulse duration.[6] Two-dimensional (2-D) simulations[7] of all-DT, OMEGA-size-capsule implosions have confirmed that DS adiabat targets exhibit significantly reduced RT growth on the ablation surface during the acceleration phase with respect to the flat-adiabat ones. Comparisons between flat- and shaped-adiabat targets are typically carried out by designing the flat- and shaped-adiabat pulses to generate identical adiabats on the shell's inner surface.

A different technique aimed at shaping the adiabat is the so-called shaping by relaxation (or RX shaping) first introduced in Ref. 8. The relaxation technique uses a less-energetic prepulse than the DS technique. The RX prepulse (Fig. 101.1) is used to launch a shock that may or may not decay inside the shell. In both cases, the prepulse is turned off before the prepulse shock reaches the shell's inner surface. Since the prepulse is followed by a complete power shutoff, the outer portion of the shell expands outward, generating a relaxed density profile while the prepulse shock travels inside the shell. The prepulse shock is not intended to greatly change the shell adiabat even though

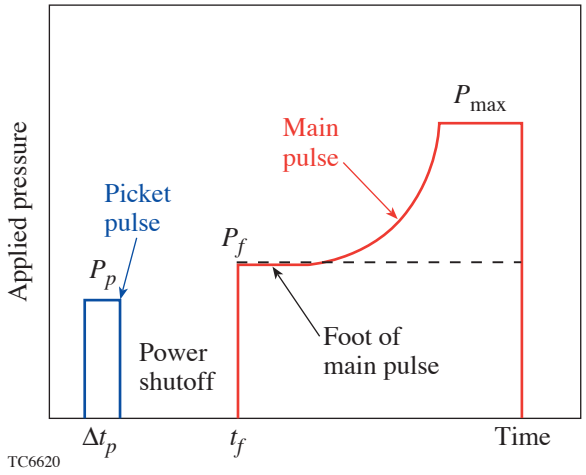

Figure 101.1
Typical pressure pulse for adiabat shaping by relaxation.

it may cause a significant adiabat modification. The main adiabat shaping occurs later in time when the foot of the main pulse starts and a strong shock travels up the relaxed density profile. The main shock first encounters the low-density portion of the relaxed profile, setting it on a very high adiabat. The adiabat develops a monotonically decreasing profile as a result of the increasing pre-shock density. Figures 101.2(a), 101.2(b), and 101.2(c) show three snapshots of the main shock propagation (m.s.) through a relaxed density profile. The density profile of an 85-μm-thick DT target is relaxed by a 60-ps, 13-Mb prepulse. The prepulse shock (p.s.) travels ahead of the main pulse shock. The latter is launched by a 15-Mb pressure applied at 1941 ps. The main shock launching time (or main pulse foot beginning time) is chosen in order to cause the main and prepulse shocks to merge on the shell's inner surface. A plot of the shaped-adiabat profile at shock breakout is shown in Fig. 101.2(d). Observe that the adiabat varies from about 2 on the inner surface to several tens on the outer surface. Two-dimensional (2-D) simulations[8–10] of OMEGA- and NIF-size-capsule implosions have confirmed that RX-shaped targets exhibit significantly reduced RT growth on the ablation surface during the acceleration phase with respect to the flat-adiabat ones.

The RX adiabat-shaping technique can be viewed as a two-step process: the prepulse and power shutoff are needed to generate the relaxed density profile, while the foot of the main pulse shapes the adiabat. Similarly to the DS shaping, the RX adiabat profile can be approximated with a power law of the mass coordinate

$$\alpha_{RX} \simeq \alpha_{inn}\left(\frac{m_{shell}}{m}\right)^{\delta_{RX}}, \qquad (2)$$

where δ_{RX} can be tailored between a minimum of zero (i.e., no shaping) to a maximum value of 2.4. This upper bound, which is well above the decaying shock value, can be achieved only for weak prepulses (either low-pressure or short-duration prepulses) and by neglecting the effects of mass ablation. For realistic prepulses and including the effect of ablation, the maximum RX power index is reduced to values in the range of 1.6 to 1.8, which is still significantly larger than the 1.1 of the decaying shock. Since the steeper RX adiabat profile leads to greater values of the outer-surface adiabat with respect to the DS adiabat shaping, one can conclude that the ablation velocity will be significantly higher in RX-shaped targets than DS-shaped targets. Furthermore, the tailoring of the adiabat steepness in RX shaping is beneficial to the control of the convective instability, which is driven by the finite entropy gradients inside the shell. This instability grows at a slower rate with respect to the Rayleigh–Taylor and does not seem to cause a significant distortion of the shell.[7,8]

Different adiabat-shaping techniques based on the tailoring of the radiation absorption in the target have also been proposed;[11–13] however, their implementation relies on manufacturing targets with a spatially varying atomic number, a technique that is difficult in cryogenic capsules. It has also been suggested[14] that some classified work on adiabat shaping was initiated in the 1980s by Verdon, Haan, and Tabak. This work

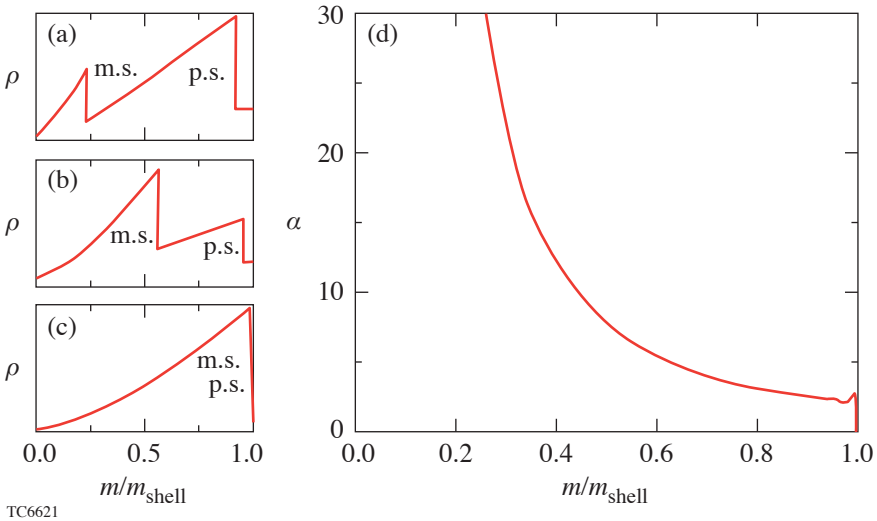

Figure 101.2
Snapshots [(a),(b), and (c)] of the density profiles at different stages of the main-shock and prepulse-shock propagation. The resulting adiabat profile left behind the main shock at breakout time is shown in (d).

appears to be restricted, however, to the classified literature and was not accessible to Betti and Anderson (authors of the earlier published work[8] on RX shaping and co-authors of the current article). It is also important to clarify the role of earlier work[15] on the so-called "picket-fence" pulses and make a distinction between adiabat shaping and picket fence. The picket-fence pulse consists of a sequence of relatively short pulses that replace the standard isentropic continuous pulse. When plotted versus time, the laser power of such a sequence of short pulses (see Fig. 3 of Ref. 15) resembles a picket fence. Instead, both DS adiabat shaping and RX adiabat shaping make use of a single short pulse (i.e., the laser prepulse) followed by a continuous pulse. Thus, except for the prepulse, the adiabat-shaping pulses are essentially continuous. While a claim can be made that adiabat shaping and picket fence use some sort of picket pulse, it would be grossly inaccurate to think of the two techniques as equal or even similar. As stated in Ref. 15, the goal of the picket-fence pulse is to replace a continuous acceleration with an impulsive one. The rationale behind this clever idea is that the RT exponential growth turns into a sequence of linear-growth stages, thus reducing the overall growth factor (as long as the number of pickets is kept relatively low). On the contrary, adiabat shaping does not change the time evolution of the acceleration. Its primary effect is to increase the ablation velocity, thus enhancing the ablative stabilization of the RT instability. Though the physical basis and pulse design of a picket-fence pulse have little (if anything) in common with adiabat shaping, it is possible that some level of adiabat shaping may occur in picket-fence implosions due to the repeated decompressions between short pulses. Though this collateral effect was not considered in Ref. 15, it would be worth investigating the degree at which the adiabat is shaped in picket-fence implosions. It is also worth mentioning that the evolution of the laser power in Fig. 2 of Ref. 15 seems to point to a single prepulse followed by a continuous main pulse. While this pulse resembles an RX pulse, the authors of Ref. 15 do not address the possibility that adiabat shaping may occur.

Lastly, it is important to recognize that the presence of a laser prepulse could have significant consequences with regard to the level of laser imprinting. Laser imprinting is caused by the spatial nonuniformities of the laser intensity and is widely considered as the main seed for the short-wavelength RT instability in direct-drive implosions. It has been recently shown[16–18] that the level of imprinting can be significantly reduced by tailoring the initial target density with a monotonically increasing profile varying from a lower value on the outer surface to its maximum on the shell's inner surface. Since the laser prepulse in RX adiabat shaping causes such a monotonically varying density profile, it is likely that RX shaping may also reduce the level of imprinting. Furthermore, it has been shown in Ref. 19 that, in the presence of a plastic (or other) coating on cryogenic capsules, the acceleration of the plastic layer against the cryogenic DT layer causes a brief exponential amplification of the imprinting level. Reference 19 also shows that this amplification can be reduced by using a sufficiently strong prepulse. Such an improvement of the imprinted nonuniformities requires a strong prepulse and may therefore be more effective in DS shaping than in RX shaping. Imprint reduction using prepulses has also been demonstrated by both simulation and experiment in single-layer targets made of aluminum.[20] While some encouraging results on the stability of RX-shaped capsule implosions have been obtained from 2-D simulations[8–10] and from experiments on plastic-shell implosions,[10] a more detailed 2-D analysis including the effect of RX shaping on imprinting as well as a complete description of the experiments carried out on the OMEGA laser system will be presented in a forthcoming publication.

In this article, we cite the results of the one-dimensional (1-D) hydrodynamic analysis of the relaxation adiabat profiles,[21,22] simplify them with power-law approximations, and compare them with decaying-shock-adiabat profiles and to simulations. Furthermore, we derive formulas for relaxation pulse design and discuss nonideal effects, such as mass ablation, on the adiabat profiles.

Summary of Previously Derived Adiabat Profiles

References 21 and 22 divide relaxation adiabat shaping designs into two categories: type 1, where the prepulse shock and rarefaction merge at the rear surface of the shell; and type 2, where the rarefaction merges with the prepulse shock within the shell. These two designs yield different adiabat profiles. An accurate description of the type-1 adiabat profile is well approximated by the following set of equations from Eqs. (75)–(77) and (46b), respectively, of Ref. 22:

$$S = S_{\text{inn}}\left(\frac{m_{\text{shell}}}{m}\right)^{\frac{2\gamma}{\gamma+1}} \frac{\chi(1)}{\chi\left(\dfrac{m}{m_{\text{shell}}}\right)}, \tag{3}$$

where

$$S_{\text{inn}} = \frac{(\gamma-1)^{2\gamma}}{\gamma\chi(1)(\gamma+1)^{2\gamma-1}}\frac{P_f}{\rho_0^{\gamma}} \tag{4}$$

is the entropy on the shell's inner surface and ρ_0 is the initial shell density. The function $\chi(x)$ represents the corrections due to the finite main shock strength

$$\chi(x)=\tilde{\rho}\left\{\frac{\gamma P_p\Theta(x)}{(\gamma+1)P_f}\left[\frac{x}{\sum(x)}\right]^{\frac{2\gamma}{\gamma+1}}\right\}^{\gamma}\frac{\Theta(x)}{\sum(x)^{\frac{2\gamma}{\gamma+1}}}, \quad (5)$$

$$\tilde{\rho}(\hat{\pi})=\frac{1+\frac{\gamma-1}{\gamma+1}\hat{\pi}}{1+\frac{\gamma+1}{\gamma-1}\hat{\pi}}\simeq 1-\frac{4\gamma}{\gamma^2-1}\hat{\pi}+\mathcal{O}\left(\hat{\pi}^2\right), \quad (6)$$

and where $\beta\simeq 2/(\gamma+1)$ and $\hat{\pi}=P_p/P_f$ is the ratio of the prepulse pressure to the pressure of the foot of the main pulse.

The type-2 adiabat profiles are steeper than the type-1 profiles and can be approximated as

$$S(m)\simeq\frac{\omega_* P_f}{\rho_M^{\gamma}}\left(\frac{z_{\text{shell}}}{z}\right)^{\gamma\mu}\left[1+D(z)(z-1)\right]\hat{s}(z), \quad (7)$$

$$\hat{s}(z)=\frac{\left\{1-\phi\hat{m}_*^{\phi}\sqrt{\frac{2(\gamma-1)}{(\gamma+1)\omega_*}\frac{P_p}{P_f}}\left[\sigma(z_{\text{shell}})-\sigma(z)\right]\right\}^{\frac{\gamma\mu}{\phi}}}{\left\{\tilde{\rho}\left[\frac{P_p}{\omega_* P_f}\frac{\hat{m}_*^{\mu\gamma}z^{\mu\gamma-\delta}}{1+D_0(z)(z-1)}\right]\right\}^{\gamma}}, \quad (8)$$

$$\omega_*=\omega_0\left[1-\frac{2\beta(\gamma+2)}{3(2-\beta)}\sqrt{\frac{2\gamma P_p}{\omega_0(\gamma+1)P_f}}\left(\frac{m_*}{m_{\text{rf}}^0}\right)^{1-\frac{\beta}{2}}\right], \quad (9)$$

where $D(x)=D_0(x)+D_1(x)$,

$$D_0(x)=\frac{2\left(x^{\mu}-1\right)+\mu(x-3)(x-1)-\mu^2(x-1)^2}{(\mu-2)(\mu-1)(x-1)^3}, \quad (10)$$

$$D_1(x)=-\mu\sqrt{\frac{\gamma-1}{\gamma+1}\frac{P_p}{\omega_* P_f}}\frac{\hat{m}_*^{\phi}\left(z_s^M\right)^{\mu}}{\left(z_s^M-1\right)^3}\times\int_1^{z_s^M}\sqrt{\frac{(x-1)^4+D_0(x)(x-1)^5}{x^{3\mu}}}dx, \quad (11)$$

and $\tilde{\rho}(x)$ is given by Eq. (6). These formulas are derived in Ref. 22 as Eqs. (100a), (100b), (90), (82), and (94), respectively.

In practical terms, these formulas for the relaxation-adiabat profiles are cumbersome and provide no intuitive comparison with decaying-shock-adiabat profiles. Therefore, in the following section, simple power-law approximations to these formulas are calculated.

Simplified Formulas for RX Adiabat Shapes and Comparison with DS Shapes

The theoretical results derived in the previous section can be simplified by fitting the adiabat shapes with a simple power law in the mass coordinate. It has been shown in Ref. 6 that the power-law approximation works extremely well for the adiabat shape left behind by a decaying shock (DS shaping). In an ideal fluid with adiabatic index $\gamma = 5/3$ and neglecting the effects of mass ablation, the adiabat profile left behind by a decaying shock follows the power law $\alpha_{\text{DS}}\sim 1/m^{1.315}$ for $m_* < m < 10\,m_*$. It is worth mentioning that the power index is approximately independent of the prepulse characteristics.

Adiabat shaping by relaxation leads to a tunable adiabat profile ranging from a rather shallow profile for RX shaping of type 1 to a steeper profile with RX shaping of type 2. In the case of RX shaping of type 1, the shaping function given in Eqs. (3)–(5) can be well approximated for $\gamma = 5/3$ by the following power law of the mass coordinate:

$$\alpha_{\text{RX1}}=\alpha_{\text{inn}}^{\text{RX1}}\left(\frac{m_{\text{shell}}}{m}\right)^{\delta_{\text{RX1}}}, \quad (12)$$

where the power index δ_{RX1} and the inner-surface adiabat $\alpha_{\text{inn}}^{\text{RX1}}$ are functions of prepulse/main-pulse pressure ratio $r_p\equiv P_p/P_f$. A straightforward numerical fit leads to the following fitting functions:

$$\alpha_{\text{inn}}^{\text{RX1}} \simeq 7.2\cdot 10^{-3}\,\frac{P_f(\text{Mb})}{\rho_0(\text{g/cc})^{5/3}} \times\left(1-1.12r_p^{0.52}+6.54r_p^{1.15}\right), \tag{13}$$

$$\delta_{\text{RX1}} \simeq 1.25-4.14r_p^{0.95}+3.05r_p^{1.61}, \tag{14}$$

where ρ_0 is the initial shell density. These approximate formulas have been derived by fitting the adiabat profile over the range $0.2 < m/m_{\text{shell}} < 1$ and $0 < r_p < 0.75$. Observe that the steepest profile of the first kind behaves as $1/m^{1.25}$ and occurs for $r_p \to 0$. For typical values of prepulse- to foot-pressure ratios in the range $0.05 < r_p < 0.2$, the power index of the adiabat profile is within the range 0.60 to 1.04, which is well below the decaying shock value of 1.315, thus indicating that the DS shaping leads to notably steeper adiabat profiles than the relaxation method of type 1.

In RX shaping of type 2, the adiabat profile left behind by the main shock [Eqs. (7)–(11)] can also be approximated by a power law of the mass coordinate

$$\alpha_{\text{RX2}} \simeq \alpha_{\text{inn}}^{\text{RX2}}\left(\frac{m_{\text{shell}}}{m}\right)^{\delta_{\text{RX2}}}, \tag{15}$$

where

$$\alpha_{\text{inn}}^{\text{RX2}} = 2.46\cdot 10^{-2}\,\frac{P_f(\text{Mb})}{\rho_0(\text{g/cc})^{5/3}} \times\left(1.19+1.76r_p^{0.8}\hat{m}_*^{2.15}-1.11\hat{m}_*^{0.25}\right), \tag{16}$$

$$\delta_{\text{RX2}} \simeq 2.105-3.469r_p^{0.62}\hat{m}_*^{1.31}, \tag{17}$$

and where $m_* = 2.09\Delta t_p\sqrt{P_p\rho_0}$, Δt_p is the prepulse duration, and $m_{\text{shell}} = \rho_0 d_0$ (d_0 is the initial shell thickness). It is important to emphasize that Eqs. (15)–(17) have been derived by fitting Eqs. (7)–(11) for an ideal fluid (no ablation) with γ= 5/3 and pulse/target characteristics satisfying $0.2 < r_p < 1$ and $0.05 < \hat{m}_* < 0.4$. It is also interesting to note that the power index δ_{RX2} is maximum for short prepulses and/or weak prepulses $\left(\hat{m}_* << 1,\ r_p << 1\right)$. For $\hat{m}_* \to 0$, the RX adiabat profile of Eqs. (7)–(11) reduces to a power law with a power index $\delta_{\text{RX2}} \simeq 2.4$, well above the power index of the decaying shock shaping $\delta_{\text{DS}} \simeq 1.315$. However, the ratio m_*/m_{shell} cannot be arbitrarily small for RX shaping since the pressure behind the prepulse shock at its arrival on the inner surface, which is approximately $P_p\hat{m}_*^{1.3}$, must be large enough to keep the prepulse shock in the strong shock regime and to ionize the target material. Typical values of δ_{RX2} are mostly in the range 1.7 to 2.0, which is still significantly larger than the 1.315 of the decaying shock.

It has been shown in Ref. 6 that ablation causes the adiabat profile induced by a decaying shock to become shallower. This is because the shock decays more slowly due to the residual ablation pressure and the fact that the supporting pressure moves closer to the shock. In the relaxation method of type 2, the relaxed density profile is produced by a decaying shock driven by the pressure prepulse. Since ablation causes a slowdown of the shock decay, it follows that the relaxed profile is "less relaxed" because of ablation. Therefore, the adiabat shape induced by the main shock is less steep than in the ideal case without ablation. Typical ablation-induced reductions of the adiabat profile power index δ_{RX} are small (of the order of 10%) and lead to a power index in the range $\delta_{\text{RX2}} \simeq 1.6$ to 1.8.

Pulse Design

To induce the desired adiabat profile, one needs to design the appropriate applied pressure pulse. The pressure pulse (Fig. 101.1) consists of a constant prepulse of pressure P_p and duration Δt_p followed by a main pulse of pressure P_f applied at time t_f. Typically, the pulse is designed to induce the desired value of the inner-surface adiabat α_{inn}. The latter is a design parameter that needs to satisfy the one-dimensional ignition and gain requirements of the implosion. Another design constraint is the merging of the prepulse and main shocks on the shell's inner surface. This is required in order to keep the adiabat profile monotonically decreasing. For the relaxation pulse of type 1, another requirement is the merging of the rarefaction wave with the prepulse and main shocks on the shell's inner surface. Therefore, given the four pulse parameters (P_p, P_f, Δt_p, and t_f), the type-1 relaxation has three constraints and one free parameter, while the type-2 relaxation has two constraints and two free parameters. Since different pulse parameters lead to different adiabat decay rates, another design parameter can be identified as the adiabat profile's spatial decay rate. By approximating the adiabat profile with a power law $S \sim 1/m^{\Delta}$, the power index Δ defines the decay

rate and can be assigned as a design parameter (within the appropriate limits), thus further reducing the degrees of freedom. Furthermore, technical limits on the prepulse and foot pressure as well as prepulse duration are imposed by the pulse-shaping capabilities of a given laser system. Such limitations are not discussed in this article but need to be taken into account when designing an adiabat-shaping pulse. In this section we proceed to determine the relevant parameters needed to design a pressure pulse for RX adiabat shaping.

1. Pulse Design for RX Shaping of Type 1

The pulse design for a relaxation shaping of type 1 is highly constrained since the prepulse shock, the rarefaction wave, and the main shock must all merge on the shell's rear surface. By combining the Hugoniot condition on the shock velocity

$$\dot{m}_s^M = \sqrt{(\gamma+1)P_{\rm ps}\rho_{\rm bs}/2},$$

the type-1 post-main-shock pressure from Eqs. (73) of Ref. 22

$$P_{\rm ps}^M = P_M/\Theta(\eta_s), \tag{18a}$$

$$\Theta(x) = 1+\frac{2\beta(\gamma+2)}{3(2-\beta)}\sqrt{\frac{2\gamma P_p}{(\gamma+1)P_M}}\,x^{1-\frac{\beta}{2}}, \tag{18b}$$

and the pre-shock density $\rho_{\rm bs}^M = \rho_p\left(m_s^M/m_{\rm rf}\right)^\beta$, with $m_{\rm rf} = m_{\rm shell}\tau$ and

$$\tau = t/\Delta t_*, \tag{19}$$

$$\Delta t_* = \frac{\Delta t_p}{\sqrt{2\gamma/(\gamma-1)}-1} \tag{20}$$

from Eqs. (12)–(13) of Ref. 22, one can easily derive the following ordinary differential equation for the main-shock propagation:

$$\frac{d\eta_s^M}{d\tau} = \frac{\gamma+1}{\gamma}\sqrt{\frac{P_f}{2P_p\Theta\left(\eta_s^M\right)}\left(\frac{\eta_s^M}{\tau}\right)^\beta}, \tag{21}$$

where $\eta_s^M = m/m_{\rm shell}$ and Θ is derived from Eq. (18b) for $\beta = 2/(\gamma+1)$, leading to

$$\Theta = 1+\frac{2(\gamma+2)}{3(\gamma+1)}\sqrt{\frac{2P_p}{P_f}}\left(\eta_s^M\right)^{\frac{\gamma}{\gamma+1}}. \tag{22}$$

A straightforward integration of Eq. (21) for $\eta_s^M \in [0,1]$ and $\tau \in [\tau_f, 1]$ leads to the following expression for the beginning time of the foot pulse:

$$t_f = \Delta t_p + \tau_f \Delta t_*, \tag{23a}$$

$$\tau_f = \left\{1-\frac{\gamma}{\gamma+1}\sqrt{\frac{2P_p}{P_f}}\left[1+\frac{\gamma+2}{6(\gamma+1)}\sqrt{\frac{2P_p}{P_f}}\right]\right\}^{\frac{\gamma+1}{\gamma}}, \tag{23b}$$

where Δt_* is proportional to the prepulse duration Δt_p through Eq. (20). The main-shock breakout time coincides with the prepulse shock and rarefaction-wave breakout time on the inner surface given by the simple relation

$$t_{\rm b.o.} = \Delta t_p + \Delta t_*. \tag{24}$$

The inner-surface adiabat induced by such a pulse is given by Eq. (13) and is primarily dependent on the foot pressure. If the inner-surface adiabat is an assigned design parameter, then Eq. (13) is used to constrain the foot pressure P_f. Note that the prepulse pressure and duration are related by the rarefaction wave/prepulse shock overtaking time, $m_* = m_{\rm shell} \equiv \rho_0 d_0$ or

$$\Delta t_p\sqrt{P_p} = \sqrt{\rho_0}\,d_0\,\frac{\sqrt{2\gamma}-\sqrt{\gamma-1}}{\sqrt{\gamma(\gamma+1)}}. \tag{25}$$

It follows that, for an assigned prepulse pressure (or duration) and inner-surface adiabat, there is only one foot pressure that would shape the adiabat with a profile of type 1 [Eqs. (12)–(14)]. As an example, we consider a 100-μm-thick DT shell ($\rho_0 = 0.25$ g/cc, $d_0 = 100$ μm) and design a type-1 RX shaping pulse using a prepulse given by $P_p = 5$ Mb, requiring an inner-surface adiabat $\alpha_{\rm inn} \simeq 3$. Equation (25) yields a prepulse duration of $\Delta t_p \simeq 1070$ ps, while the foot pressure can be determined from Eq. (13) by setting $\alpha_{\rm inn} = 3$. A straightforward calculation yields the foot pressure $P_f \simeq 29.7$ Mb. The foot pressure is applied at the time t_f obtained from Eq. (23),

yielding $t_f \simeq 1442$ ps. The shock-breakout time on the inner surface is given by Eq. (24), yielding $t_{\text{b.o.}} \simeq 1936$ ps. The corresponding adiabat profile has an approximate power-law behavior [Eq. (12)] with power index $\delta_{\text{RX1}} \simeq 0.67$ given by Eq. (14). Observe that Eq. (23b) suggests that a critical value of P_p/P_f exists that makes $\tau_f = 0$. Though such a critical value is not accurately predicted by the weak prepulse theory $\left(P_p << P_f\right)$ derived in this article, it is intuitive that an upper limit in the ratio P_p/P_f must exist in the design of a relaxation pulse of the first kind. Indeed, for a given prepulse pressure, the foot pressure must be sufficiently large to cause the main shock to catch the prepulse shock on the shell's rear surface.

2. Pulse Design Shaping for RX Shaping of Type 2

The shock-merging constraint requires that both the prepulse and the main shock merge at the rear surface. The prepulse-shock breakout time ($t_{\text{b.o.}}$) on the rear surface can be easily obtained from Eq. (32) of Ref. 22,

$$z_s^p(\tau) = \left[1 + \left(1 + \frac{\delta}{2}\right)\sqrt{\frac{\gamma - 1}{2\gamma}}(\tau - 1)\right]^{\frac{2}{2+\delta}}, \tag{26}$$

by setting $z_s^p = z_{\text{shell}} \equiv m_{\text{shell}}/m_*$, thus leading to

$$t_{\text{b.o.}} = \Delta t_p + \Delta t_* \tau_{\text{b.o.}}, \tag{27a}$$

$$\tau_{\text{b.o.}} \equiv 1 + \frac{2}{2+\delta}\sqrt{\frac{2\gamma}{\gamma - 1}}\left[z_{\text{shell}}^{(2+\delta)/2} - 1\right], \tag{27b}$$

where Δt_* is given in Eq. (20) and m_* in Eq. (14) of Ref. 22:

$$m_* = \Delta t_* \rho_p a_p = \Delta t_* \sqrt{\gamma P_p \rho_p}. \tag{28}$$

The main shock must also arrive on the rear surface at time $t_{\text{b.o.}}$ by traveling through the $m > m_*$ and $m < m_*$ regions. The main shock's traveling time through the $m > m_*$ region can be easily derived by integrating Eq. (91) of Ref. 22:

$$\dot{m}_s^M = \sqrt{\frac{\gamma - 1}{2}\omega_* P_f \rho_M \left(\frac{m_s^M}{m_s^p}\right)^{\mu}\left[1 + D\left(z_s^M\right)\left(z_s^M - 1\right)\right]}. \tag{29}$$

A straightforward manipulation yields the following traveling time:

$$\Delta t_{m>m_*}^M = \Delta t_* \Delta \tau_{m>m_*}^M, \tag{30a}$$

where

$$\Delta \tau_{m>m_*}^M = \sqrt{\frac{2\gamma}{\gamma + 1}\frac{P_p}{\omega_* P_f}} \times \int_1^{z_{\text{shell}}} \frac{\left(z_s^p\right)^{\mu/2} dz_s^M}{\sqrt{\left(z_s^M\right)^{\mu}\left[1 + D\left(z_s^M\right)\left(z_s^M - 1\right)\right]}}, \tag{30b}$$

z_s^p is a function of z_s^M [Eqs. (96)–(97) of Ref. 22],

$$\left(z_s^p\right)^{\phi} - z_{\text{shell}}^{\phi} = \phi\sqrt{\frac{2(\gamma - 1)}{\gamma + 1}\frac{P_p}{\omega_* P_f}}\left[\sigma\left(z_s^M\right) - \sigma\left(z_{\text{shell}}\right)\right], \tag{31}$$

where $z_s^p = m_s^p/m_*$, $z_{\text{shell}} = z_{\text{shell}} = m_{\text{shell}}/m_*$, and

$$\sigma(\xi) = \sqrt{\frac{(\mu - 2)\xi^{1-\mu} - (\mu - 1)\xi^{2-\mu} + 1}{(\mu - 2)(\mu - 1)}}, \tag{32}$$

and $D(x)$, ω_* are given in Eqs. (10), (11), and (9). It follows that the time when the main shock is at $m = m_*$ is $t_{m=m_*}^M = \Delta t_p + \Delta t_* \tau_{m=m_*}$, where $\tau_{m=m_*} \equiv \tau_{\text{b.o.}} - \Delta \tau_{m>m_*}^M$. Before arriving at m_*, the main shock travels through the region $0 < m < m_*$, where the density profile is given by Eq. (44) of Ref. 22,

$$\rho(z < 1) \approx \rho_p\left(\frac{z}{\tau}\right)^{\beta} = \rho_p\left(\frac{m}{m_{\text{rf}}}\right)^{\beta}, \tag{33}$$

and the post-shock pressure follows Eq. (18) with $\eta = m_s^M/m_{\text{rf}}^0$ and m_{rf}^0 given in Eq. (89) of Ref. 22,

$$m_{\rm rf}^0 = m_*\left\{1+\frac{2}{2+\delta}\sqrt{\frac{2\gamma}{\gamma-1}}\left[z_{\rm shell}^{(2+\delta)/2}-1\right]\right\}. \qquad (34)$$

The shock-evolution equation is given by the Hugoniot condition [Eq. (10) of Ref. 22]

$$\dot{m}_s = \sqrt{\frac{(\gamma+1)}{2}\left[P_{\rm ps}\rho_{\rm bs}\right]_{m_s}}, \qquad (35)$$

which can be integrated between the main-shock launching time (or main-pulse foot beginning time t_f) and the arrival time at $m = m_*$. A short calculation yields the launching time

$$t_f = \Delta t_* \tau_f + \Delta t_p, \qquad (36a)$$

$$\tau_f \equiv \left[\tau_{m=m_*}^{(2-\beta)/2} - \left(1-\frac{\beta}{2}\right)\theta\sqrt{\frac{2\gamma}{\gamma+1}\frac{P_p}{\omega_0 P_f}}\right]^{\frac{2}{2-\beta}}, \qquad (36b)$$

where

$$\theta = \int_0^1 dx \frac{1}{\chi^{\beta/2}}$$

$$\times\left[1-\frac{2\beta(\gamma+2)}{3(2-\beta)}\sqrt{\frac{2\gamma P_p}{(\gamma+1)\omega_0 P_f}}\left(\frac{xm_*}{m_{\rm rf}^0}\right)^{\frac{2-\beta}{\beta}}\right]^{-\frac{1}{2}}. \qquad (36c)$$

Observe that Eqs. 36 provide the beginning time of the foot of the main pulse once the prepulse pressure P_p, foot pressure P_f, and prepulse duration Δt_p are assigned. The time t_f is derived by timing the prepulse and main shock so that they merge on the shell's inner surface. As an example, we consider a 100-μm-thick DT shell (ρ_0 = 0.25 g/cc, d_0 = 100 μm) and design a type-2 RX shaping pulse using a P_p = 18 Mb, Δt_p = 100-ps prepulse and requiring an inner-surface adiabat $\alpha_{\rm inn} \simeq 3$. Using the definition $m_{\rm shell} = \rho_0 d_0$ and Eqs. (20) and (28) to find m_*, one can easily compute the parameter $\hat{m}_* = 0.177$. The foot pressure can be determined by using $\alpha_{\rm inn} = 3$ into Eq. (16), yielding $P_f \simeq 24$ Mb. The time when the foot pressure is applied can be computed from Eqs. (36) using $\gamma = 5/3$, $\omega_0 \simeq 1.5$, and $\beta = 0.75$, leading to t_f = 1256 ps. The shocks' breakout/merging time is determined through Eqs. (27), leading to $t_{\rm b.o.}$ = 1993 ps. The corresponding adiabat profile has an approximate power-law behavior [Eq. (15)] with power index $\delta_{\rm RX2} \simeq 1.80$, which is significantly larger than in the case of the decaying-shock shaping.

It is important to recognize that typical laser pulses are designed so that the laser power reaches its peak at shock breakout. The corresponding laser pressure starts from the foot level (P_f) and increases monotonically to its maximum value $P_{\rm max}$ (Fig. 101.1). The laser power (and pressure) is raised at a low-enough rate to avoid strengthening the main shock and to prevent increasing the adiabat after the main shock. Since the resulting adiabat shape is set by the main shock driven by P_f, the theory derived in this article is valid for realistic ICF pulses with a laser-power raise after the foot (Fig. 101.1).

This concludes the analysis of the pulse design. A detailed comparison of the adiabat shapes and pulse-design parameters with the results of numerical simulation is carried out in the next section.

Comparison with Simulations

The results of the analytic theory derived in this article are compared to the numerical results calculated by a one-dimensional Lagrangian hydrodynamics code, using ideal gas equation of state and an imposed pressure boundary condition to simulate the relaxation drive pulses. We have chosen the case of $\alpha_{\rm inn}$ = 3 as a case of interest, where adiabat shaping is expected to demonstrate significantly improved performance and to constrain our capsule and pulse designs to such as would be implementable on the OMEGA laser system.

Using the pulse-design formulas given in the **Pulse Design for RX Shaping of Type 1** section (p. 6), a type-1 RX pulse shape was designed for a typical OMEGA cryogenic capsule of density ρ_0 = 0.25 g/cm^3 and thickness d_0 = 100 μm using the parameters described in the example on pp. 6–7: P_p = 5 Mb, Δt_p = 1070 ps, P_f = 29.7 Mb, and t_f = 1442 ps. The shocks' breakout time is $t_{\rm b.o.}$ = 1936 ps, and the resulting adiabat shape can be approximated with the power law $\alpha \simeq 3.04\left(m_{\rm shell}/m\right)^{0.67}$. The pulse parameters have been used as input to the one-dimensional Lagrangian code that solves the equation of motion over a mesh of 2000 grid points. Figure 101.3 compares the adiabat profiles from the numerical simulation (solid curve) with the power-law approximation (dashed curve) and the full analytic formula in Eqs. (3)–(5) (dotted curve). Observe that the theoretical pulse parameters described on pp. 6–7 produce a monotonically decreasing adiabat profile with an inner-surface adiabat of about $\alpha_{\rm inn} \simeq 3$. Furthermore, the simulated adiabat profile compares favorably with the full

analytic formula as well as the power-law approximation described in the **Simplified Formulas for RX Adiabat Shapes and Comparison with DS Shapes** section (p. 4) for type-1 relaxation.

Similarly, a type-2 RX pulse shape is designed in the **Pulse Design for RX Shaping of Type 2** section (p. 7) for the same target with $\alpha_{inn} = 3$. The pulse parameters shown on p. 8 are $P_p = 18$ Mb, $P_f = 24$ Mb, $\Delta t_p = 100$ ps, and $t_f = 1256$ ps. The shocks' breakout time is $t_{b.o.} = 1993$ ps, and the adiabat profile can be approximated with the power law $\alpha \simeq 3.0\left(m_{shell}/m\right)^{1.8}$. Figure 101.4 compares the adiabat profiles from the numerical simulation (solid curve) with the power-law approximation (dashed curve) and the full analytic formula in Eqs. (7)–(11) (dotted curve). Observe that the theoretical pulse parameters (p. 8) induce a monotonically decreasing adiabat profile with an inner-surface adiabat of about $\alpha_{inn} \simeq 3$. Even in this case, the simulated adiabat profile compares favorably with both the full analytic formula as well as the power-law approximation for type-2 relaxation.

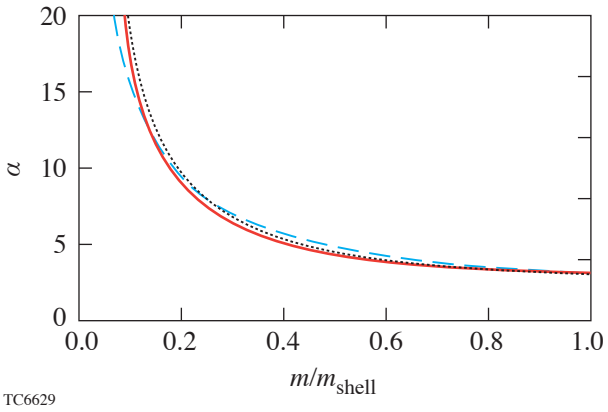

Figure 101.3
A comparison of the simulated adiabat shape of type 1 (solid) with the full analytic formula [Eqs. (3)–(5)] (dotted) and the power-law approximation [Eqs. (12)–(14)] (dashed).

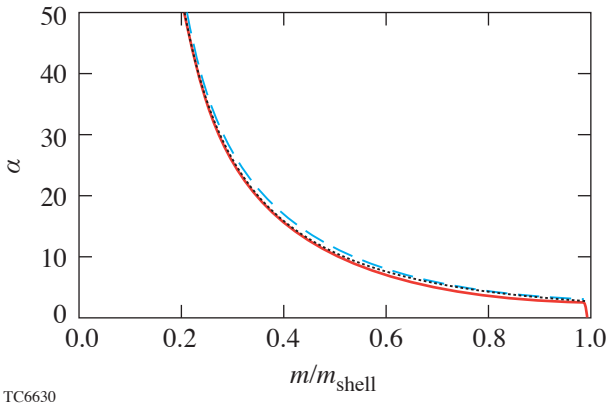

Figure 101.4
A comparison of the simulated adiabat shape of type 2 (solid) with the full analytic formula [Eqs. (7)–(11)] (dotted) and the power-law approximation [Eqs. (15)–(17)] (dashed).

Nonideal Effects on RX Adiabat Shaping

In realistic ICF implosions, quantifying the adiabat profile generated in a relaxation-design capsule is further complicated by other physical processes and constraints, such as radiation, thermal conduction, mass ablation, laser absorption and laser system constraints, realistic equations of state (EOS's), and spherical convergence. Radiation and thermal conduction effects may invalidate the assumption of isentropic flow away from the shocks. Mass ablation alters the position where the laser-induced shocks are launched and therefore affects the shock timing. In typical pulse designs, the laser-absorption histories, and hence applied pressure histories, are not constant over the duration of either the prepulse or the foot, as has been assumed in the previous analysis. Realistic EOS's yield different results for compressibility, shock and rarefaction speeds, and post-shock flow velocity than the ideal-gas approximation. A thorough theoretical treatment of these processes is beyond the scope of this article; however, an attempt is made here to quantify their effects on the shell's adiabat profile through simple reasoning and simulation.

In ICF capsules, the radiation emitted from the hot coronal plasma can penetrate the shell, heating the dense shell material up to a significant depth. This inevitably causes a "natural" shaping of the adiabat near the ablation front,[11–13] even when the laser pulse is designed to induce a flat adiabat. This effect may indeed be noticeable for capsules with high or moderate average atomic number, e.g., polystyrene plastic[23] (CH, $\langle Z \rangle = 3.5$). However, for the hydrogenic capsules ($Z = 1$) of interest for direct-drive ICF, the radiation shaping is typically negligible when compared with the laser-induced shaping discussed here.

Thermal conduction plays an essential role in ICF capsule implosions since the heat conducted from the laser-absorption region to the ablation surfaces determines the ablation pressure. At the ablation surface, the shell material absorbs heat rapidly, raising its adiabat quickly as it ablates off the shell. Once this shell material has been ablated, however, its adiabat is no longer relevant to the capsule stability since the ablation velocity is determined only by the local value of the adiabat at

the ablation surface. Furthermore, the contribution of heat conduction to the adiabat in the bulk of the shell is very small compared to the shock-induced adiabat since both the temperature and temperature gradients are small in the unablated shell. Therefore, thermal conduction effects on the adiabat profile (with the exception of mass ablation) may also be neglected.

Mass ablation occurs during the prepulse as well as the foot of the main pulse. While the mass ablated during the prepulse is negligible, a significant fraction ranging from 20% to 30% of the total shell mass is ablated during the foot of the main pulse. Since the mass m_* undertaken by the rarefaction wave before the interaction with the prepulse shock is small in type-2 adiabat shaping, the ablated mass m_{abl} often exceeds m_*. When this happens, the foot-pressure amplification through the region $0 < m < m_*$ is eliminated. In the absence of mass ablation, the applied foot pressure is amplified from P_f at $m = 0$ to $\omega_* P_f$ at m_*, where $\omega_* \approx 1.5$ is given in Eq. (9). If the mass m_* is quickly removed by mass ablation during the foot, then the main shock is launched with the pressure P_f instead of $\omega_* P_f$. Therefore, the validity of Eqs. (15)–(17) for the design of type-2 adiabat shaping can be easily extended to the ablative case by replacing the applied pressure P_f with $P_f/\omega_* \approx P_f/1.5$.

When dealing with thick cryogenic targets, spherical convergence effects should also be taken into account for an accurate estimate of the adiabat shapes. They can be easily included by replacing the areal mass coordinate m with the total mass coordinate $m^{\text{sph}} = \int_0^{\bar{r}} \bar{r}'^2 \rho(\bar{r}', 0)\, d\bar{r}'$. This requires a redefinition of m_* as follows:

$$m_*^{\text{sph}} = \frac{\rho_0}{3}\left(R_{\text{out}}^3 - R_*^3\right),$$

where R_{out} is the initial outer radius of the shell and

$$R_*^{\text{sph}} = \sqrt{4P_p/3\rho_0}\left(\Delta t_p + \Delta t_*\right)$$

is the radial coordinate of the rarefaction–shock merging.

To quantitatively account for all these effects, simulations were performed using *LILAC*,[24] a 1-D Lagrangian ICF code. The *LILAC* simulations used *SESAME* EOS in a spherical geometry, while modeling laser absorption by ray trace and inverse bremsstrahlung, thermal conduction using a flux-limited local thermodynamic equilibrium treatment, and radiation transport using multigroup diffusion. The target is an 85-μm-thick, solid-DT shell. The laser pulse, designed in accordance with pulse-shaping capabilities of the OMEGA laser system,[25] consists of an 80-ps, 15-TW square prepulse, with a finite ramp-up and ramp-down in intensity, followed by a 7-TW foot with finite ramp-up launched at about 950 ps. The average prepulse pressure found by *LILAC* is 23 Mb. The ablation pressure of the foot pulse at the time of shock generation is approximately 34 Mb. The resulting adiabat profile is shown in Fig. 101.5 (solid) and compared with the prediction of Eqs. (15)–(17) (dashed), including the above modifications, indicating good agreement between theory and simulation. Note that the optimal foot-pulse turn-on time predicted by theory is 800 ps, whereas the value in simulation was 950 ps, indicating that some retuning of the pulse was necessary.

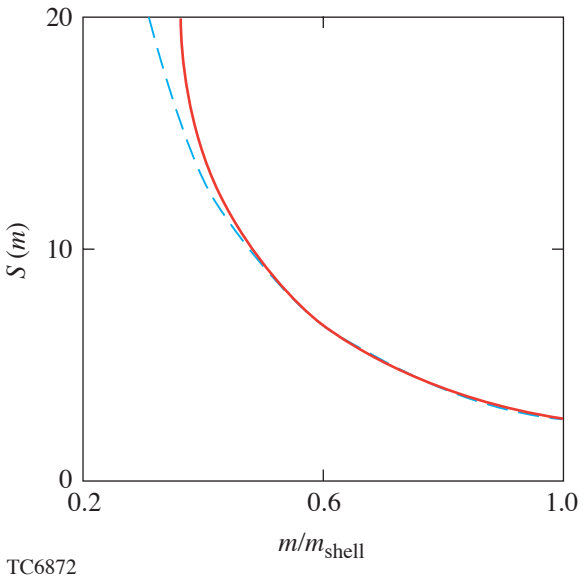

Figure 101.5
A comparison of the simulated adiabat shape predicted by *LILAC* (solid) with the analytic formula [Eqs. (15)–(17)] (dashed) for an OMEGA-scale design.

To estimate the increase in ablation velocity, it is important to recognize that in realistic ICF implosions, a significant fraction of the target material is ablated off during the foot of the laser pulse. For an RX pulse shape, about 20% to 30% of the target mass is ablated before the shock-breakout time, thus causing the shell's outer surface to shift inward. The shell acceleration starts shortly after the shock-breakout time when the laser power reaches its peak. The relevant outer-surface adiabat determining the ablation velocity is the adiabat at the ablation front, which moves deeper inside the target as more mass is ablated off. In mass coordinates, the ablation-front position is equal to the amount of mass ablated, $m_a(t)$. It follows that the ablation velocity for a shaped-adiabat implosion is determined by the following simple scaling law:

$$V_a^{\text{shaped}} \simeq V_a^{\text{flat}} \left(\frac{m_{\text{shell}}}{m_a(t)} \right)^{\frac{3}{5}\delta}, \tag{37}$$

where V_a^{flat} is the ablation velocity for a flat-adiabat implosion with $\alpha = \alpha_{\text{inn}}$ and δ equal to δ_{RX1}, δ_{RX2}, or δ_{DS}, depending on the shaping method. During the acceleration phase, V_a is maximum at the beginning [low $m_a(t)$] and decreases in time as more mass is ablated and $m_a(t)$ increases. At the beginning of the acceleration phase when $m_a \sim 0.3\, m_{\text{shell}}$, the shaped-adiabat ablation velocity is roughly 2 times the flat-adiabat value for the decaying-shock shaping ($\delta_{\text{DS}} \simeq 1.1$), about 1.5 times V_a^{flat} for type-1 RX shaping ($\delta_{\text{RX1}} \sim 0.7$), and over 3 times V_a^{flat} for type-2 RX shaping ($\delta_{\text{RX2}} \sim 1.6$ to 1.8). Figure 101.6 shows the time evolution of the ablation velocities computed by *LILAC* for a typical OMEGA-size cryogenic DT shell of 85-μm thickness and 345-μm inner radius. The three curves represent the three pulse designs: flat adiabat with $\alpha = 3$ (dashed), shaped adiabat by decaying shock (dotted), and shaped adiabat by RX-2 shaping (solid). The corresponding laser time histories are shown in Fig. 101.7, and the time axis in Fig. 101.6 is adjusted to fit the different acceleration phases (i.e., maximum laser power intervals) of the three designs. Observe that the RX-2 design leads to the largest ablation velocity, approaching 3 times the flat-adiabat value at the beginning of the acceleration phase.

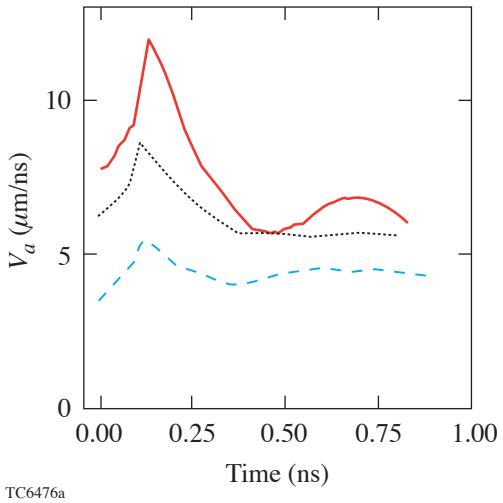

Figure 101.6
Time evolution of the ablation velocities during the laser pulse's flattop for flat $\alpha = 3$ (dashed), decaying-shock–shaped (dotted), and type-2 relaxation-shaped (solid) implosions.

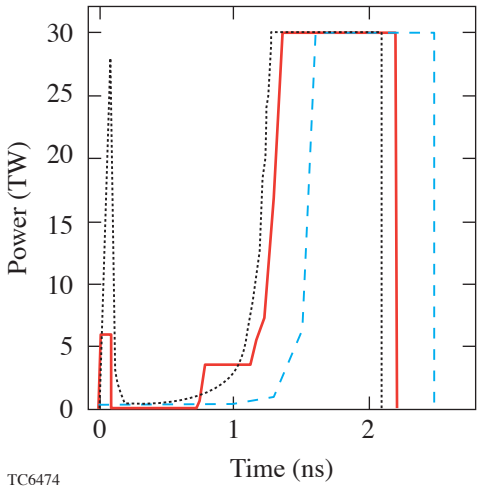

Figure 101.7
Laser pulse for a flat $\alpha = 3$ design (dashed), a decaying-shock design (dotted), and a type-2 relaxation design (solid) of comparable 1-D performance.

Conclusions

Analytic forms of the relaxation adiabat shapes have been derived for two cases: type 1, where the prepulse is long enough that the rarefaction wave catches the prepulse shock at the shell's inner surface; and type 2, the case of short prepulses, where the rarefaction wave/shock interaction occurs inside the shell. The analytic relaxation adiabat profiles derived here are in excellent agreement with simulations. Results indicate that the adiabat profiles for both type-1 and type-2 designs are well approximated by a power law for ICF-relevant values of the prepulse to main-pulse pressure ratio. The power-law indices for RX designs have been shown to be highly tunable, giving the possibility for tailoring adiabat profiles to desired design specifications. The type-2 relaxation designs also allow for power-law indices, which are substantially higher than those generated by decaying-shock designs (see Ref. 6), resulting in the possibility of higher ablation velocities and higher RT mitigation in RX designs, while maintaining similar one-dimensional compression and yield. In addition, formulas to aid in the design of RX implosions have been provided, and nonideal effects on RX adiabat shaping have been estimated.

ACKNOWLEDGMENT

This work was supported by the U.S. Department of Energy Office of Inertial Confinement Fusion under Cooperative Agreement No. DE-FC52-92SF19460, the University of Rochester, and the New York State Energy Research and Development Authority. The support of DOE does not constitute an endorsement by DOE of the views expressed in this article.

REFERENCES

1. W. K. Levedahl and J. D. Lindl, Nucl. Fusion **37**, 165 (1997).
2. M. M. Basko and J. Johner, Nucl. Fusion **38**, 1779 (1998).
3. M. C. Herrmann, M. Tabak, and J. D. Lindl, Nucl. Fusion **41**, 99 (2001).
4. A. Kemp, J. Meyer-ter-Vehn, and S. Atzeni, Phys. Rev. Lett. **86**, 3336 (2001).
5. R. Betti, K. Anderson, V. N. Goncharov, R. L. McCrory, D. D. Meyerhofer, S. Skupsky, and R. P. J. Town, Phys. Plasmas **9**, 2277 (2002).
6. K. Anderson and R. Betti, Phys. Plasmas **10**, 4448 (2003).
7. V. N. Goncharov, J. P. Knauer, P. W. McKenty, P. B. Radha, T. C. Sangster, S. Skupsky, R. Betti, R. L. McCrory, and D. D. Meyerhofer, Phys. Plasmas **10**, 1906 (2003).
8. K. Anderson and R. Betti, Phys. Plasmas **11**, 5 (2004).
9. L. J. Perkins, M. Tabak, J. Lindl, D. Bailey, J. Harte, A. Schmitt, S. Obenschain, and R. Betti, Bull. Am. Phys. Soc. **47**, 101 (2002).
10. K. Anderson, R. Betti, J. P. Knauer, and V. N. Goncharov, presented at the 34th Anomalous Absorption Conference, Gleneden Beach, OR, 2–7 May 2004.
11. J. H. Gardner, S. E. Bodner, and J. P. Dahlburg, Phys. Fluids B **3**, 1070 (1991).
12. S. E. Bodner *et al.*, Phys. Plasmas **7**, 2298 (2000).
13. L. Phillips *et al.*, Laser Part. Beams **17**, 225 (1999).
14. R. P. J. Town and L. J. Perkins, Lawrence Livermore National Laboratory, private communication (2003); M. Tabak, Lawrence Livermore National Laboratory, private communication (1987).
15. J. D. Lindl and W. C. Mead, Phys. Rev. Lett. **34**, 1273 (1975).
16. N. Metzler, A. L. Velikovich, and J. H. Gardner, Phys. Plasmas **6**, 3283 (1999).
17. N. Metzler *et al.*, Phys. Plasmas **9**, 5050 (2002).
18. N. Metzler *et al.*, Phys. Plasmas **10**, 1897 (2003).
19. T. J. B. Collins and S. Skupsky, Phys. Plasmas **9**, 275 (2002).
20. A. B. Iskakov *et al.*, Phys. Rev. E **61**, 842 (2000); E. Krousky *et al.*, Laser Part. Beams **18**, 87 (2000).
21. Laboratory for Laser Energetics LLE Review **98**, 106, NTIS document No. DOE/SF/19460-527 (2004). Copies may be obtained from the National Technical Information Service, Springfield, VA 22161.
22. R. Betti, K. Anderson, J. P. Knauer, T. J. B. Collins, R. L. McCrory, P. W. McKenty, and S. Skupsky, "Theory of Laser-Induced Adiabat Shaping in Inertial Confinement Fusion Implosions: The Relaxation Method," submitted to Physics of Plasmas.
23. K. Anderson, R. Betti, J. P. Knauer, and V. N. Goncharov, Bull. Am. Phys. Soc **49**, 210 (2004).
24. M. C. Richardson, P. W. McKenty, F. J. Marshall, C. P. Verdon, J. M. Soures, R. L. McCrory, O. Barnouin, R. S. Craxton, J. Delettrez, R. L. Hutchison, P. A. Jaanimagi, R. Keck, T. Kessler, H. Kim, S. A. Letzring, D. M. Roback, W. Seka, S. Skupsky, B. Yaakobi, S. M. Lane, and S. Prussin, in *Laser Interaction and Related Plasma Phenomena*, edited by H. Hora and G. H. Miley (Plenum Publishing, New York, 1986), Vol. 7, pp. 421–448.
25. T. R. Boehly, D. L. Brown, R. S. Craxton, R. L. Keck, J. P. Knauer, J. H. Kelly, T. J. Kessler, S. A. Kumpan, S. J. Loucks, S. A. Letzring, F. J. Marshall, R. L. McCrory, S. F. B. Morse, W. Seka, J. M. Soures, and C. P. Verdon, Opt. Commun. **133**, 495 (1997).

Improved Target Stability Using Picket Pulses to Increase and Shape the Ablator Adiabat

Introduction

The minimum energy required for ignition of the imploding capsule in inertial confinement fusion[1] is a strong function of the fuel adiabat α_{stag} (the ratio of the shell pressure to the Fermi-degenerate pressure) at the time of maximum compression: $E_{\min} \sim a_{\text{stag}}^{1.9}$ (Refs. 2 and 3). The shell must be driven on the lowest-possible adiabat to minimize this energy. The performance of low-adiabat implosions is limited by hydrodynamic instabilities that tend to disrupt the shell during the acceleration phase. The most important instability is the Rayleigh–Taylor[4,5] (RT) instability that is seeded by single-beam nonuniformities and surface roughness. The RT growth is reduced by mass ablation from the target surface[6–9] characterized by the ablation velocity V_a.

Interface perturbations grow exponentially ($a = a_0 e^{\gamma t}$) during the "linear" phase of the RT instability and reach a saturation phase (when $a \sim \lambda/10$) where the growth continues at a reduced rate.[10] Here, a is the amplitude of the perturbation, a_0 is the initial perturbation amplitude (the seed), γ is the growth rate, and λ is the wavelength of the perturbation.

A great deal of effort has gone into reducing the seeds (a_0) caused by illumination nonuniformities (imprinting) and target imperfections. The effect of imprinting has been reduced by a number of beam-smoothing techniques, including distributed phase plates (DPP's),[11] polarization smoothing (PS) with birefringent wedges,[12,13] smoothing by spectral dispersion (SSD),[14] and induced spatial incoherence (ISI).[15] The effect of the RT instability can also be reduced by lowering the RT growth rate. It has been shown that the ablation-surface RT growth rate is reduced by the ablation process. Theoretical work that includes the effect of thermal transport[9] shows that the RT-growth-rate dispersion formula for a DT target is given by

$$\gamma_{\text{DT}} = \sqrt{A_T(L_0,\nu)kg - A_T^2(L_0,\nu)k^2 V_a V_{bo}}$$

$$-\left[1 + A_T(L_0,\nu)\right]kV_a,$$

where $A_T(L_0,\nu)$ is the Atwood number, a function of L_0 and ν; k is the perturbation spatial wave number; g is acceleration; L_0 is ablation interface thickness; V_a is ablation velocity; V_{bo} is the "blowoff" velocity; and ν is the thermal transport index. V_{bo} is equal to V_a times the ratio of the blowoff plasma density to the ablation surface density. The ablation velocity, in turn, increases with the adiabat α in the ablation region as $V_a \propto \alpha^{3/5}$ (Ref. 16). This is the compromise that faces target designers—lowering α reduces the minimum energy required for ignition, but increases the effects of the RT instability. This article describes recent results using a shaped adiabat that increases the ablation-surface adiabat while maintaining a low adiabat for the compressed fuel.

This article is divided into five sections: (1) the motivation for adiabat shaping; (2) the results from the planar growth and imprint experiments; (3) data from spherical implosions with the decaying-shock-wave picket and the relaxation picket; (4) simulations showing the extension of the picket pulses to cryogenic implosions; and (5) conclusions.

Adiabat Shaping

The conflicting requirements of the lower-adiabat fuel at the maximum compression and the higher-adiabat ablation region can be achieved by shaping the adiabat inside the shell. A schematic of a shaped shell adiabat is shown in Fig. 101.8, where the shell is represented as a region of constant density and the adiabat varies from 1.5 to 4. The shaded region is the portion of the shell that remains at the end of the acceleration phase of the implosion. The inner fuel region is on a low adiabat while the adiabat in the ablated mass is high. The first published work on adiabat shaping used the absorption of low-energy x rays[17] to increase the adiabat at the ablation surface.

A short, high-intensity picket pulse, as seen in Fig. 101.9(a), can be used to shape the shell adiabat by creating a decaying shock wave.[18,19] This technique modifies the adiabat by modifying the pressure inside the shell. The ablation pressure from the picket pulse creates a shock wave that raises the pressure at the ablation surface and propagates into the shell. A rarefaction

wave propagates toward the shock wave at the end of the picket pulse. The shock-wave pressure then decays after the rarefaction wave overtakes it, reducing the pressure and lowering the adiabat for the inner sections of the shell.

The shell adiabat can also be shaped by propagating a strong shock wave in a fluid where the density increases from the ablation surface to the inner shell.[20] This density shape is created by a low-intensity, narrow picket pulse that causes the shell to decompress after it is turned off. This pulse shape is shown in Fig. 101.9(b). Shell decompression creates a density profile that is low at the ablation interface and high in the inner shell. The pulse shape needs to be timed so that the shock wave from the drive pulse reaches the shell–gas interface at the same time as the rarefaction wave from the picket pulse.

Picket-pulse shapes are not new to inertial confinement fusion (ICF); Lindl and Mead mentioned picket pulses in Ref. 21. This work showed that multiple picket pulses used in a simulation showed reduced target distortions during implosion. This was attributed to the impulsive nature of the picket drive with no mention of adiabat shaping. In the 1980s, simulations done at Lawrence Livermore National Laboratory (LLNL) and LLE[22] showed that if a picket pulse is used with a low-adiabat drive, the acceleration RT growth is reduced.

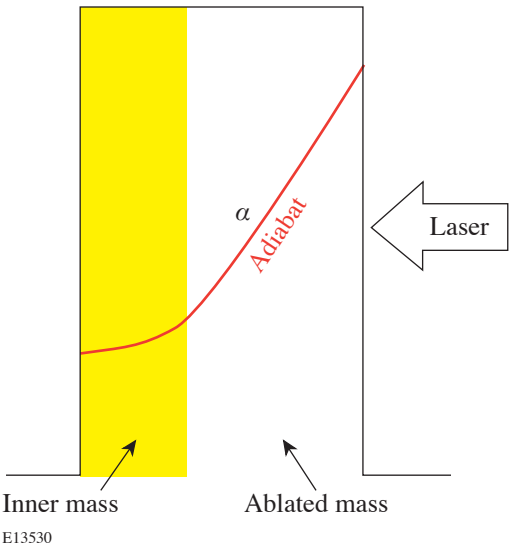

Figure 101.8
Schematic of a shell showing a shaped adiabat between the ablation surface and the inner surface. The shaded region is the portion of the shell that is not ablated. The adiabat is higher in the ablated material and therefore reduces the RT growth of ablation-interface perturbations.

LLE has done planar RT growth experiments[23] with picket pulses and established an analytical understanding of adiabat shaping with picket pulses.[18–20] Picket pulses are being actively studied to improve direct-drive target performance.

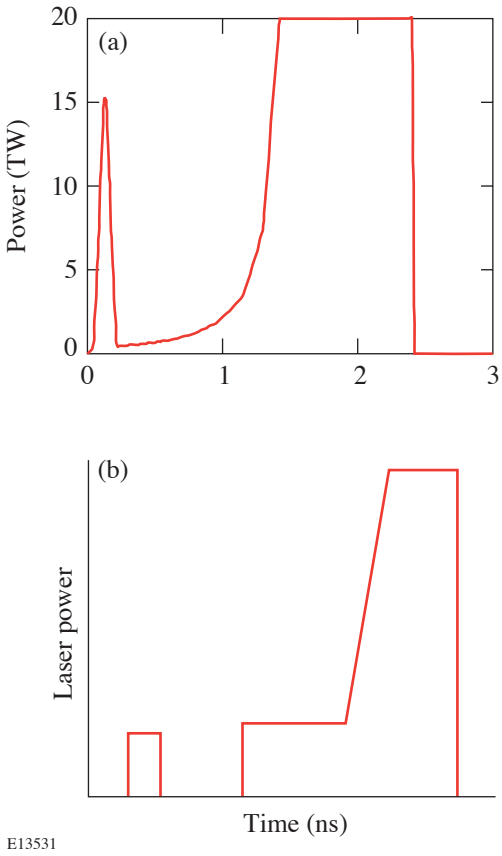

Figure 101.9
Laser pulse shapes for a decaying-shock-wave picket and a relaxation picket. In (a) the decaying shock wave is created by the short picket at the beginning of the pulse shape. The adiabat is shaped as the shock wave decays. The pulse shape for a relaxation picket drive is shown in (b). The low-intensity, narrow picket in front creates a spatial-density profile that is low at the ablation region and high inside the shell. The strong shock wave resulting from the high foot intensity then propagates through this density profile, shaping the shell's adiabat.

Planar Experiments

Acceleration interface perturbation growth due to the RT instability has been routinely studied in planar targets. A non-converging planar target allows the whole foil to be placed on a high adiabat to study how the adiabat affects the RT growth. The mass-modulated accelerated foil was composed of a 20-μm-thick CH foil with perturbations imposed on the side irradiated by the laser.[24] This thickness was chosen because it has about two attenuation depths for the 1.0- to 1.5-keV x rays

used for radiography. The initial perturbations were (1) a wavelength of $\lambda = 60$ μm and amplitude of $a = 0.25$ μm; (2) $\lambda = 30$ μm and $a = 0.125$ and 0.25 μm; and (3) $\lambda = 20$ μm and $a = 0.05$ and 0.25 μm. The perturbation amplitudes decreased with decreasing wavelength to ensure that the growth was measured in the "linear" ($a < \lambda/10$) phase of the RT instability. The 0.25-μm-amplitude perturbation at wavelengths of 30 μm and 20 μm was used to study the stability of this perturbation for large picket intensities where little or no growth was expected and the smaller amplitude perturbation was below the detection threshold.

Planar targets with imposed mass perturbations were accelerated using ten laser beams overlapped with a total overlapped peak intensity of 1.7×10^{14} W/cm^2. Each of the drive beams was focused to a spot size with a diameter of ~930 μm (at the 5% intensity contour) and used all of the beam smoothing available on OMEGA. The use of distributed phase plates, polarization smoothing, and SSD resulted in a laser-irradiation nonuniformity relative to the intensity envelope of <1% over a 600-μm-diam region defined by the 90% intensity contour. Two pulse shapes were used for the drive beams: first, a pulse with a Gaussian rise to a 2-ns constant intensity (referred to as the drive pulse) and, second, this same pulse with a Gaussian picket placed ~2 ns ahead of the time when the drive pulse reaches constant intensity. The pulse shape is shown in Fig. 101.10(a). The maximum drive intensity was designed to be the same for irradiation with and without a picket.

A comparison of the calculated and measured amplitudes of the fundamental Fourier mode of the optical-depth modulation for a 20-μm-wavelength perturbation is shown in Fig. 101.10(b), for a drive pulse only, a picket 50% of the drive-pulse intensity, and a picket 100% of the drive intensity. The data with and without the picket have been temporally shifted to match the start of the measured drive pulse. Multiple shots were performed at each wavelength, with the x-ray diagnostics using different temporal windows covering the duration of the drive pulse. A clear reduction in the 20-μm-wavelength perturbation growth rate is seen for the 50% I_p/I_d data. Data for a picket with an intensity of 100% of the drive pulse show that the ablation velocity during the drive pulse is large enough to stabilize the RT growth at this wavelength. Two-dimensional (2-D) hydrodynamic simulations of the experiment agree with the experimental data without and with picket pulses with intensities equal to 50% of the drive pulse.

A picket pulse is also effective in reducing the imprint seed for the RT instability in cryogenic implosions.[22] Current cryogenic targets are thin (~3- to 5-μm) CH shells with a 100-μm layer of DT or D_2 ice. The density mismatch between the CH shell and the hydrogenic layer causes a pressure gradient to be established during the constant-intensity foot portion of the

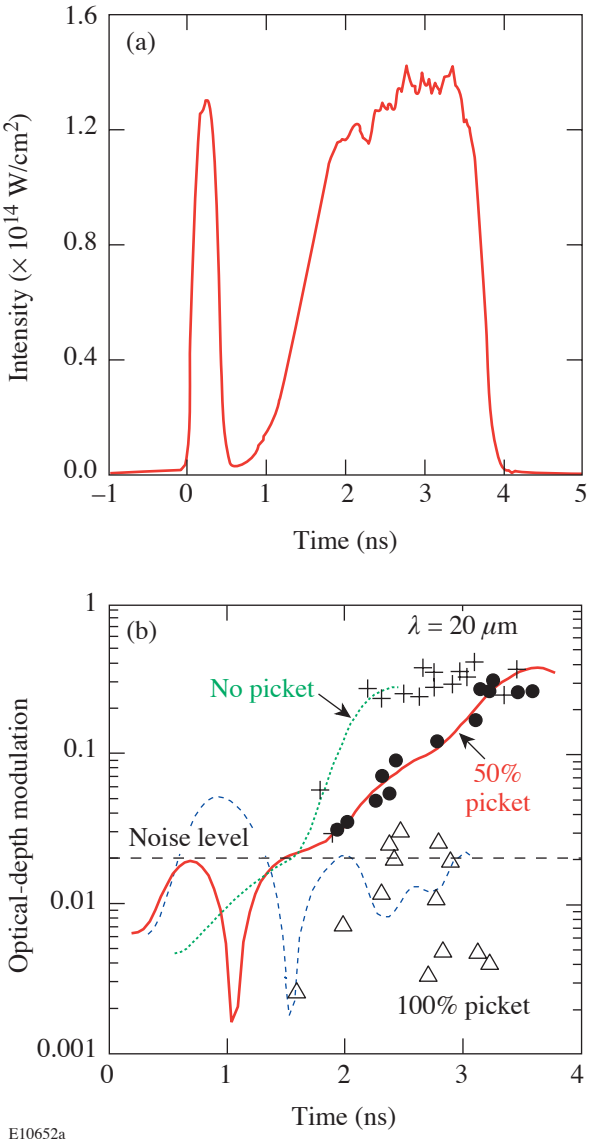

Figure 101.10
Planar RT growth experiments used the pulse shape shown in (a). The 300-ps-wide picket caused the foil to decompress, lowering the ablation-interface density and raising the ablation velocity. The modulation in optical depth is shown in (b) for an imposed 20-μm-wavelength perturbation. Data without a picket are shown as plus (+) symbols, data for a picket with an intensity of 50% of the drive are shown as filled circles, and data for a picket with an intensity of 100% of the drive are shown as triangles. Lines indicate 2-D hydrodynamic simulations of the experiments with the dotted line for no picket, the solid line for a 50% picket, and the dashed line for a 100% picket.

laser illumination. The ablation surface is accelerated as a result of the pressure gradient, and the laser imprint is amplified by the RT instability. A picket pulse mitigates the pressure gradient and reduces the RT amplification of the laser nonuniformities and thus reduces the RT seed from imprinting for the target implosion.

Planar experiments were done to study imprint reduction with picket pulses for layered targets. The planar targets were constructed with a 5-μm-thick, solid-density CH layer and a 90-μm-thick CH foam layer with a density of 0.18 g/cm^3. This foil target acts as a surrogate for a section of a cryogenic spherical target. Intensity perturbations with wavelengths of 120, 90, 60, and 30 μm using specifically designed DPP's in a single beam were imposed on these planar foils. Figures 101.11 and 101.12 show the experimental optical-depth-modulation amplitude for these perturbations. Data in Figs. 101.11(a) and 101.11(b) show little reduction in the imprinting for long-

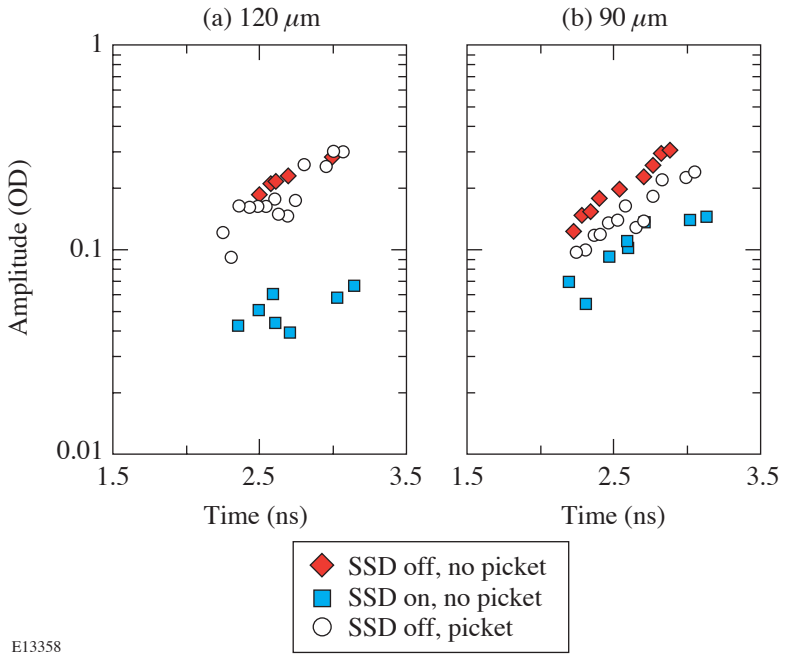

Figure 101.11
Imprinting data for 120-μm and 90-μm intensity perturbations. Data with SSD off and no picket are plotted as diamonds, data with SSD on and no picket as squares, and data with SSD off and with the picket as circles.

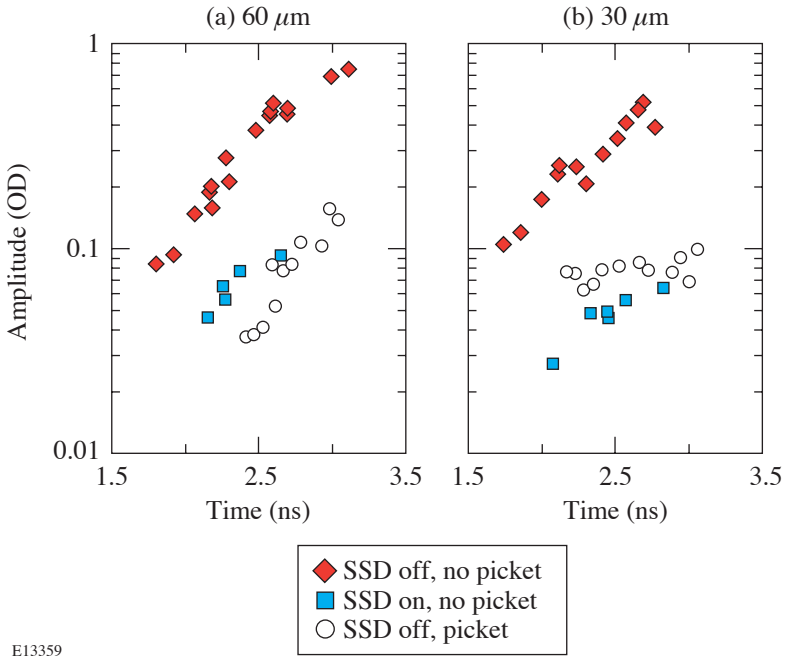

Figure 101.12
Imprinting data for 60-μm and 30-μm intensity perturbations. Data with SSD off and no picket are plotted as diamonds, data with SSD on and no picket as squares, and data with SSD off and with the picket as circles.

wavelength perturbations when the picket pulse was used. There is no difference at 120-μm-wavelength perturbations [Fig. 101.11(a)] with and without the picket. The data for a 90-μm-wavelength perturbation [Fig. 101.11(b)] with the picket pulse lie between the data without the picket and with SSD off and SSD on. The shorter-wavelength perturbations show a greater effect on optical-depth modulation for the picket pulse [Figs. 101.12(a) and 101.12(b)].

Modulation in optical-depth data shows that the amplitude of the imprint with the picket is the same as that when SSD is on and there is no picket pulse. The DPP's used to impose the intensity perturbations are refractive optics, so SSD will not affect the perturbation wavelength but will reduce the contrast and, thus, the perturbation amplitude. The picket is as effective as one-dimentional (1-D), 1.5-Å SSD at reducing the imprint for 60-μm-wavelength [Fig. 101.12(a)] and 30-μm-wavelength [Fig. 101.12(b)] perturbations.

The temporal evolution of the optical-depth data shown in Figs. 101.11 and 101.12 shows that only the 30-μm-wavelength perturbation has its RT growth rate reduced. This is not unexpected. Previous planar growth experiments with picket pulses[20] have shown that the RT growth of long-wavelength perturbations ($\lambda \geq 60$ μm) is less affected by the picket pulse than the short-wavelength perturbations ($\lambda = 30$ and 20 μm). This is a result of the k-dependence of the ablation-velocity stabilization term in the dispersion formula for the RT growth rate.

Spherical Experiments

The OMEGA[26] laser system imploded spherical targets with the pulse shapes shown in Fig. 101.13. Sixty beams of 351-nm radiation were incident onto the target. All beams had polarization smoothing, 1-THz bandwidth, 2-D SSD, and DPP's with an intensity envelope given by a third-order super-Gaussian to minimize the illumination nonuniformities imposed by the laser. The targets used for these measurements are shown as the inset in Fig. 101.13. The shells were made of either 33- or 27-μm-thick polystyrene and filled with three gas-fill conditions: 15 atm of D_2; 3 atm of D_2; and a mixture of 12 atm of ^{3}He and 6 atm of D_2. All targets had a 1000-Å layer of aluminum as a gas-retention barrier. The laser pulse shapes were optimized for an outer diameter of 906 μm, and the targets had diameters that ranged from 901 to 923 μm.

Results from the fusion-product-yield measurements for three shots for each target and pulse shape are shown in Figs. 101.14(a) and 101.14(b). For the 15-atm-D_2-filled, 33-μm-thick shell [Fig. 101.14(a)], there is a factor-of-3 increase in the number of D_2 neutrons from the target irradiated with a picket pulse than that from the target without a picket. The experiment was optimized for the 33-μm-thick shells; the improvement for the 27-μm-thick shells is only 50%. Both the 3-atm-D_2-filled and the ^{3}He-D_2-filled, 33-μm-thick shells show an improved fusion yield by a factor of 2. The ratio of the measured primary neutron yield to the neutron yield predicted by the hydrodynamics simulation [usually referred to as yield-over-clean (YOC)] is plotted in Fig. 101.14(b) and shows that the 15-atm-D_2-filled, 33-μm-thick shells improve from 0.03 to 0.19. In all cases, the YOC can be seen to improve significantly. The results from high-adiabat implosions with 1-ns square drive pulses are also plotted in Figs. 101.14(a) and 101.14(b). The absolute fusion yield from the 1-ns square data is between yields measured without and with the picket pulse. A high-adiabat implosion will have a lower calculated yield, and therefore the YOC data for the 1-ns square implosions are higher than either the non-picket or picket YOC's.

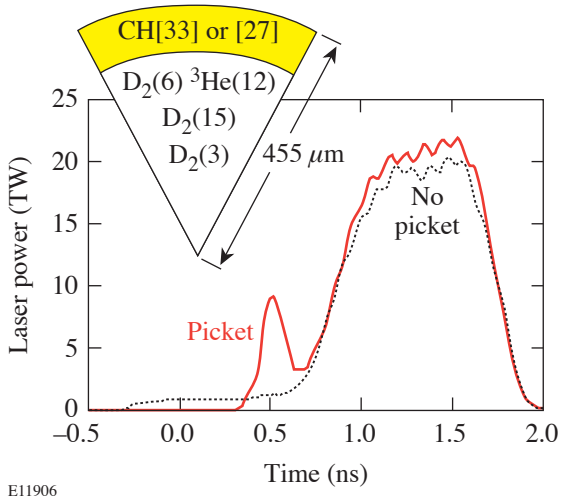

Figure 101.13
Pulse shapes used for decaying-shock-wave picket-pulse experiments. The picket drive is shown as a line and the no-picket drive as a dotted line. The targets used are shown as an inset.

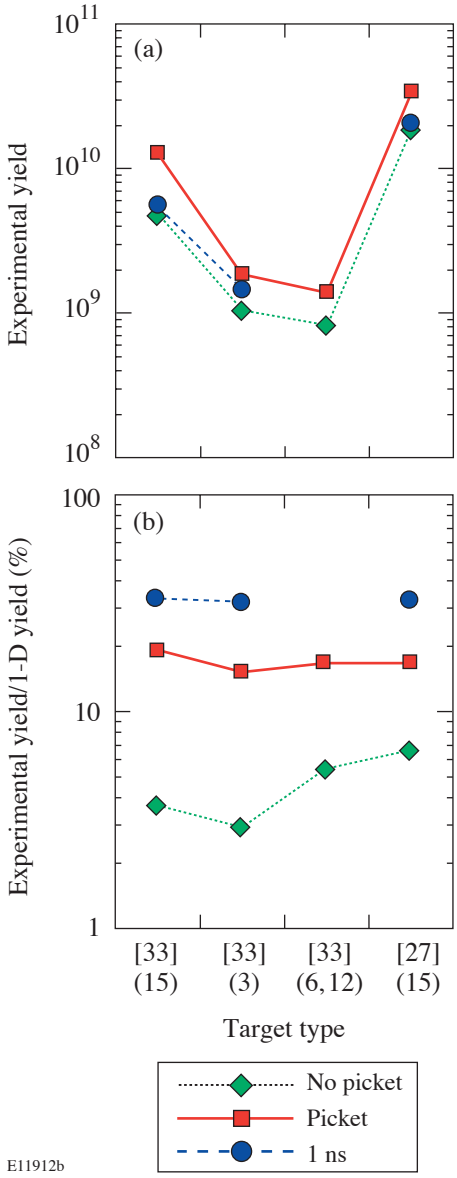

Figure 101.14
Fusion-produced yield from the decaying-shock-wave picket implosions. The absolute yields are shown in (a) and the normalized yields in (b). The picket data are plotted as squares, non-picket data as diamonds, and 1-ns square pulse implosions as circles.

Neutron-production rates for the 15-atm-D_2-filled, 33-μm-thick shell, measured (symbols) and predicted (lines), are shown in Fig. 101.15. The solid curve and open circles are data from the implosion without a picket. The dashed curve and filled circle plots are from the matching implosion using a picket. The experimental data were measured with the "neutron temporal diagnostic" (NTD).[27] The temporal offsets needed to compare experimental and simulation data were determined by maximizing the cross-correlation of the drive portion of the pulse as a function of a temporal shift relative to the laser pulse without a picket. This aligned the leading edges of the main drive pulse for all of the data. It is assumed that the neutron production is determined by the compression of the target by the drive pulse. Comparing the experimental data with predictions indicates that the implosions using a picket not only attain higher absolute yields than the implosions without a picket but also return, as was stated earlier, a larger fraction of the 1-D yield. This suggests more stable implosions with less mix due to RT growth. One-dimensional hydrodynamic simulations indicate that there is little if any adiabat shaping from the picket for these implosions. CH targets are affected by radiation transport that changes the shell adiabat, and this dominates the adiabat from the picket at the time of peak acceleration. Cryogenic D_2 targets will not be dominated by radiation and should show decaying shock-wave adiabat shaping.

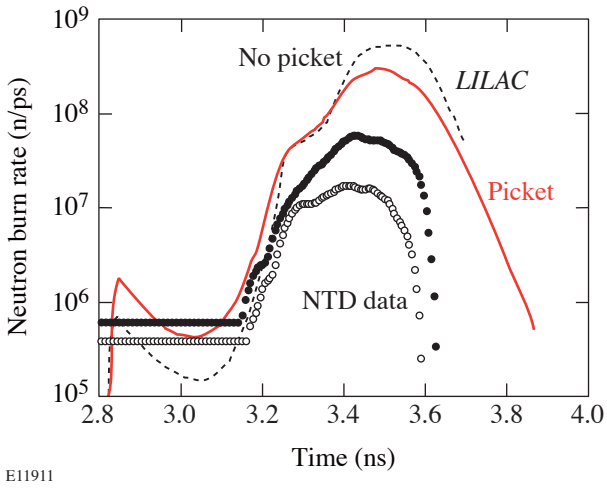

Figure 101.15
NTD data from the decaying-shock-wave implosions. *LILAC* simulation results are plotted for the non-picket pulse (dashed line) and the picket pulse (solid line). Experimental data are plotted for the non-picket pulse (open circles) and the picket drive (dark circles).

The OMEGA laser system was also used to study the effect of relaxation picket target designs on imploding CH shells. A relaxation picket implosion uses a picket in front of a drive pulse that has a high foot intensity. The picket is separated from the drive pulse by a region of zero intensity during which time a rarefaction wave causes the shell to decompress. The non-picket drive is designed to implode the targets on the same adiabat ($\alpha \sim 2$) as that of the inner layer for the relaxation

picket. These pulse shapes are shown in Fig. 101.16. The picket pulse had a FWHM of ~60 ps. The targets shown schematically by the inset in Fig. 101.16 were designed for a total laser energy of 18 kJ. They are 870-μm-diam, 35-μm-thick CH shells filled with 15 atm of D_2. A thin (1000-Å) Al layer coated the outside of the targets and was the gas retention barrier.

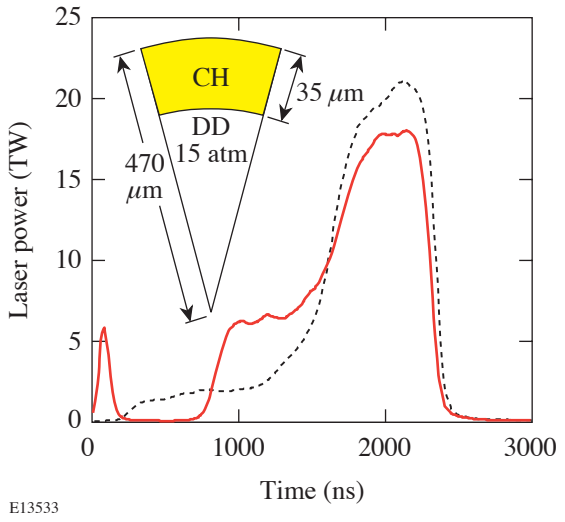

Figure 101.16
Pulse shapes used for relaxation-picket-pulse experiments. The picket drive is shown as the solid line and the non-picket drive as the dashed line. The targets used are shown as an inset.

The measured experimental yields increased when a relaxation (RX) picket pulse was used. The neutron yields shown in Table 101.I were taken for laser drives with and without SSD and with and without a picket pulse. With either SSD on or SSD off, the neutron yields are higher when a picket-pulse drive is used. The yield increases by a factor of 2.5 in the case of SSD off. The laser energy (17.3±0.2 kJ) was very stable for these implosions, allowing for the direct comparison of measured yield data.

Table 101.I: Measured experimental yields increase when a relaxation picket is used.

	SSD Off	SSD On	Clean 1-D
	Yield ($\times 10^9$)	Yield ($\times 10^9$)	Yield ($\times 10^{10}$)
Picket	5.6±0.2	6.8±0.2	5.2±0.5
No picket	2.2±0.1	5.5±0.5	4.0±0.2

One-dimensional hydrodynamic simulations[28] were used to calculate the adiabat shape at the start of acceleration and at peak acceleration shown in Fig. 101.17. *LILAC* simulations indicate that RX adiabat shaping in CH is effective throughout the acceleration phase. The adiabat without a picket pulse is illustrated as the "flat" case. At the start of the shell acceleration the adiabat is nearly constant at $\alpha = 2$ when no picket pulse is used. The RX drive has an adiabat of $\alpha = \sim 12$ at the ablation interface and an $\alpha = 2$ for the inner shell layer. The shape of the adiabat is still steeper for the RX drive at the time of peak acceleration, thus maintaining the effect of a high adiabat at the ablation interface while keeping a low ($\alpha = 2$) adiabat in the shell's interior.

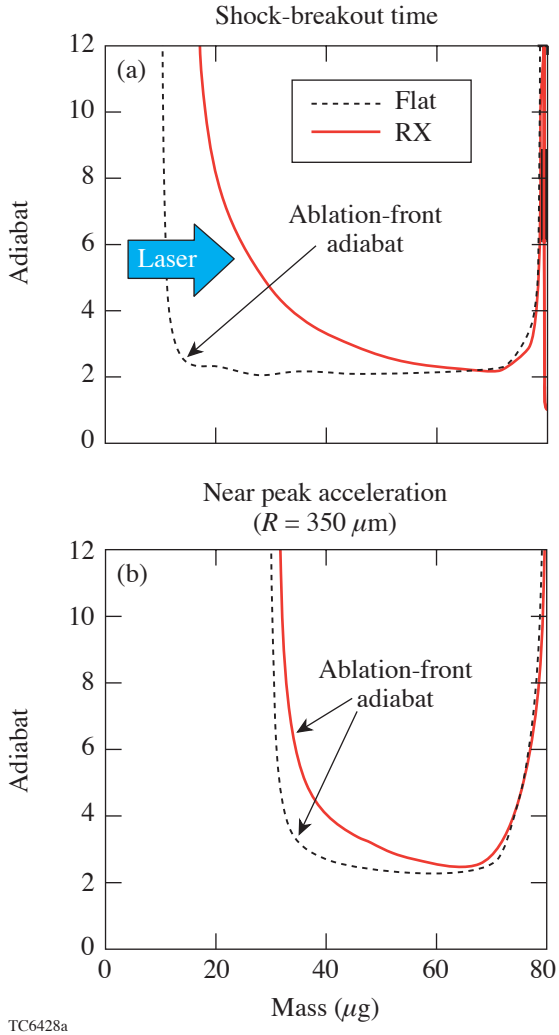

Figure 101.17
Shell adiabat shapes for the relaxation-picket-drive implosions. Shapes for the start of the acceleration are shown in (a) and those for near the peak acceleration are shown in (b). The non-picket drive is shown as a dashed line while the picket-drive profiles are shown as a solid line. The *x* axis is the Lagrangian mass coordinate.

Extension to Cryogenic Targets

The planar and spherical experimental data can be used to predict the expected performance of cryogenic target picket-pulse implosions. Greater shell stability is predicted for high-performance OMEGA cryogenic target designs with a picket pulse.[18] The decaying-shock-wave picket pulse for a cryogenic target is shown in Fig. 101.18. An OMEGA cryogenic target is typically 860 μm in diameter with a 5-μm-or-less CH shell, with a 65-μm-or-greater DT-ice layer, and a DT-gas pressure determined by the target's temperature. A schematic of this target is shown as the inset in Fig. 101.18. These target implosions are simulated with a drive pulse that has a peak intensity of 30 TW. A 20-TW picket is added for picket implosions. Table 101.II lists the 1-D simulation results. The simulations show that the picket does not compromise the core conditions but improves the shell's integrity. The calculated ρR is 330 mg/cm^2 without the picket and 305 mg/cm^2 with the picket drive. Neutron yields are nearly identical at 6.5×10^{14} and 6×10^{14} without and with the picket, respectively. The shell's stability or integrity is determined by the ratio of the bubble amplitude to the shell thickness. This ratio is greater than 100% for the non-picket implosion and only 55% for the picket implosion.

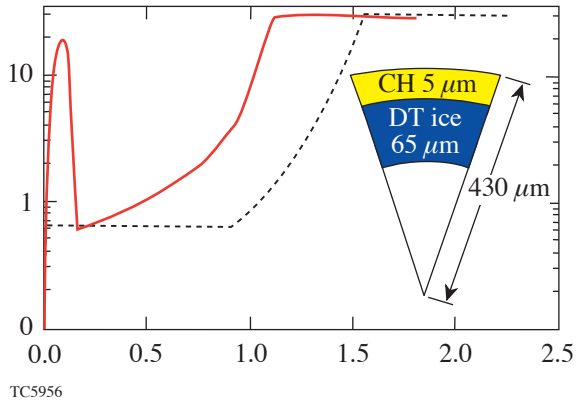

Figure 101.18
Pulse shapes used for cryogenic target simulations. The picket drive is shown as a solid line, and the non-picket drive as a dashed line. The targets used are shown as an inset.

Table 101.II: The decaying-shock-wave picket improves the stability of cryogenic target implosions.

	No Picket	Picket
ρR (mg/cm^2)	330	305
Y ($\times 10^{14}$)	6.5	6
A_{bubble}/Th (%)[1]	>100	55

Calculated adiabat and density profiles for both the decaying-shock-wave and relaxation-picket-pulse shapes are shown in Figs. 101.19(a) and 101.19(b). A decaying-shock-wave picket shapes the shell's adiabat [Fig. 101.19(a)] for a cryogenic target at the start of acceleration. The average adiabat for the ablated mass and the inner mass can be calculated from the simulation output. The average ablated mass adiabat calculated for the adiabat shape at the start of acceleration is 8 and the average inner adiabat is 5. At the end of the acceleration phase the average shell adiabat is 5; therefore, the cryogenic target was imploded with a higher ablation interface adiabat than the interior shell adiabat. The relaxation picket shapes the adiabat of the shell at the onset of acceleration as shown in

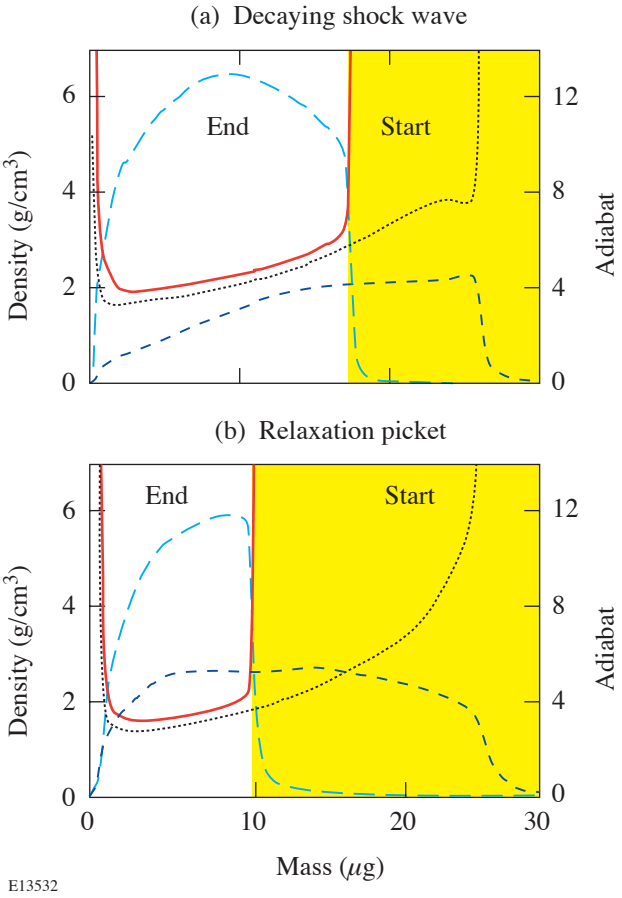

Figure 101.19
Shell adiabat and density shapes for the cryogenic target simulations. Shapes for the decaying-shock-wave picket at the start and end of shell acceleration are shown in (a) and those for the relaxation picket are shown in (b). The non-picket drive adiabat is shown as a solid line while the picket drive adiabat profiles are shown as a dotted line. The density profiles for the non-picket drive are shown as the long-dashed curves and density profiles for the picket drive are shown as the short-dashed curves. The shaded region represents the ablated mass.

Fig. 101.19(b). The RX drive simulations are also used to calculate the average adiabats for the ablated mass and the shell's interior. The shell's adiabat varies from $\alpha = 16$ at the ablation interface to $\alpha = 3$ in the shell's interior. The average adiabat for the ablated mass is 12 and for the inner shell is 3 at the start of shell acceleration. The average shell adiabat at the end of shell acceleration is 4. Both the decaying-shock-wave and the RX picket pulses shape the shell's adiabat for OMEGA cryogenic targets.

Conclusions

Picket pulses coupled to a low-adiabat drive pulse reduce both imprinting and perturbation growth. Adiabat shaping has the potential to improve target stability without significantly increasing the energy needed for compression and ignition. The ablation surface has a high adiabat to increase the ablation velocity and therefore reduce the RT growth. This is done while maintaining the inner portions of the shell on a low adiabat so that the energy needed to compress the core is minimized. The adiabat can be shaped either by launching a decaying shock wave that has a high pressure at the ablation surface and a low pressure at the inner shell surface or by using a picket pulse to produce a spatial density distribution so that a strong shock wave propagating from the ablation interface to the inner shell surface produces an adiabat that is high in the ablated material and low in the compressed material.

Planar experiments with picket pulses have reduced RT growth and imprinting, and spherical experiments with picket pulses show increased fusion yields when a picket pulse is used. With a picket-pulse intensity equal to 50% of the drive-pulse intensity, the RT growth was reduced for a 20-μm-wavelength surface perturbation and no significant RT growth was measured for a picket intensity equal to 100% of the drive pulse. Imprint experiments demonstrated that picket pulses were as effective as 1-D, 1.5-Å SSD at the reduction of imprint for both 60-μm- and 30-μm-wavelength perturbations. Spherical target experiments were done with picket pulses that generate a decaying shock wave and a relaxed density profile. The yields of fusion products are improved both in terms of the absolute value and in terms of the comparison to 1-D hydrodynamic simulation output for the decaying-shock-wave picket, and the absolute yield increased with SSD on and SSD off when the relaxation picket was used.

One-dimensional and two-dimensional hydrodynamic simulations with cryogenic targets show that performance is expected to improve when either the decaying shock wave or the relaxation picket pulse is used. The shell's adiabat can be shaped with either the decaying-shock-wave picket or the relaxation-picket-pulse shape. There is little difference between the core conditions with the flat-shell adiabat or the shaped-shell adiabat, but the ratio of the bubble amplitude to shell thickness is ~55% when the picket is added to the drive.

Results with warm CH targets and calculations with cryogenic targets indicate that picket pulses can be used for NIF direct-drive implosions. Either the decaying-shock-wave or the relaxation-picket-pulse shape can be used to improve the likelihood of achieving ignition.

ACKNOWLEDGMENT

This work was supported by the U.S. Department of Energy Office of Inertial Confinement Fusion under Cooperative Agreement No. DE-FC52-92SF19460, the University of Rochester, and the New York State Energy Research and Development Authority. The support of DOE does not constitute an endorsement by DOE of the views expressed in this article.

REFERENCES

1. J. Nuckolls *et al*., Nature **239**, 139 (1972).
2. M. C. Herrmann, M. Tabak, and J. D. Lindl, Nucl. Fusion **41**, 99 (2001).
3. R. Betti, K. Anderson, V. N. Goncharov, R. L. McCrory, D. D. Meyerhofer, S. Skupsky, and R. P. J. Town, Phys. Plasmas **9**, 2277 (2002).
4. Lord Rayleigh, Proc. London Math Soc. **XIV**, 170 (1883).
5. G. Taylor, Proc. R. Soc. London Ser. A **201**, 192 (1950).
6. S. E. Bodner, Phys. Rev. Lett. **33**, 761 (1974).
7. J. D. Lindl, in *Inertial Confinement Fusion*, edited by A. Caruso and E. Sindoni (Editrice Compositori, Bologna, Italy, 1989), pp. 595–615.
8. H. Takabe *et al*., Phys. Fluids **28**, 3676 (1985).
9. R. Betti, V. N. Goncharov, R. L. McCrory, P. Sorotokin, and C. P. Verdon, Phys. Plasmas **3**, 2122 (1996).
10. S. W. Haan, Phys. Rev. A, Gen. Phys. **39**, 5812 (1989).
11. T. J. Kessler, Y. Lin, J. J. Armstrong, and B. Velazquez, in *Laser Coherence Control: Technology and Applications*, edited by H. T. Powell and T. J. Kessler (SPIE, Bellingham, WA, 1993), Vol. 1870, pp. 95–104.
12. Y. Kato, unpublished notes from work at LLE, 1984.
13. T. R. Boehly, V. A. Smalyuk, D. D. Meyerhofer, J. P. Knauer, D. K. Bradley, R. S. Craxton, M. J. Guardalben, S. Skupsky, and T. J. Kessler, J. Appl. Phys. **85**, 3444 (1999).
14. S. Skupsky, R. W. Short, T. Kessler, R. S. Craxton, S. Letzring, and J. M. Soures, J. Appl. Phys. **66**, 3456 (1989).

15. R. H. Lehmberg and S. P. Obenschain, Opt. Commun. **46**, 27 (1983).

16. J. D. Lindl, *Inertial Confinement Fusion: The Quest for Ignition and Energy Gain Using Indirect Drive* (Springer-Verlag, New York, 1998), Chap. 5, p. 54.

17. J. H. Gardner, S. E. Bodner, and J. P. Dahlburg, Phys. Fluids B **3**, 1070 (1991).

18. V. N. Goncharov, J. P. Knauer, P. W. McKenty, P. B. Radha, T. C. Sangster, S. Skupsky, R. Betti, R. L. McCrory, and D. D. Meyerhofer, Phys. Plasmas **10**, 1906 (2003).

19. K. Anderson and R. Betti, Phys. Plasmas **10**, 4448 (2003).

20. K. Anderson and R. Betti, Phys. Plasmas **11**, 5 (2004).

21. J. D. Lindl and W. C. Mead, Phys. Rev. Lett. **34**, 1273 (1975).

22. M. Tabak, Lawrence Livermore National Laboratory, private communication (1987); R. P. J. Town and L. J. Perkins, Lawrence Livermore National Laboratory, private communication (2003).

23. T. J. B. Collins, J. P. Knauer, R. Betti, T. R. Boehly, J. A. Delettrez, V. N. Goncharov, D. D. Meyerhofer, P. W. McKenty, S. Skupsky, and R. P. J. Town, Phys. Plasmas **11**, 1569 (2004).

24. J. P. Knauer, R. Betti, D. K. Bradley, T. R. Boehly, T. J. B. Collins, V. N. Goncharov, P. W. McKenty, D. D. Meyerhofer, V. A. Smalyuk, C. P. Verdon, S. G. Glendinning, D. H. Kalantar, and R. G. Watt, Phys. Plasmas **7**, 338 (2000).

25. T. J. B. Collins and S. Skupsky, Phys. Plasmas **9**, 275 (2002).

26. T. R. Boehly, D. L. Brown, R. S. Craxton, R. L. Keck, J. P. Knauer, J. H. Kelly, T. J. Kessler, S. A. Kumpan, S. J. Loucks, S. A. Letzring, F. J. Marshall, R. L. McCrory, S. F. B. Morse, W. Seka, J. M. Soures, and C. P. Verdon, Opt. Commun. **133**, 495 (1997).

27. R. A. Lerche, D. W. Phillion, and G. L. Tietbohl, in *Ultrahigh- and High-Speed Photography, Videography, and Photonics '93*, edited by P. W. Roehrenbeck (SPIE, Bellingham, WA, 1993), Vol. 2002, pp. 153–161.

28. M. C. Richardson, P. W. McKenty, F. J. Marshall, C. P. Verdon, J. M. Soures, R. L. McCrory, O. Barnouin, R. S. Craxton, J. Delettrez, R. L. Hutchison, P. A. Jaanimagi, R. Keck, T. Kessler, H. Kim, S. A. Letzring, D. M. Roback, W. Seka, S. Skupsky, B. Yaakobi, S. M. Lane, and S. Prussin, in *Laser Interaction and Related Plasma Phenomena*, edited by H. Hora and G. H. Miley (Plenum Publishing, New York, 1986), Vol. 7, pp. 421–448.

High-Spatial-Resolution Studies of UV-Laser-Damage Morphology in SiO_2 Thin Films with Artificial Defects

Introduction

The importance of conducting a quantitative, high-spatial-resolution investigation of thin-film-damage morphology is twofold. First, comparison of spatial frequencies of the damaged site with the surrounding unmodified material may indicate the presence of particular processes in the damage event. For instance, a smooth surface that is missing granular film structure usually points to melting of thin-film material. Second, experimental data on geometry (lateral size, depth, cross-sectional profiles, volume) of the modified material provide vital information for theoretical-model validation.

High-resolution studies of laser damage in thin films have generated a significant amount of information regarding morphological changes in coating materials under different conditions (wavelength and pulse length, fluence, spot size) of irradiation. The application of high-resolution methods established that nanosecond-pulse–driven damage in thin-film coatings is linked to localized absorbing defects. For lasers operating in the UV spectral range, even a few nanometer-sized defects can initiate thin-film damage in the form of craters.[1]

Despite this fact, very few systematic studies link thin-film-defect parameters and local laser fluence to micron- and nanometer-scale modification of thin-film material. The most important reason for that is that size and density of defects in laser-quality coatings are extremely small,[1] thus precluding any characterization. An investigation of the role of nodular defects in multilayer 1.06-μm laser damage[2,3] serves as one example of such studies. To assuage this challenge, SiO_2 thin films with embedded gold nanoparticles serving as artificial absorbing defects have been explored[4–13] and have proven to be a very useful model system for unraveling damage mechanisms.

Previous experiments with this system subjected to UV, nanosecond pulses showed that during the laser pulse, absorption is not confined to the absorbing defect.[7] Upon defect-temperature rise, modification of the surrounding matrix takes place followed by effective growth of the absorbing volume. According to theoretical predictions by M. Feit *et al.*,[14,15] this growth saturates when reaching a scale of the order of the excitation wavelength λ. The same theory establishes scaling relations between damage-crater diameter and particle-lodging depth at fixed laser-fluence conditions.

A detailed theoretical description of the laser-pulse-energy deposition followed by crater formation remains a challenge even for this well-characterized model system. The initial stages, including kinetics of absorption and heating in the gold particle and energy transfer processes at the particle–matrix interface, were studied by P. Grua *et al.*[16,17] It was shown that thermionic electron emission from gold inclusion is an important mechanism of energy transfer to the surrounding matrix.

Promising results have been obtained with the one-dimensional (1-D) hydrodynamic code DELPOR (F. Bonneau *et al.*[18]), including electromagnetic effects, thermal conduction, radiative transfer, ionization by thermal UV radiation, and propagation of shock waves. From this code, combined with the two-dimensional (2-D) hydrodynamic code HESIONE,[19] which calculates mechanical effects using brittle-fracture models, a crater-formation picture emerges for relatively large, 600-nm particles in qualitative agreement with experiment.[8,9] Remaining difficulties here are related to the paucity of accurate data on electrical, thermal, optical, and mechanical properties of materials in the solid, liquid, vapor, and plasma states in the temperature range from ambient to ~10^4 K.

In this work, we used 18.5-nm gold nanoparticles as artificial defects embedded in a SiO_2 thin film at several well-defined distances from the film surface. Atomic force microscopy (AFM) is used to investigate the damage morphology produced by 351-nm, 0.5-ns laser pulses and dominated by submicrometer-scale craters. Variation in crater diameter, depth, and shape with laser fluence and particle-lodging depth is systematically studied and compared with phenomenological-theory[14,15] predictions. The contributions of two major mechanisms of damage crater formation—melting/evaporation and fracture/ejection—are evaluated.

Experimental

A SiO_2 thin-film sample containing gold nanoparticles is prepared in three steps: Initially, a 240-nm SiO_2 thin film is deposited by *e*-beam evaporation onto a cleaved fused-silica (Corning 7980, 14 × 6 × 5 mm) substrate. Next, gold nanoparticles of average diameter $d = 18.5$ nm (standard deviation = 0.9 nm; data from Ted Pella, Inc.) in the form of a gold colloid are diluted in isopropanol and deposited by a micropipette onto the SiO_2-coated surface. Finally, the sample is returned to the coating chamber and coated with an additional layer of SiO_2. Five samples are prepared as described above, all coated in the same deposition run, each with a different capping-layer thickness: 30 nm, 60 nm, 110 nm, 190 nm, and 240 nm. A more detailed description of the sample preparation can be found in Ref. 7.

A Nd-doped glass laser (frequency-tripled, 351-nm, 0.5-ns pulses; 400-μm spot size) is used for sample irradiation. Laser-beam incidence on the entrance surface was slightly off-normal (~7°) in order to prevent influence of the back-reflection (~4%) from the sample exit surface. No damage is observed within the bulk or at the rear surface of the cleaved fused-silica substrate at the entrance-surface fluence <8.1 J/cm^2. Laser-fluence profiles are obtained from images captured by a low-noise (few electrons/pixel/s at a temperature of –40°C), high-dynamic-range, charge-coupled-device (CCD) imaging camera (Spectral Instruments, Inc.) in a sample equivalent plane. Correlation between laser-spot intensity and areal density and average size of damage craters allows attributing the peak fluence to the damage center (see Fig. 101.20). Once it is done, laser fluence versus sample-coordinate dependence can be easily established and damage crater geometry versus fluence behavior investigated. The particular laser fluence at which the crater diameter approaches zero value is defined as the nanoscale damage threshold.

The damage morphology investigation is conducted by means of atomic force microscopy (AFM) (NanoscopeIII, Digital Inst./Veeco) operated in tapping mode. High-aspect-ratio (better than 5:1) silicon probes are used to ensure convolution-free imaging of craters with steep wall angles approaching 80° with the horizon.

Results and Discussion

1. Damage Morphology

Submicrometer-sized craters, formed exclusively at nanoparticle locations,[7] are the main damage-morphology features. In the case of shallow particle-lodging depths (30 nm and 60 nm) and close to the crater-formation threshold, the craters are very small, with a typical lateral size of 35 to 50 nm, and randomly shaped (see Fig. 101.21). The absence of a rim elevated above the average surface level and the random shape point to a material-removal mechanism without significant melting. The portion of the film above the particle is probably ejected under pressure created in the process of particle heating. This picture holds in the fairly narrow fluence range of 0.5 to 0.8 J/cm^2 for a 60-nm lodging depth, and in the range of 0.6 to 4 J/cm^2 for a 30-nm lodging depth [detailed in the **Crater Geometry Versus Laser-Fluence Behavior** section (p. 28)]. Beyond this initial fluence range, a crater takes a

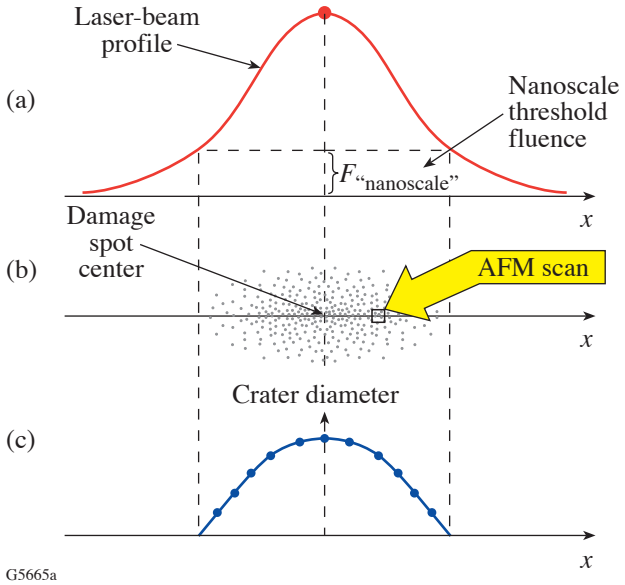

Figure 101.20
Experimental scheme of nanoscale damage threshold and crater diameter versus laser-fluence determination. (a) Laser-spot *x*-intensity profile; (b) damage crater areal distribution; (c) crater diameter versus *x* coordinate position. The nanoscale threshold value is defined as the laser fluence at which the crater diameter is approaching zero value.

conventional symmetric shape with an elevated rim, indicative of melting and resolidification (Fig. 101.22). The smooth internal surface of these craters, shown in Fig. 101.23, is missing the granular texture of the surrounding film, which is characteristic of melting and explosive vaporization. Later, this type of crater will be referred to as a *regular* crater. It is also useful to note here that under the term vaporization, we consider all processes transforming material from the liquid phase into the vapor phase, including fragmentation (nanocluster formation).

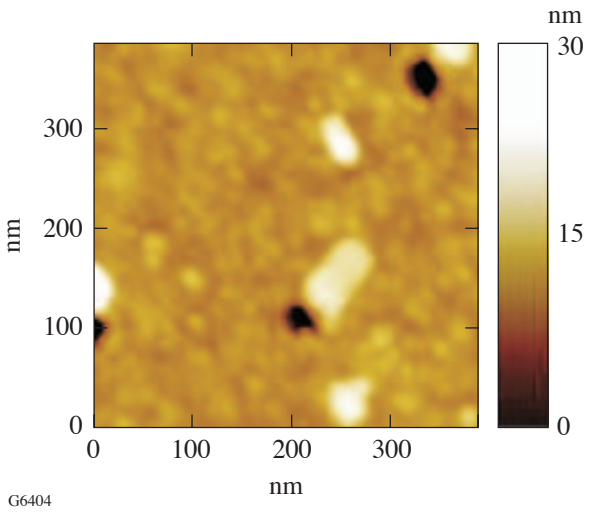

Figure 101.21
Craters originated by particles with 30-nm lodging depth at close-to-threshold conditions, 0.4-μm × 0.4-μm AFM image.

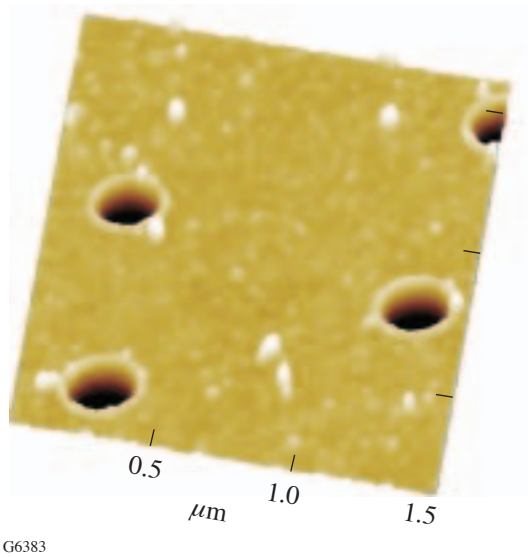

Figure 101.22
Typical craters originated by particles with 60-nm lodging depth at fluence F = 6.2 J/cm^2, 1.5-μm × 1.5-μm AFM scan.

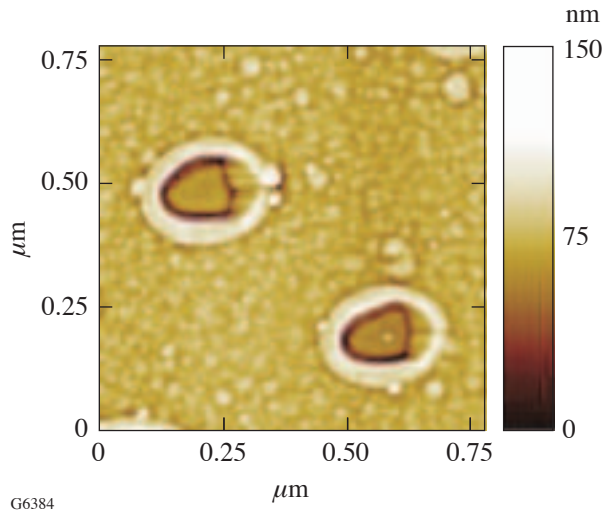

Figure 101.23
Internal walls of craters originated by particles with 60-nm lodging depth at fluences $F > 1$ J/cm^2 are missing granular structure of the surrounding film, indicative of melting and vaporization. Contrast enhancement function is applied in order to amplify high special frequencies, 0.8-μm × 0.8-μm AFM image.

Damage-crater morphology caused by particles at 190-nm and 240-nm lodging depths is very different. From this point this type of crater will be referred to as a *complex* crater. The lateral shape of these craters (depicted in Fig. 101.24) is asymmetric, most often with partial circularity and sharp corners—all pointing to hoop-stress–driven material removal. On the other hand, their internal surfaces are smooth (Fig. 101.25), indicative of the melting point having been reached. A cross-sectional profile of a typical complex crater is also depicted in Fig. 101.25. It clearly shows two parts: a narrow "channel" with vertical walls at the bottom and a wide upper part with inverse aspect ratio. Absence of the rim around the crater indicates that energy deposited in the upper part of the crater was insufficient to cause molten material flow at the outer crater boundary.

One possible scenario for the formation of this type of crater is as follows: Initially, absorption inside and around the particle causes melting and superheating of the material within the channel volume. This process is accompanied by rapid internal-pressure buildup and shock-wave generation. When the

generated hoop stress exceeds the strength of the silica material (fracture toughness ~0.75 Mpa • $m^{1/2}$ for bulk fused silica), fracture along the boundaries of the upper part of the crater takes place, followed by ejection of both the fractured portion and the molten material from within the channel.

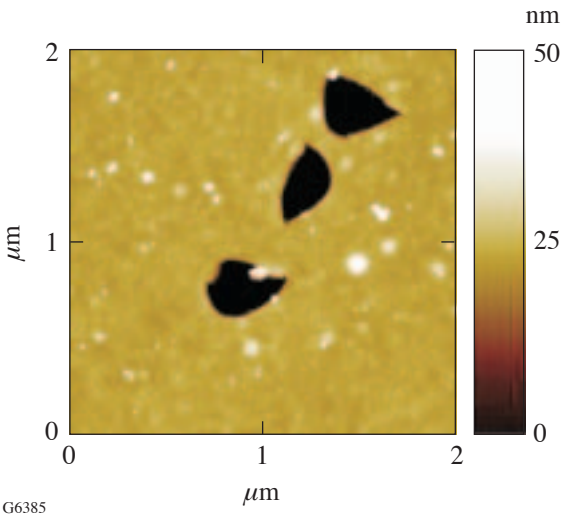

Figure 101.24
Craters originated by particles with 190-nm lodging depth. Random, partially circular shapes pointing to hoop-stress–driven material removal of the top film layer, 2-μm × 2-μm AFM scan.

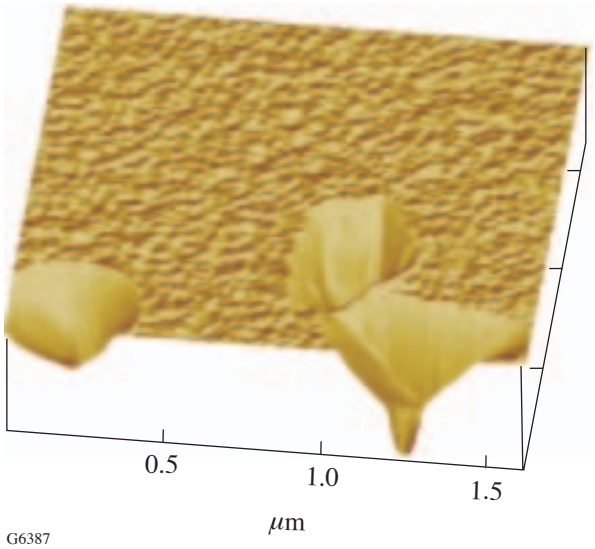

Figure 101.25
Smooth internal walls of complex craters point to the melting point having been reached. Cross-sectional crater profile reveals presence of two parts, a narrow channel on the bottom and a wide upper part removed by fracture.

Formation of such a complex crater was also reported in Refs. 9 and 10, where much larger gold particles of 600 nm were embedded in a SiO_2 film matrix. In the case of 110-nm lodging depth, both types of crater geometries characteristic for shallow and deep particle locations are present (Fig. 101.26).

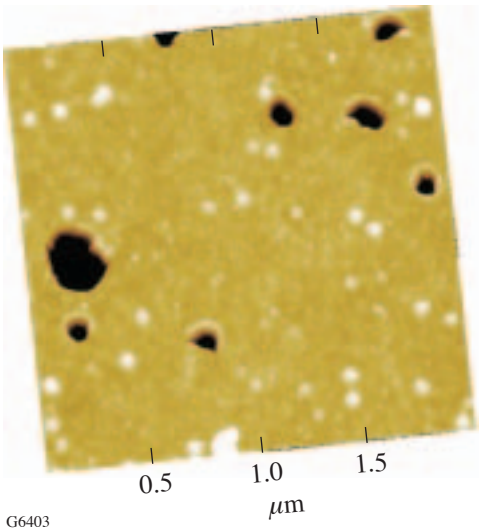

Figure 101.26
Craters formed from intermediate, 110-nm-deep particle location. Both types of craters, regular and complex, are generated simultaneously, 2-μm × 2-μm AFM scan.

2. Nanoscale Damage Thresholds

The definition of damage threshold has always been linked to the method of detecting material modification. Consequently, type and sensitivity of the damage-detection equipment have a major impact on measured threshold values. The most commonly used optical methods are adequate for practical evaluation of optical-component survival in high-power laser systems or for studying particular trends, like pulse-length dependencies. Still, these methods are very difficult to use for meaningful comparison with the theories describing the dynamics of the damage process.

AFM investigation of crater size versus laser-fluence dependencies allows one to find the crater-formation threshold (nanoscale threshold) as that fluence at which the crater diameter approaches zero. It corresponds to a maximum fluence causing only limited localized melting without material removal. This definition is in much better agreement with theories that consider matrix melting as the onset of damage.

The results of nanoscale-threshold measurement summarized in Table 101.III and in Fig. 101.27 show a threshold

increase with increasing particle-lodging depth. An explanation comes from the fact that at near-threshold conditions, deeper particles consistently produce deeper and larger craters [see the **Crater Geometry Versus Laser-Fluence Behavior** section (p. 28)]. Consequently, larger material removal requires more energy to be absorbed for a crater to form.

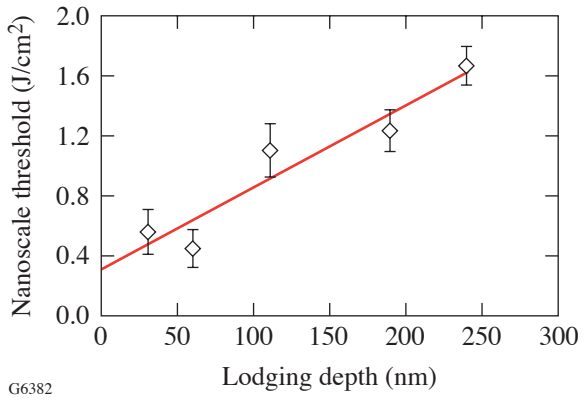

Figure 101.27
Nanoscale damage thresholds as a function of particle-lodging depth.

Table 101.III: Nanoscale damage thresholds.

Particle Lodging Depth		Nanoscale Threshold (J/cm^2)
h_0,nm	h_0/d	
30	1.6	0.56±0.15
60	3.2	0.45±0.10
110	5.9	1.11±0.21
190	10.3	1.24±0.16
240	13.0	1.67±0.14

3. Theoretical Approach to Crater Formation

As was mentioned above, numerical calculations of damage-crater–formation kinetics and final geometries are very challenging. In this work, we compare experimental results on crater lateral size behavior as a function of fluence and absorbing defect lodging depth with phenomenological-theory[14,15] predictions.

The main assumptions and results of this theory can be formulated as follows: If the temperature around an absorbing defect exceeds a critical value, a thermal explosion[20] takes place. In this process, the defect-surrounding matrix becomes absorptive and undergoes rapid heating and ionization with plasma density exceeding critical. This process is depicted schematically in Fig. 101.28.

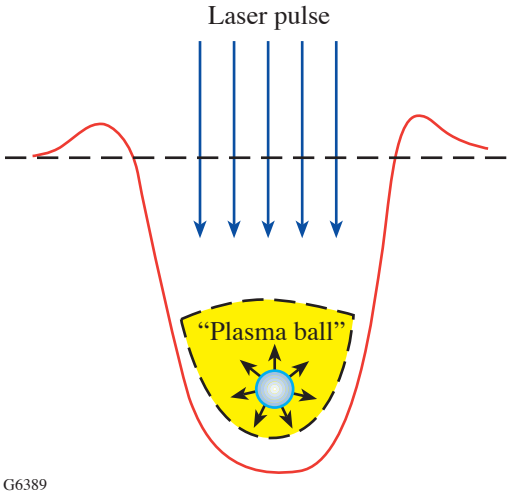

Figure 101.28
Schematic of the plasma-ball formation around an absorbing defect.

Considering that the major part of the absorbed energy goes into ionization of the material, the ionized volume (plasma "fire ball") radius a grows exponentially with laser fluence F:

$$a = a_0 \exp \gamma , \tag{1}$$

where the growth factor γ scales linearly with F.

At high laser fluences, growth of the plasma ball tends to saturate, and its diameter reaches a maximum value of the order of the absorbed-light wavelength λ. In this case absorbed energy can be estimated as

$$E = F\pi\lambda^2 . \tag{2}$$

The radius R of a produced crater is determined by E, the energy deposited in the plasma-ball volume, and h, the lodging depth of the initiating absorber.

At fixed energy E, the crater radius as a function of lodging depth h is given by the expression

$$R^2 = h^{2/3}\left(h_d^{4/3} - h^{4/3}\right), \tag{3}$$

where h_d is the maximum lodging depth at which a crater is still formed. For this depth, energy E is the threshold energy for crater formation and corresponds to the *nanoscale damage threshold*.

The maximum crater radius R_m and corresponding lodging depth h_m are given by

$$R_m = \sqrt{2}h_m \approx 0.6\,h_d \quad \text{and} \quad h_m \approx 0.44\,h_d. \tag{4}$$

At high laser fluences, when the growth of the plasma ball saturates, crater radius growth with fluence can be approximated by 1/3 power law:

$$R \sim F^{1/3}. \tag{5}$$

4. Crater Geometry Versus Laser-Fluence Behavior

a. Crater-diameter variation with fluence. Geometrical parameters measured for the two types of crater morphology are schematically presented in Fig. 101.29. Henceforth, a cross-sectional profile similar to Fig. 101.29(a) will be referred to as a regular crater, and one similar to Fig. 101.29(b) as a complex crater.

Crater diameter D is measured by means of the cross-sectional analysis of AFM images as crater opening at average surface level (see Fig. 101.29). In the case of asymmetric craters, diameter values are taken as an average of measurements taken in two orthogonal directions crossing the center of gravity of the crater opening area. Each data point in the $D(F)$ graph is obtained as an average for all craters (2 to 10) imaged within a particular AFM scan (2 μm × 2 μm or 3 μm × 3 μm) and correlated with one fluence value.

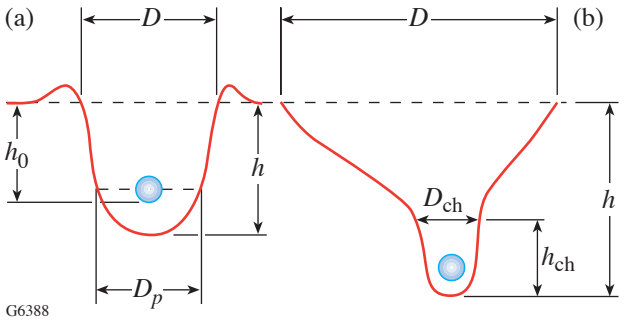

Figure 101.29
Cross-sectional profiles (not to scale) of (a) a regular crater and (b) a complex crater. Crater parameters measured by AFM: crater diameter D, crater depth h, crater channel diameter D_{ch}, channel depth h_{ch}, and crater width at particle-center position D_p.

This averaging allows variations to be smoothed out in the crater geometry for individual particle locations caused by the inhomogeneous thin-film environment. As shown earlier (see Ref. 7), variations in the particle/thin-film interface geometry strongly affect both absorption by the particle and energy transfer to the surrounding-film matrix. This effect is more pronounced at close-to-threshold conditions, when only particles with the best contact with the matrix are producing craters. At laser fluences many times exceeding threshold, the probability of crater formation is approaching 100% and, for regular craters, variation in crater size is significantly reduced.

Crater diameter versus fluence dependence for shallow lodging depths—30 nm and 60 nm—is presented in Fig. 101.30. In the case of the 60-nm lodging depth, it can be well approximated by a linear fit. More complex behavior is observed in the 30-nm case where, after a threshold jump, stagnation of diameter growth is measured in the fluence range of 0.6 to 4 J/cm^2. At higher fluences, almost exponential growth sets in, and at $F > 7$ J/cm^2, 30-nm and 60-nm curves tend to merge together.

An explanation for this behavior in the case of 30-nm lodging depth may be found in the coating geometry (see Fig. 101.31). The coating above the particle is growing like a nodule and forms a spherical bump with lateral size L for which AFM measurement (unirradiated site) gave an average value of 47 nm. This value fits well within crater diameter sizes of 35 to 50 nm measured in the fluence range of 0.6 to 4 J/cm^2. Together with the typical crater depth of ~30 nm this points to material removal within one nodular volume, indicated by the dashed line in Fig. 101.31. Shallow particle location and gold-silica thermal mismatch imply reduced strength of the coating within the nodular volume described above and lend support for the following explanation: Upon energy absorption from the laser pulse and particle heating, pressure applied to the portion of the coating above the particle may suffice for its ejection without melting of the surrounding matrix. With an increase in laser fluence, increased pressure leads to even faster ejection and, possibly, additional heating of the removed material, but still without reaching a critical temperature at the particle/matrix interface. Eventually, at a high-enough fluence (>4 J/cm^2), coupling to the surrounding matrix takes place before material ejection, leading to dramatic growth in crater size. In the case of 60-nm lodging, a similar

stagnation range exists, though over a very narrow fluence range of 0.5 to 0.8 J/cm^2. As one can notice, crater-diameter growth with fluence in the cases of 30-nm and 60-nm lodging (see Fig. 101.30) is much faster than $F^{1/3}$. This indicates that the plasma-ball saturation regime [see the **Theoretical Approach to Crater Formation** section (p. 27)] is not reached at fluences <8.1 J/cm^2.

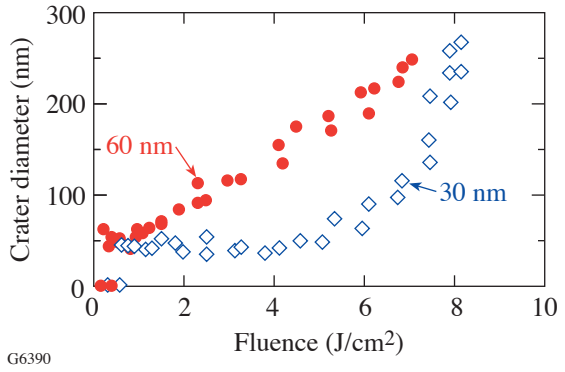

Figure 101.30
Crater diameter versus fluence dependence for shallow particle-lodging depths, 30 nm and 60 nm.

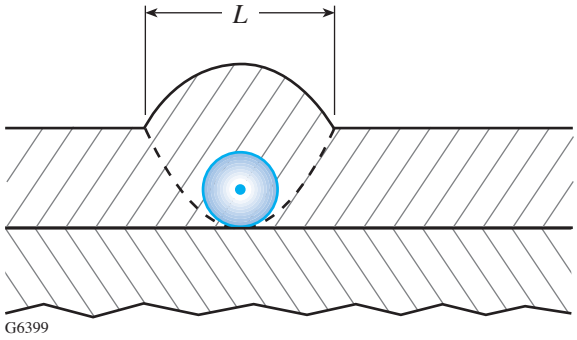

Figure 101.31
Thin-film geometry in case of 30-nm particle-lodging depth.

Crater diameter versus fluence dependence for 110-nm, 190-nm, and 240-nm lodging depths is depicted in Fig. 101.32, showing several features different from the case of shallow-lodging depth. The most notable difference is size. For instance, *at near-threshold conditions*, craters start with ~390-nm diameter for 240-nm lodging compared to ~35-nm diameter for 30-nm lodging. The reason goes beyond the trivial fact that at fluences just above threshold, deeper absorbers produce larger craters. More importantly, *different crater-formation processes* come into play with increasing lodging depth. Regular craters [Fig. 101.29(a)] originate from shallow locations and are formed through the processes of melting and vaporization. Complex craters [Fig. 101.29(b)] originate from deep locations and, in addition to melting and vaporization of the material in the channel volume, have a significant amount of the top part of the material removed through a *fracture mechanism*. The process of material removal through fracture is much more favorable energetically than volumetric vaporization. In the former case, energy goes to molecular bond braking in molecules associated only with a new surface compared to breaking bonds in the whole removed volume in the latter case. Even in the case when material removal proceeds through fragmentation (nanocluster formation), this picture holds.

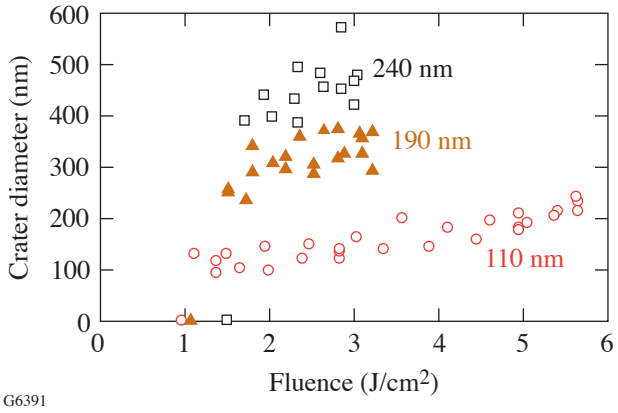

Figure 101.32
Crater diameter versus fluence dependence for 110-nm, 190-nm, and 240-nm lodging depths.

The growth of the crater diameter with fluence shows a lower growth rate for deep lodging depths, especially 190-nm and 240-nm lodgings. It can be understood considering the change in volume removed for each increment in crater diameter. At equal laser fluences, the same partial increment in the diameter will result in much larger volume removal for a large crater than for a small one. Consequently, it results in a larger fluence increment required for diameter increase and slower growth rate with fluence for larger craters.

The other feature in the $D(F)$ dependence for craters originating from deep (190-nm and 240-nm) particle locations (see Fig. 101.32) is a large variation in diameter. As was discussed earlier [see the **Damage Morphology** section (p. 24)], these craters are formed in a process involving fracture and ejection of the top portion of the coating. Due to the inhomogeneity of

the thin-film material, variation in local material strength and stress factors can significantly affect size and shape of the fracture-removed portion of the complex crater.

b. Crater-depth variation with fluence. Crater depth versus fluence behavior for 60-nm, 110-nm, and 190-nm lodging depths is presented in Fig. 101.33. At laser fluences slightly above threshold, crater-depth values are very close to the particle-lodging-depth values and deeper absorbers produce not only wider [see the **Crater-Diameter Variation with Fluence** section (p.28)] but also deeper craters. With fluence increase, however, the rate of depth growth with fluence is reduced with increasing lodging depth, which is clearly seen from power-law approximation of the $h(F)$ curves in Fig. 101.33. The explanation here is similar to the case of the $D(F)$ dependencies. Since crater volume is roughly proportional to h^3, deep craters require a larger fluence increment to achieve the same partial depth increment compared to shallow craters.

In the case of deep lodging depth (190 nm), the $h(F)$ dependence is much more deterministic than the $D(F)$ dependence, which is probably associated with the mechanism of complex-crater channel formation. The channel morphology suggests a channel-formation process very similar to the regular-crater formation involving phases of plasma-ball growth, melting, and vaporization. Comparison of channel geometry with regular crater geometry [see the **Features of Complex-Crater Channel Formation** section (p. 31)] lends strong support to this hypothesis.

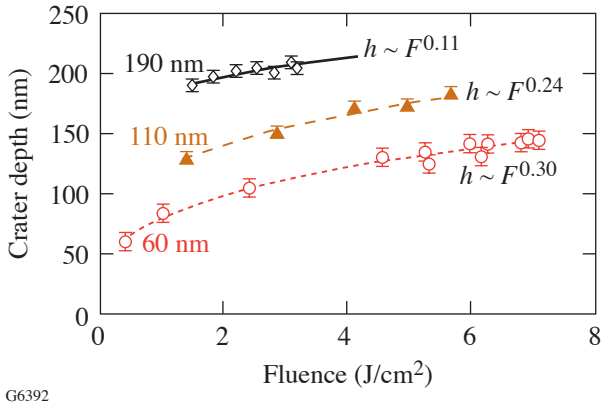

Figure 101.33
Crater depth versus fluence dependence for 60-nm, 110-nm, and 190-nm lodging depths.

c. Transformation of crater aspect ratio with fluence. One of the important features of crater growth with laser fluence is the modification in aspect ratio. Changes in aspect ratio are linked to the kinetics of energy deposition and dissipation processes.

Figure 101.34 depicts crater diameter/depth ratio versus fluence for 60-nm, 110-nm, and 190-nm lodging depths. In the case of 60-nm and 110-nm lodging depths, there is clear evidence that the crater diameter grows faster than the depth, *indicating that crater growth preferentially happens in the lateral dimension*. For 190-nm lodging depth, large scatter in data points and a relatively narrow fluence range prevent a definitive conclusion. This trend is highlighted further by Fig. 101.35, which shows cross-sectional AFM profiles for three craters generated from the 60-nm lodging depth at three different fluences: 1 J/cm^2, 2.4 J/cm^2, and 6 J/cm^2. Comparison of diameter ratios to depth ratios underscores the dominance of the lateral scale in crater growth: $D_3/D_1 = 3.5$ and $h_3/h_1 = 1.7$.

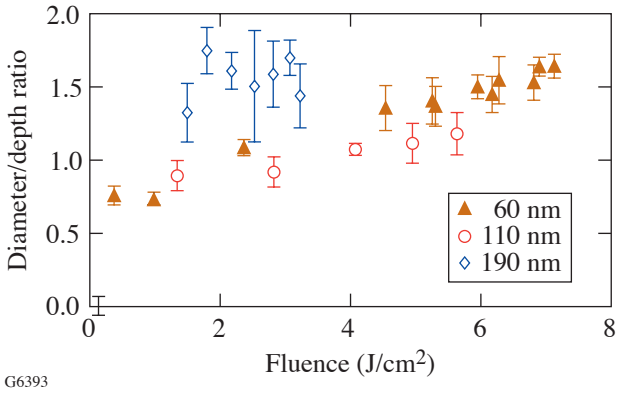

Figure 101.34
Crater-diameter to crater-depth ratio as a function of fluence for 60-nm, 110-nm, and 190-nm lodging depths.

An interesting observation is that the D/h aspect ratio grows faster for more-shallow 60-nm lodging compared to 110-nm lodging. A probable explanation may be linked to the fact that instantaneous temperature distribution in the material depends on the absorber lodging depth. For a shallow initiation point, the proximity of the adiabatic boundary (silica/air interface) means that heat propagating from the absorbing volume (plasma ball) will be caught at the boundary and eventually spread laterally. Since plasma-ball growth preferentially proceeds toward the adiabatic boundary due to irradiation geometry and screening effect (see Fig. 101.28), fluence

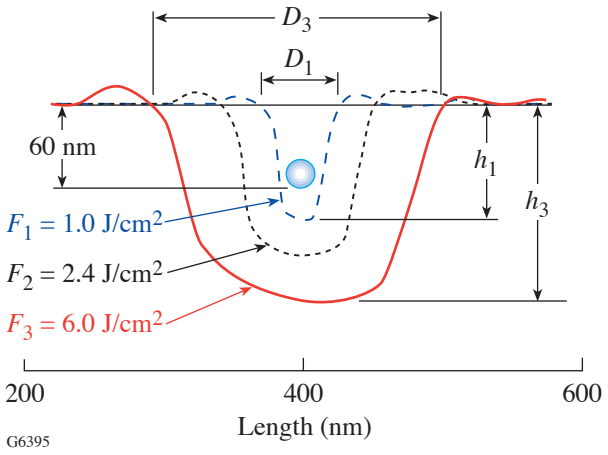

Figure 101.35
AFM-measured cross-sectional profiles for craters originated by particles with 60-nm lodging depth at fluences of 1.0 J/cm^2, 2.4 J/cm^2, and 6.0 J/cm^2. Crater growth with fluence is dominated by lateral scale.

increase should enhance lateral heat redistribution. For deep absorbers this effect may be less pronounced due to a more symmetric heat dissipation.

d. Features of complex-crater channel formation. To understand the mechanism of complex-crater formation, both channel diameter D_{ch} and depth h_{ch} [Fig. 101.29(b)] are measured as functions of fluence for 190-nm lodging. The results are plotted in Fig. 101.36 together with diameter and depth data (Figs. 101.30 and 101.33) for regular craters initiated by absorbers with 60-nm lodging. The striking agreement is seen for both diameter [Fig. 101.36(a)] and depth [Fig. 101.36(b)] values: channel data overlap well with regular-crater curves. This result lends support to a channel-formation mechanism through similar processes of melting and vaporization as in regular-crater formation. It also indicates that a *major part of the energy deposition in a complex crater takes place in the channel volume and goes into channel formation*. This immediately brings up a question about mechanism of the fracture generation leading to the removal of the complex crater's upper part. The most probable candidate here is a shock wave generated during localized heating by a 0.5-ns laser pulse.

It is also useful to compare channel dynamics with the dynamics of the whole complex crater. For this purpose, D_{ch} and h_{ch} are normalized to their counterparts of the whole crater and plotted as a function of fluence in Fig. 101.37. Both dependencies show growth, which provides circumstantial evidence that plasma-ball and melt-front-propagation velocity in the channel exceeds the fracture velocity in the studied range of fluence.

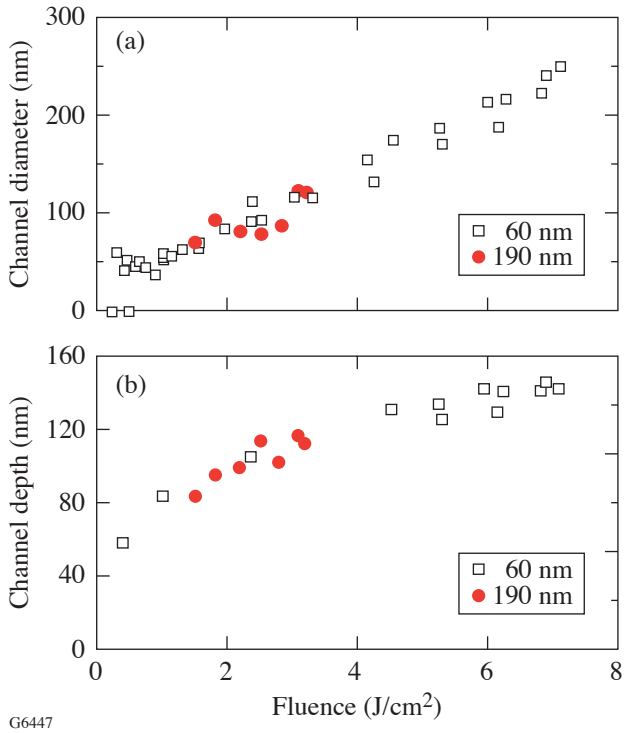

Figure 101.36
Complex-crater-channel diameter and depth variation with laser fluence: (a) channel diameter and (b) channel depth. Data for craters initiated by particles with 190-nm lodging depth are interleaved with data for regular craters originated by particles with 60-nm-deep location (see Figs. 101.30 and 101.33).

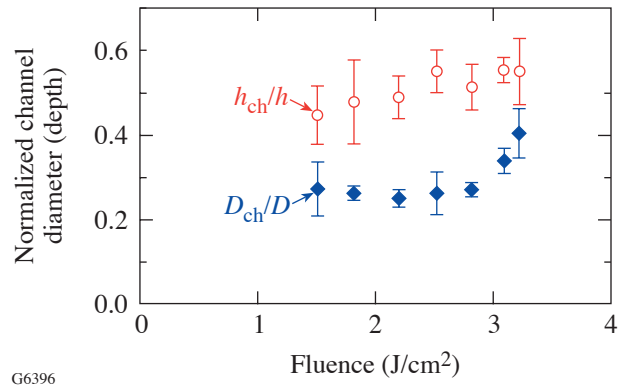

Figure 101.37
Channel diameter/crater diameter and channel depth/crater depth ratios as functions of fluence.

5. Estimates of Plasma-Ball Scale

Estimating the size of the plasma ball using only AFM data on crater geometry is not a straightforward task. Due to the dynamic nature of crater formation, the final shape of the regular crater is the result of interplay between processes of energy deposition, dissipation, hydrodynamic motion, and evaporation of the material. From this point of view, crater width at the particle-center position (see Fig. 101.28) is only remotely connected to the plasma-ball diameter. Nevertheless, with an increase in fluence and plasma-ball growth, part of the deposited energy used for crater formation will also grow due to the reduced role of dissipation processes (surface-to-volume ratio). It allows the use of crater width at the particle-center position D_p in the upper limit of fluence range as an estimate for the plasma-ball size. D_p values for 60-nm and 190-nm lodging are depicted in Fig. 101.38 as a function of fluence. In the case of 60-nm lodging, D_p shows linear growth and reaches a maximum value of ~180 nm at a fluence of ~6 J/cm^2 (~13 times threshold). According to phenomenological theory [see the **Theoretical Approach to Crater Formation** section (p. 27)], plasma-ball growth saturates upon reaching a size comparable with laser wavelength in SiO_2 film, $\lambda_f = 351/n_f \sim$ 250 nm (n_f, film refractive index ≈ 1.4). Both the maximum measured value of $D_p \sim 180$ nm ≈ $3/4\lambda_f$ and the linear behavior of $D_p(F)$ suggest that plasma-ball growth is not reaching its saturation regime within the investigated fluence range.

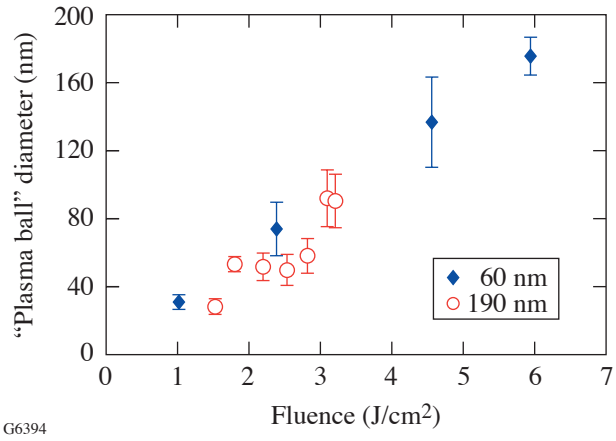

Figure 101.38
Estimate of plasma-ball size. Crater width at the particle-center position taken as a function of fluence for the particle-lodging depths of 60 nm and 190 nm.

6. Scaling Relations

There are two lodging-depth cases where the crater is not formed: the first case is where the lodging depth is so large that the pulse energy deposited in the material is not enough to create a crater; the second case is zero depth, where the defect can experience desorption without any modification of the film. At all intermediate locations, craters can be formed and the theory predicts a "bell"-shaped curve for crater diameter versus lodging depth dependence, in agreement with Eq. (3).

Our previous attempt to check scaling relations[11] with 8.4-nm particles showed qualitative agreement with theory, although only three relatively shallow lodging depths (10 nm, 30 nm, and 48 nm) were available at the time.

In this work, crater diameter was measured as a function of lodging depth at a fixed laser fluence of 1.67 J/cm^2—the threshold fluence for the deepest lodging depth h_d = 240 nm. The results, normalized to h_d, are presented in Fig. 101.39 together with the theoretical curve predicted by Eq. (3). The departure from the theoretically predicted ("bell"-shaped) curve and shift in the peak position may be directly attributed to the change in the crater-formation mechanism with increasing lodging depth. The experimental curve shows clearly a transition taking place between 60-nm and 110-nm lodging depths and manifests the onset of the fracture-driven material removal. Significant change (4.3 times) in the diameter size for 190-nm lodging (h/h_d = 0.79) compared to 60-nm lodging (h/h_d = 0.25) points to the energetic preference of the fracture mechanism compared to melting and vaporization.

Figure 101.39 also shows surprisingly close agreement between the experimental maximum value of normalized crater size D/h_d = 1.25 and the theoretically predicted ≈ 1.2 value [see Fig. 101.39 and Eq. (4)]. Further investigations of scaling relations, preferably with only one dominating mechanism of crater formation, should test the strength of this result.

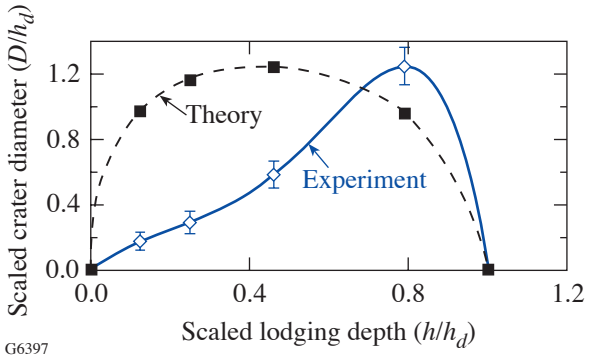

Figure 101.39
Scaled crater diameter versus scaled particle-lodging depth. Experimental data are taken at fluence 1.67 J/cm^2, corresponding to the crater-formation threshold for lodging depth h_d = 240 nm.

Conclusions

1. High-resolution investigation of 351-nm damage morphology in SiO_2 thin films with 18.5-nm gold nanoparticles serving as artificial, absorbing defects revealed submicrometer-scale craters as the main damage features.

2. Two different crater geometries are attributed to either (1) shallow absorbers and a melting/vaporization mechanism of crater formation, or (2) deep absorbers and complex-crater formation involving a combination of melting/vaporization *and* fracture.

3. The nanoscale thresholds (crater formation thresholds) increase with increasing particle-lodging depth, owing to the increased amount of energy required for craters to form.

4. At near-threshold conditions, craters initiated by deep absorbers are much larger than craters initiated from shallow depth mainly due to additional fracture-driven material removal from the top film layer. This mechanism is energetically much more efficient than melting and vaporization.

5. The growth of crater diameter and crater depth with laser fluence shows a higher rate for shallow absorbers compared to deep absorbers, which is explained by the difference in energy to be deposited to achieve the same partial increment in size.

6. Comparison with theoretical predictions for regular crater growth with fluence leads to the conclusion that the *saturation regime associated with the 1/3 power law is not reached* in the fluence range <8.1 J/cm^2. This conclusion is strongly supported by a plasma-ball-size estimate showing linear growth with fluence and reaching a value of ~3/4 of a wavelength for 60-nm lodging depth and an ~6-J/cm^2 fluence.

7. Analysis of crater-aspect-ratio variation with laser fluence proved that *crater growth with fluence is dominant in the lateral dimension*, especially in the case of shallow absorbers.

8. Investigation of complex-crater formation showed that the channel part of the crater is formed through melting and vaporization with geometry and size closely resembling a regular crater, provided fluence is the same. The rate of channel scale growth with fluence is exceeding the rate of growth of the complex crater as a whole, indicating that the major part of energy deposition takes place in the channel volume.

9. Scaling relations between crater diameter and absorber lodging depth are influenced by changes in crater-formation mechanism with increasing lodging depth. Good agreement with theoretical predictions is found for scaled maximum-diameter values. Further understanding of the crater-formation picture can be achieved with the help of numerical modeling (as reported in Refs. 18 and 19) with realistic temperature-dependent material parameters and absorbing-particle sizes.

ACKNOWLEDGMENT

The authors would like to thank P. A. Jaanimagi, R. Boni, and M. Millecchia for help with implementation of the CCD imaging system. This work was supported by the U.S. Department of Energy Office of Inertial Confinement Fusion under Cooperative Agreement No. DE-FC52-92SF19460, the University of Rochester, and the New York State Energy Research and Development Authority. The support of DOE does not constitute an endorsement by DOE of the views expressed in this article.

REFERENCES

1. S. Papernov and A. W. Schmid, J. Appl. Phys. **82**, 5422 (1997).

2. M. C. Staggs *et al.*, in *Laser-Induced Damage in Optical Materials: 1991*, edited by H. E. Bennett *et al.* (SPIE, Bellingham, WA, 1992), Vol. 1624, pp. 375–385.

3. R. J. Tench, R. Chow, and M. R. Kozlowski, in *Laser-Induced Damage in Optical Materials: 1993*, edited by H. E. Bennett *et al.* (SPIE, Bellingham, WA, 1994), Vol. 2114, pp. 415–425.

4. S. Papernov, A. W. Schmid, R. Krishnan, and L. Tsybeskov, in *Laser-Induced Damage in Optical Materials: 2000*, edited by G. J. Exarhos *et al.* (SPIE, Bellingham, WA, 2001), Vol. 4347, pp. 146–154.

5. S. Papernov, A. W. Schmid, A. L. Rigatti, and J. D. Howe, in *Laser-Induced Damage in Optical Materials: 2001*, edited by G. J. Exarhos *et al.* (SPIE, Bellingham, WA, 2002), Vol. 4679, pp. 282–292.

6. A. V. Hamza *et al.*, in *Laser-Induced Damage in Optical Materials: 2001*, edited by G. J. Exarhos *et al.* (SPIE, Bellingham, WA, 2002), Vol. 4679, pp. 96–107.

7. S. Papernov and A. W. Schmid, J. Appl. Phys. **92**, 5720 (2002).

8. F. Bonneau *et al.*, Appl. Phys. B **75**, 803 (2002).

9. H. Bercegol *et al.*, in *Laser-Induced Damage in Optical Materials: 2002*, edited by G. J. Exarhos *et al.* (SPIE, Bellingham, WA, 2003), Vol. 4932, pp. 297–308.

10. H. Bercegol *et al.*, in *High-Power Laser Ablation IV*, edited by C. R. Phipps (SPIE, Bellingham, WA, 2002), Vol. 4760, pp. 1055–1066.

11. S. Papernov and A. W. Schmid, in *Laser-Induced Damage in Optical Materials: 2002*, edited by G. J. Exarhos *et al.* (SPIE, Bellingham, WA, 2003), Vol. 4932, pp. 66–74.

12. F. Bonneau *et al.*, Appl. Phys. Lett. **83**, 3855 (2003).

13. A. During *et al*., in *Laser-Induced Damage in Optical Materials: 2003*, edited by G. J. Exarhos *et al*., (SPIE, Bellingham, WA, 2004), Vol. 5273, pp. 366–372.

14. M. D. Feit *et al*., in *Laser-Induced Damage in Optical Materials: 1997*, edited by G. J. Exarhos *et al*. (SPIE, Bellingham, WA, 1998), Vol. 3244, pp. 350–355.

15. M. D. Feit *et al*., in *Laser-Induced Damage in Optical Materials: 2000*, edited by G. J. Exarhos *et al*. (SPIE, Bellingham, WA, 2001), Vol. 4347, pp. 316–323.

16. P. Grua and H. Bercegol, in *Laser-Induced Damage in Optical Materials: 2000*, edited by G. J. Exarhos *et al*. (SPIE, Bellingham, WA, 2001), Vol. 4347, pp. 579–587.

17. P. Grua *et al*., Phys. Rev. B **68**, 035424 (2003).

18. F. Bonneau *et al*., in *Laser-Induced Damage in Optical Materials: 2000*, edited by G. J. Exarhos *et al*. (SPIE, Bellingham, WA, 2001), Vol. 4347, pp. 308–315.

19. F. Bonneau *et al*., Appl. Phys. B **78**, 447 (2004).

20. Yu. K. Danileiko, A. A. Manenkov, and V. S. Nechitailo, Sov. J. Quantum Electron. **8**, 116 (1978).

Minimizing Artifact Formation in Magnetorheological Finishing of CVD ZnS Flats

Introduction and Motivation

The development of optics for new applications is based on the use of materials that have the appropriate mechanical and optical properties. For infrared (IR) window and dome materials that protect imaging systems against damaging conditions, three main considerations are taken into account: material strength, thermal-shock resistance, and optical characteristics, such as transmission, absorption, scattering, and emissivity. To obtain maximum transmittance, a good IR material should exhibit minimum optical scattering due to a rough surface finish. The synthetic materials that meet the requirements for IR windows could be either single crystals or polycrystalline with cubic crystallographic structure, the latter being usually tougher, which is desired.[1] Polycrystalline ZnS is an excellent candidate for these applications.

The chemical vapor deposition (CVD) process was developed in the 1970s in response to the need for increased volumes of polycrystalline ZnS with improved transparency.[2] The CVD process takes place in a chamber similar to an autoclave at increased temperatures (600°C to 1000°C) and at pressures below 100 Torr. Deposits of solid grains are formed on the inside walls of a graphite mandrel. The size of the grains depends on the deposition temperature and has a dramatic impact on the mechanical properties, such as the erosion rate.[3]

Two types of CVD ZnS are available on the market from domestic sources: regular grade and multispectral grade. The first type has a grain size of about 2 to 8 μm, is yellow-orange in color, and is used in the 3- to 5-μm-wavelength and 8- to 12-μm-wavelength regions. The "multispectral (or 'water clear') grade" ZnS is colorless, exhibits high transmittance over a wider range of wavelengths, and can be used in the 0.5- to 12-μm region of the spectrum. This latter material undergoes a hot isostatic pressing (HIP) process to grow the grain size to 20 to 100 μm, eliminating microscopic voids and other internal defects; however, this refining process leads to a reduction in strength and erosion resistance of the clear material.

The CVD process offers many advantages over conventional techniques for preparing infrared transmitting materials, the most significant being the purity of the material, its minimized IR absorption, and the fact that the process is not size limited. A potential disadvantage of the process is that the CVD ZnS material, though it possesses a fine grain structure, contains a micro- to macroscopic inhomogeneous "nodular" structure, referred to as "hillocks" or "pebbles." Pebbles nucleate from dust and dust-like inclusions on the mandrel where substrate growth initiates. These then grow up from the bottom in the form of expanding "cones" through the bulk of a CVD ZnS puck.[4] They may reach several millimeters in size on the free surface.

The process of surface finishing is of great importance since the final surface quality has an impact on optical properties of a ZnS optic. Single-point diamond turning, a common method for finishing nonspherical surfaces, is especially effective with long-wave infrared materials (LWIR = 8 to 12 μm) like ZnS, ZnSe, and Ge. Magnetorheological finishing (MRF), described elsewhere,[5–7] is a deterministic polishing process that is now widely used in the production of high-precision optics around the world. The extension of MRF to a vast array of materials is possible because of the accommodating nature of this finishing process, which offers a wide range of removal rates required for the surface finishing of glasses, crystals, polycrystalline, and plastic materials. The objective of this work was to determine which aqueous magnetorheological (MR) fluid composition and conditions would provide the best polishing and smoothing performance on CVD ZnS flats that differed in initial surface preparation and source of supply. During this research the emergence of pebbles upon polishing with MRF was revealed. Suppression of these artifacts at the surface was accomplished by changing the composition of the MR fluid.

Experimental Details

MR fluids were prepared with a variety of magnetic and nonmagnetic ingredients. Two types of magnetic carbonyl iron (CI) particles were evaluated. Each type was spherical in shape

with an average particle size of ~4 μm. One type was mechanically "hard", and the second was mechanically "soft".[8] Four nonmagnetic polishing abrasives were evaluated: cerium oxide, diamond, alumina, and silica. Table 101.IV lists the attributes of these abrasives. Abrasive size was difficult to ascertain. It depended on milling time during use for those abrasives that were strongly agglomerated. These abrasives were used previously in experiments on MRF of polymers.[9]

CVD ZnS from two manufacturers—"regular grade" from II-VI, Inc.,[10] and "high-quality" material from the Research Institute of Synthetic Crystal, Beijing[11]—were used in the experiments. Samples were provided in the form of 35- to 40-mm-diam pucks that were 8 to 20 mm thick. Surfaces were used as prepared by outside sources or after additional processing in-house.

Spotting and polishing experiments with uniform removal (successive dc polishing runs) were conducted on a Q22Y MRF polishing machine.[12] Peak and volumetric removal rates were calculated using interferometric data obtained on a Zygo GPI phase-shifting interferometer.[13] Polishing performance of the various MR fluids was evaluated by measuring the removal rate, the final surface roughness (p–v and rms), and the visual appearance of the surfaces after polishing runs.

The evolution of surface morphology and texture was determined using a Zygo New View5000 White Light Optical Profilometer.[14] This instrument quantifies microroughness and reveals surface defects. Two types of objectives were used for the analysis: a 20× Mirau (with a 0.26-mm × 0.35-mm image size) and a 2.5× Michelson (with a 2.11-mm × 2.81-mm image size for 1× zoom and 5.38 mm to 7.17 mm for a 0.4× zoom) with no digital filter applied. The higher magnification allowed for the evaluation of areal rms and p–v surface roughness, while the lower magnification was useful for studying the extent and shape of pebble-like surface artifacts.

Five initial surface states were investigated: deterministically microground, single-point diamond turned, and after pitch-polishing in-house (for ZnS from II-VI); "as received" and after pitch-polishing in-house (for ZnS from China). Pitch-polished surfaces were prepared in-house in a four-step process: controlled loose-abrasive grinding (40 μm of alumina on cast iron, 20 μm of alumina on glass, and 9 μm of alumina on glass) followed by polishing on a beeswax/Gugolz73 lap (10%/90%) with a 50/50 acidic mixture of 0.3 μm of alumina/colloidal silica. Resulting surfaces were flat to better than 0.5 μm p–v, with areal surface roughnesses as good as 10 nm p–v and 0.5-nm rms.[15]

The deterministically microground surfaces were prepared in-house using a three-step protocol consisting of computer numerically controlled removal with three diamond ring tools: rough (220 μm in bronze), medium (15 μm in bronze), and fine (3 μm in resin). Surface-roughness levels after grinding were ~400 nm p–v and ~20-nm rms.

Table 101.IV: Abrasive particles used in MR fluids for CVD ZnS polishing.

Dry Abrasive	pH in DI Water	Primary Particle Size[(b)]	Median Size[(c)]	Comments
CeO_2	—	40 nm	96 nm	[(b)]Provided as 20.9-wt.% solids in pH7.4 solution
Diamond[(a)]	2.5	4 nm	1.4 μm	Milling in an MRF machine increased vol % of particles <0.6 μm from 0.5 to 21 in 7 days
Al_2O_3 γ phase	4.7	33 nm	93 nm	Milling in an MRF machine increased vol % of particles <225 nm from 0 to 75 in 24 h
SiO_2	4.7	40 nm	—	[(b)]Amorphous, fumed, hydrophilic

[(a)]Standard MR fluid constituent; [(b)]information supplied by vendor; [(c)]powder dispersed in DI water with a surfactant and intensively sonicated prior to sizing.

Samples of CVD ZnS from II-VI were single-point diamond turned (SPDT) by an outside vendor;[16] surface-roughness levels after SPDT were 33±6 nm p–v and 6.4±1.0-nm rms.[15] A typical lineout of an SPDT surface is shown in Fig. 101.40. Over a distance of 300 μm one can see the fine diamond-turning marks (spatial periodicity of ~8 μm), superimposed on undulations with large amplitudes and periods of over 100 μm. Power spectral density (PSD) analyses were conducted on these surfaces before and after MRF to track the evolution of these features (described later).

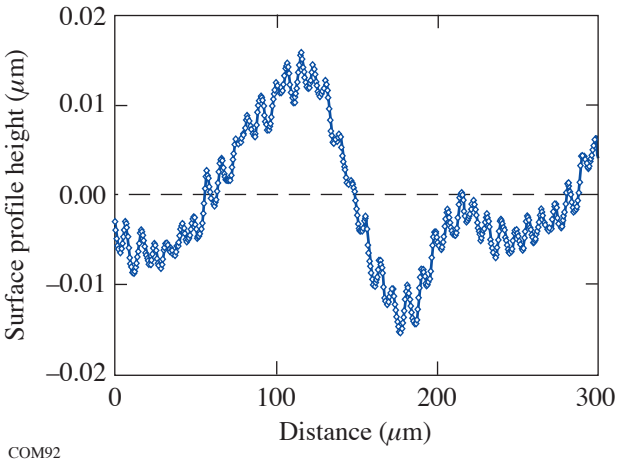

Figure 101.40
The initial surface profile of an SPDT surface on CVD ZnS used in this work.

Some of the CVD ZnS parts manufactured in Beijing were used as received from China (specular surfaces with an areal surface roughness of 300±155 nm p–v and 8.8±0.5-nm rms).[15] Others were used after polishing in-house on pitch (areal-surface roughness of 10±3 nm p–v and 0.8±0.0-nm rms).[15]

No discussion has been found in the literature regarding the relevance of pebble-like structures on CVD ZnS used in IR applications. Since the CVD process imposes rather different growing conditions as the growth surface extends out from the mandrel, care was taken to keep track of CVD ZnS surfaces. The sides of the ZnS pucks that were in contact with the growth mandrel were designated S1 (more yellow coloration), and the sides farthest away from the mandrel were designated S2 (more orange in color).

The work described here consisted of three phases: Experiments were first conducted on the in-house pitch-polished surfaces of CVD ZnS from II-VI. The immediate goal was to identify the optimal nonmagnetic abrasive from the four types of powders in tests with hard CI. S1/S2 side-related effects were studied on 20-mm-thick flats. Secondly, magnetic-particle type and MR fluid chemistry were further altered to make additional improvements in the final surface roughness. Finally, the polishing performance of the altered fluid was evaluated on the four types of surfaces previously described, for both the domestic and foreign-made ZnS materials.

Nonmagnetic Abrasive Study (Phase 1)

MR fluids using hard CI were prepared with each of the four nano-abrasives from Table 101.IV, which differ in particle hardness (from soft silica particles to hard diamond ones), as well as in the particle surface chemistry. This latter characteristic affects fluid rheology, thus setting individual limits for the maximum abrasive content that can be used. MRF trials with each of these abrasives were conducted on the same part and surface (S2). The part was repolished on pitch before each successive trial.

The results of these experiments are presented in Figs. 101.41 and 101.42. Figure 101.41 tracks the evolution of surface microroughness as a function of material removed. Figure 101.42 shows the peak removal rate achieved for a given abrasive concentration and the level of p–v surface roughness after removing 1 μm of material.

The highest removal rate along with the least degradation to surface roughness was provided by the hard CI-based MR fluid with >1.0 vol% of alumina; the removal rate observed for the fluid with nanodiamond was quite similar to that for

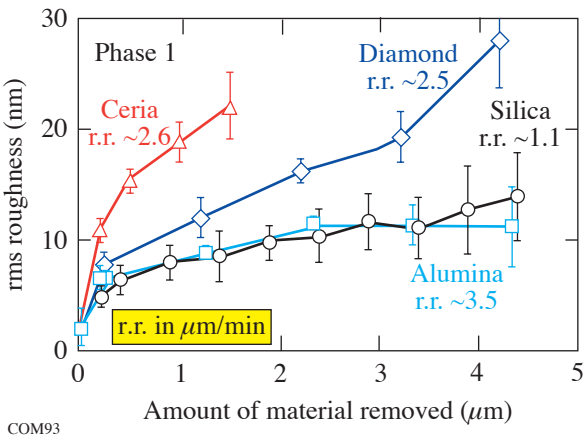

Figure 101.41
Evolution of rms surface roughness with the amount of material removed during dc polishing of pitch-polished CVD ZnS with a hard CI-based fluid prepared with each of four different abrasives.

the ceria-based MR fluid, which was almost two times higher than the removal rate provided by the silica-containing fluid. These results clearly demonstrate the dramatic difference in abrasive polishing efficiency on ZnS, independent of the abrasive concentration. (It was not possible to relate removal rates to the number of abrasive particles of a given abrasive type because of issues of aggregation and agglomeration previously discussed relative to Table 101.IV.)

The two abrasives, ceria and diamond, provided similar removal rates with drastically different surface-roughness characteristics. As shown in Fig. 101.41, rms surface roughness increased dramatically from 2.7 nm for the initially pitch-polished surface up to 11 nm after polishing out 0.2 μm of material with the ceria-based MR fluid. Roughness continued to increase after every subsequent polishing run and approached 22-nm rms with the cumulative removal of 1.5 μm. Roughness values grew slowly but steadily when using diamond abrasives, exceeding 25-nm rms after the removal of 4 μm. Silica and alumina abrasives caused less surface degradation. The silica-based MR fluid provided relatively lower roughness levels with the rms leveling out at around 11 nm after removing as much as 3.5 μm of material. However, this abrasive demonstrated a tendency for increasing roughness with further polishing. The results obtained for the alumina-based fluid were quite similar to those of the silica-based fluid, with rms not exceeding 11 nm after polishing out more than 2 μm. Root-mean-square roughness remained at this same level after polishing out another 2.5 μm of material. Moreover, the p–v surface characteristics showed the lowest values as well. The alumina-based fluid was chosen for further experiments due to its 3.5×-higher removal rate than the silica, a low level of surface roughening, and its excellent rheological properties.

Pebbles were first observed on the S2 surface of the CVD ZnS puck after the first 0.5-μm dc polishing runs were made, regardless of the type of abrasive used. The emergence of pebbles on S2 became more noticeable to the eye after each subsequent polishing run; however, the quantification of these topographic features was difficult to document since they caused no increase to the surface roughness measured with either 20× or 2.5× objectives. On S1, the situation was different. Pebble-like features became noticeable to the eye only with removal of over 1.5 μm of material. As they emerged with additional polishing, the features on S1 exhibited a different shape, areal density, and intensity than those on S2.

Images of S1 and S2 on a 20-mm-thick CVD ZnS puck after 1.5 μm of material was polished out from an initially pitch-polished ZnS surfaces were obtained using a laser interferometer (40-mm aperture) and a white-light interference microscope (2.5×: 7.2-mm × 5.4-mm area). The images are presented in Fig. 101.43 and clearly demonstrate the pronounced difference

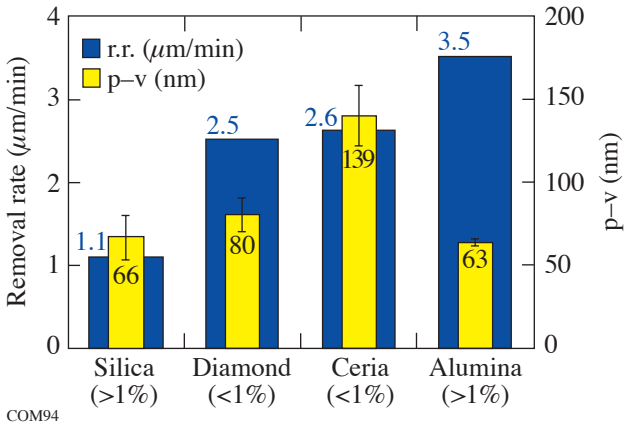

Figure 101.42
The removal rates and p–v surface-roughness values measured after polishing out 1 μm of material with hard CI-based fluids prepared with four different abrasives. Approximate abrasive concentration is indicated in volume percent.

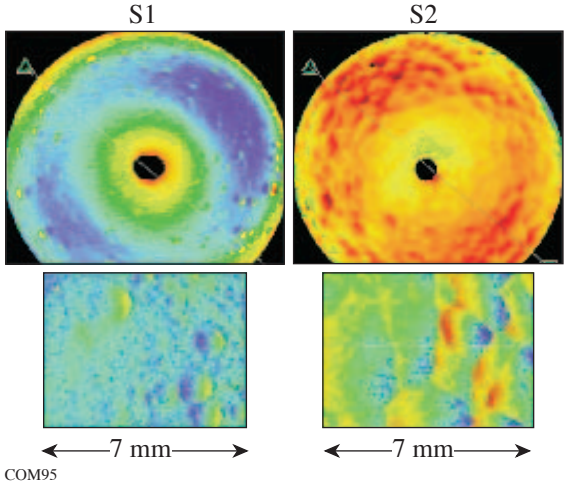

Figure 101.43
Laser interferometer images (40-mm aperture) and white-light interferometer intensity maps (2.5×, 7.2-mm × 5.4-mm field) for two opposite sides of a 20-mm-thick CVD ZnS puck after polishing out 1.5 μm of material by a hard CI-based nanoalumina fluid.

in the shape and density of the artifacts. Pebbles on S1 resemble distinct, separated craters, having a circular shape with a diameter smaller than 1 mm, while the pebbles observed on S2 appear as large, overlapped petals of a flower. The features on S2 are quite different in size, with some being larger than 5 mm across. In terms of visual appearance, the S2 side showed significant decoration to the eye, whereas S1 looked nicely polished with no observable artifacts. These micro- and macrostructures fit previous descriptions and microphotographs of CVD ZnS that indicate cones of material growing up and away from S1 (mandrel/side) toward S2 (free side).[4]

Composition and Chemistry Alterations (Phase 2)

The necessity for making further improvements to surface roughness and surface visual appearance resulted in the second phase of our experiment, during which MR fluid composition and chemistry were altered employing alumina as the nonmagnetic polishing abrasive. Use of a soft type of CI improved long-term stability of the altered alumina-based fluid and provided removal rates of ~1 μm/min. Additional alterations of fluid chemistry gave very beneficial results. The evolution of p–v and rms surface roughness as a function of material removed by these MR fluids with soft CI and altered chemistry are plotted in Figs. 101.44(a) and 101.44(b) for initially pitch-polished surfaces. The use of soft CI led to the noticeable improvement in the surface roughness although there was a 3× reduction in the removal rate from phase 1. The alteration of both CI type *and* chemistry lowered the surface roughness to below 20 nm p–v and 2-nm rms after polishing out as much as 2 μm of material from an initially pitch-polished surface. Further polishing to remove a total of 3.5 μm led to a modest increase in both roughness parameters to 25 nm p–v and 2.5-nm rms.

The other significant advantage of using the altered fluid was the fact that no pebbles were observed on either S1 or S2 [see Fig. 101.44(c)], providing good visual appearance after polishing out a total of 3.5 μm. These results made the chemically altered, alumina-based, soft-CI MR fluid an advantageous choice for figure correction of prepolished CVD ZnS.

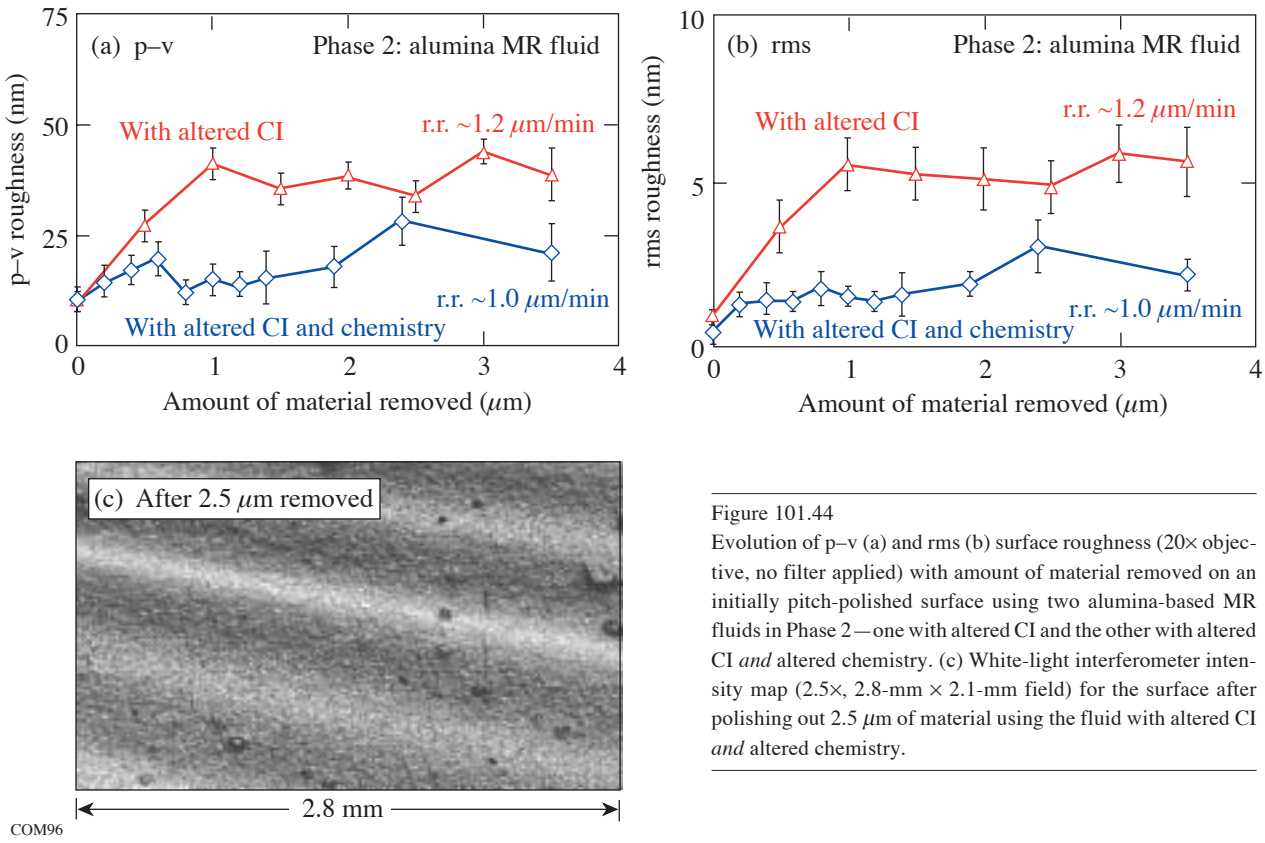

Figure 101.44
Evolution of p–v (a) and rms (b) surface roughness (20× objective, no filter applied) with amount of material removed on an initially pitch-polished surface using two alumina-based MR fluids in Phase 2—one with altered CI and the other with altered CI *and* altered chemistry. (c) White-light interferometer intensity map (2.5×, 2.8-mm × 2.1-mm field) for the surface after polishing out 2.5 μm of material using the fluid with altered CI *and* altered chemistry.

The Effect of Initial Surface Preparation (Phase 3)

The effect of initial surface preparation on the polishing and smoothing performance of MRF was studied using the chemically altered, alumina-based, soft-CI MR fluid on five types of CVD ZnS surfaces from the two manufacturers described earlier.

The removal rate was measured to be 1.2 to 1.4 μm/min with no significant dependence on the initial surface preparation in the tested range of initial roughness parameters. The evolution of roughness with the amount of material polished out from domestic CVD ZnS with different initial surface preparation is presented in Figs. 101.45(a) and 101.45(b). Similar roughness levels were achieved on all three tested surfaces after polishing out 2 μm of material, with the p–v falling to below 20 nm and the rms going below 2 nm. This was accomplished despite the fact that p–v values for the initial surfaces were in a range that varied from 10 nm p–v for the pitch-polished surface to more than 400 nm p–v for the microground surface. This result is of great importance for the MRF process because it widens the range of initial surface conditions that can be processed. The other noteworthy result is that no signs of surface decoration (e.g., pebble-structure formation) were observed on any surfaces of ZnS after removing up to 4 μm of material.

The surface of an SPDT ZnS part before and after MRF polishing was examined using PSD analysis of lineouts from roughness scans. This analysis is useful for showing the evolution of various spatial frequencies in the surface. The initial surface exhibited primary peaks in power density (e.g., diamond-turning grooves) with several periodicities between 8 μm and 15 μm (spatial frequencies from 1.2×10^{-4}/nm to 7×10^{-5}/nm), with a broad secondary peak (grooves presumably caused by misalignment or chatter) between 100 μm and 500 μm (spatial frequencies from 1×10^{-5}/nm to 2×10^{-6}/nm).

The PSD data in Fig. 101.46 demonstrate that the primary diamond-turning grooves (8 to 15 μm) were eliminated after the removal of only 0.2 μm of material. Removal of 1 μm was sufficient to decrease the signature near 200 μm (5×10^{-6}/nm) by over on order of magnitude. This demonstrated ability of MRF to reduce the intensity and even eliminate the periodic

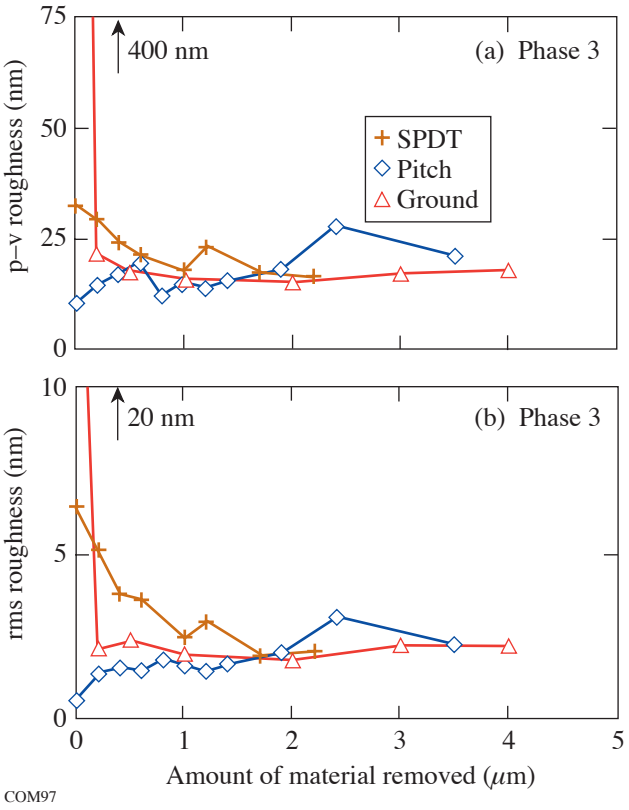

Figure 101.45
Evolution of p–v (a) and rms (b) surface roughness with the amount of material polished out for three types of initial surfaces—pitch-polished, ground, and SPDT—using the chemically altered, soft-CI MR fluid (domestic material from II-VI, Inc).

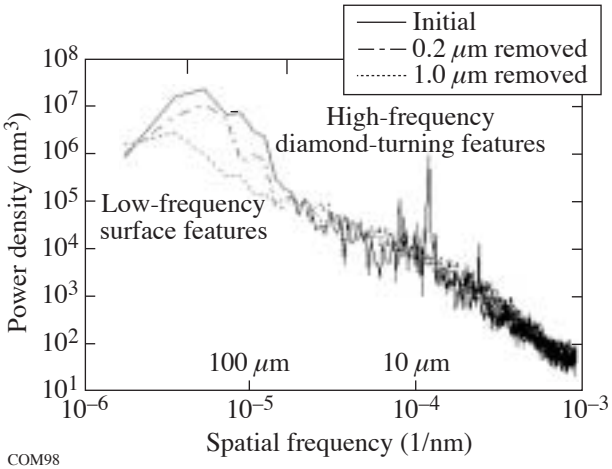

Figure 101.46
PSD plots on an SPDT ZnS surface showing the removal of high-frequency diamond-turning grooves after polishing out 0.2 μm of material. Additional polishing reduced the power density of low-frequency artifacts by 10×.

marks of different frequencies, accompanied by a dramatic improvement in surface roughness without introducing artifacts, makes the altered MR fluid a strong candidate for improving SPDT surfaces of CVD ZnS.

CVD ZnS manufactured in Beijing was evaluated in a series of dc polishing runs using the chemically altered, soft-CI MR fluid. Both as-received surfaces and surfaces prepolished in-house on pitch were processed with MRF without uncovering any surface artifacts. As shown in Fig. 101.47, it was impossible to improve the roughness of as-received surfaces (initial: 300 nm p–v/9-nm rms) to less than 30 to 40 nm p–v/5-nm rms. Starting from an in-house pitch prepolish, however, it was possible to bring the Chinese material to p–v and rms roughness levels comparable to those achieved for the domestic material.

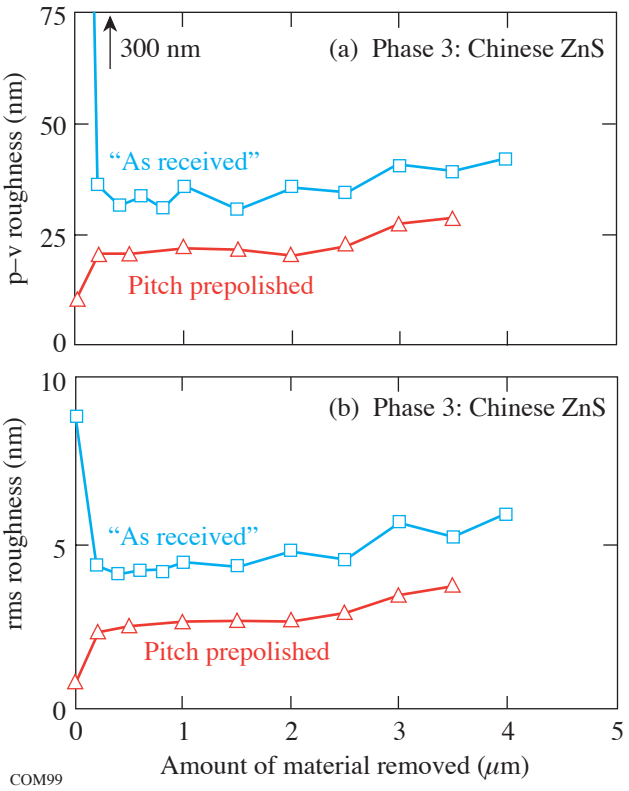

Figure 101.47
Evolution of p–v (a) and rms (b) surface roughness with the amount of material removed for CVD ZnS from China using chemically altered, soft-CI MR fluid. Two initial surfaces were used in the experiment: as received and after in-house prepolishing on pitch.

Summary

The finishing performance of magnetorheological (MR) fluids prepared with a variety of magnetic and nonmagnetic ingredients was studied on CVD ZnS flats from different manufacturers. Surfaces studied were used as received, after polishing on pitch, after single-point-diamond-turning (SPDT), and after deterministic microgrinding. MR polishing using hard CI and standard MR fluid chemistry yielded a surface with high roughness and pebble-like structures. The severity of pebble-like decoration was shown to be related to the processed side of the ZnS puck. Pebbles were more pronounced on the free surface farthest from the graphite growth mandrel. Experiments on pitch-polished surfaces showed nanoalumina abrasives to be the least detrimental of four nanoabrasives tested. These abrasives were then combined with soft CI and altered MR fluid chemistries to enable several microns of ZnS material to be removed with suppression of pebble-like decoration. Surfaces that were initially microground, diamond turned, or pitch polished were all processed with this altered MR fluid to ~20 nm p–v and 2-nm rms. Diamond-turning marks were eliminated.

REFERENCES

1. R. Lane and B. Battat, Advanced Materials and Processes Technology Information Analysis Center (AMPTIAC), **AMPT-18,** IIT Research Institute, Rome, NY, Contract No. SPO700-97-D-4001 (December 1999).

2. H. H. Karow, *Fabrication Methods for Precision Optics* (Wiley, New York, 1993), Chap. 2.

3. C. S. Chang, J. L. He, and Z. P. Lin, Wear **225**, 115 (2003).

4. K. L. Lewis, A. M. Pitt, and J. A. Savage, in *Proceedings of the Ninth International Conference on Chemical Vapor Deposition 1984*, edited by Mc. D. Robinson *et al.* (Electrochemical Society, Pennington, NJ, 1984), pp. 530–545.

5. S. D. Jacobs, S. R. Arrasmith, I. A. Kozhinova, L. L. Gregg, A. B. Shorey, H. J. Romanofsky, D. Golini, W. I. Kordonski, P. Dumas, and S. Hogan, Am. Ceram. Soc. Bull. **78**, 42 (1999).

6. D. Golini, in *Precision Science and Technology for Perfect Surfaces*, edited by Y. Furukawa, Y. Mori, and T. Kataoka, JSPE Publication Series No. 3 (The Japan Society for Precision Engineering, Tokyo, Japan, 1999), pp. 132–137.

7. S. D. Jacobs, S. R. Arrasmith, I. A. Kozhinova, S. R. Gorodkin, L. L. Gregg, H. J. Romanofsky, T. D. Bishop II, A. B. Shorey, and W. I. Kordonski, in *Initiatives of Precision Engineering at the Beginning of a Millennium*, edited by I. Inasaki (Kluwer Academic Publishers, Boston, 2001), pp. 501–505.

8. A. B. Shorey, S. D. Jacobs, W. I. Kordonski, and R. F. Gans, Appl. Opt. **40**, 20 (2001).

9. J. E. DeGroote, H. J. Romanofsky, I. A. Kozhinova, J. M. Schoen, and S. D. Jacobs, in *Manufacturing and Testing V*, edited by H. P. Stahl (SPIE, Bellingham, WA, 2004), Vol. 5180, pp. 123–134.

10. II-VI, Inc., Saxonburg, PA 16056-9499.

11. Research Institute of Synthetic Crystals State Administration of Building Materials, Industry, Beijing, Peoples Republic of China.

12. Q22Y, Commercial MRF machines manufactured by QED Technologies, LLC, Rochester, NY 14607.

13. Zygo GPIxpHR phase shifting interferometer system, Zygo Corporation, Middlefield, CT 06455.

14. Zygo New View™ 5000 White Light Optical Profilometer, Zygo Corporation, Middlefield, CT 06455.

15. New View™ 5000 setting for roughness measurements with 20× objective: scan length: 20 μm bipolar; min. mode: 5.0%; min. area size: 7; FDA: high. The reported roughness values are the average of eight to ten measurements at different sites.

16. Corning NetOptix, Diamond Turning Division, Keene, NH 03431.

A Multichannel, High-Resolution, UV Spectrometer for Laser-Fusion Applications

Introduction

The 60-beam OMEGA laser system is used for inertial confinement fusion (ICF) studies.[1] The configuration of each of the 60 beams should be exactly the same to produce the most-uniform ICF implosions.[2] A shaped infrared (IR) (λ = 1053 nm) pulse is generated from a single master oscillator and fed into 60 beamlines with large Nd:glass amplifiers.[3] Each beamline produces approximately 800 J of IR light in a 1-ns pulse. The frequency of the IR light is tripled in a series of KDP crystals to produce UV light at 351 nm, which is used to illuminate the ICF target. An important feature of this laser system is that spectral broadening can be deliberately imposed on the emitted radiation using a technique called smoothing by spectral dispersion (SSD).[4] This is done to produce a more-uniform, time-integrated illumination profile at the target. The imposed bandwidth has a width of 1.2 nm in the IR, which exceeds the acceptance bandwidth of the potassium dihydride phosphite (KDP) crystals used for frequency tripling.[5] To overcome this problem, each beam has two tripling crystals that are angularly detuned with respect to the direction of propagation.[6] The acceptance bandwidth of the combined crystals is large enough to efficiently convert the SSD pulses. To maintain the highest conversion efficiency, the angular detuning of the KDP crystals must be controlled to approximately 100 μrad. Mistuned crystals decrease the UV conversion efficiency and change the spectra of the converted light. A procedure has been developed to tune the crystals by looking at the conversion efficiency on nine laser shots; however, the tuning can drift with time, and checks of individual beamlines have revealed that the spectra were different. Figure 101.48 illustrates the differences in spectra between two beamlines. To facilitate a more-accurate tuning procedure, a spectrometer was built to measure the UV spectra of all 60 beams on all OMEGA shots. This article describes that spectrometer.

In addition to the bandwidth imposed by the SSD system, there is an intrinsic source of bandwidth on the OMEGA system. If the intensity of a laser pulse varies rapidly in time, the nonlinear index of refraction produces a time-varying phase.[7] The time-varying phase produces a wavelength shift. The spectral structures associated with these intrinsic wavelength shifts have typical widths of 3 picometers (pm). The ability to understand and control this intrinsic bandwidth was a secondary motivation for building this spectrometer.

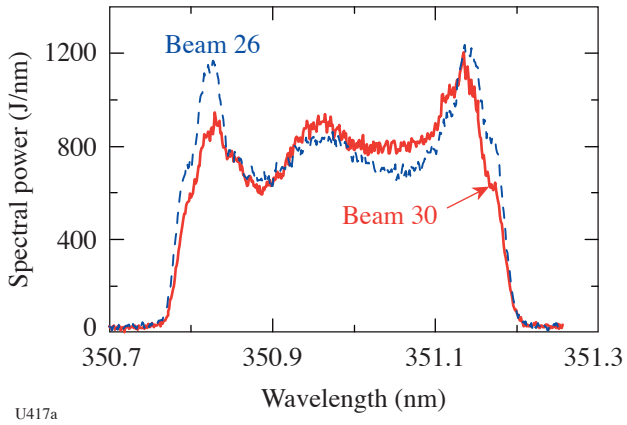

Figure 101.48
The spectra, with SSD on, vary from beam to beam on the same shot. The dashed curve is for beam 26 on shot 35711, and the solid curve is for beam 30 on the same shot.

The dual missions mentioned above determined the specifications of the spectrometer that was constructed. The spectrometer had to be able to acquire at least 60 complete spectra in a single shot. To allow for the possibility of corrupt channels and to incorporate *in-situ* wavelength calibration, an imaging spectrometer was constructed to accommodate 63 channels. Each channel must span a 0.5-nm bandwidth around λ = 351.01 nm to be capable of viewing the entire SSD-broadened spectra. With SSD turned off, the spectrometer must be able to resolve spectral features of the order of 3 pm. The light that feeds the spectrometer will come from a small fraction of the light from each beamline that is split off for diagnostic purposes (about 1 μJ on a full-energy shot). The total UV energy per beamline on OMEGA can range from 10 to 500 J. The fraction of light that is split off is linearly dependent on the total beam energy, so the detection system must be able to accommodate signal levels that vary by a factor of 50.

Spectrometer Layout

The physical layout of the spectrometer is shown in Fig. 101.49. The input to the spectrometer comes from 60 fiber bundles. Each fiber bundle consists of three 300-μm, UV-transmitting, step-index fibers.[8] The fiber bundles are attached to an integrating sphere, which is illuminated with a portion of the light from each beamline. Three fibers are used to increase the light coupled out of the integrating sphere. The fiber bundles attach to an input manifold. Within the manifold, three fibers from each bundle are realigned into a linear array and coupled into a UV-transmitting, fused-silica bar $10 \times 1.2 \times 0.4$ mm^3, along the 1.2-mm dimension. The bar, which is aluminized on all four sides with a 10-mm edge, acts as an optical homogenizer via multiple reflections off the metallized sides. The light emerging from the fiber should be approximately spatially uniform and have a Gaussian dependence on angle. The homogenizer will cause the high-angle rays that have the lowest uniformity to undergo at least two reflections from the sides, thus increasing the uniformity of the output radiation. This assembly constitutes a single channel, which is the input to the spectrometer. Twenty-one of these channels are arranged in a line. The center channel is fed with a neon pencil lamp, which provides a wavelength fiducial for calibrating the wavelength. The entire manifold consists of three lines of 21 channels separated by 10.4 mm. In between the lines are three uniform bars that can be used to flat-field the instrument.

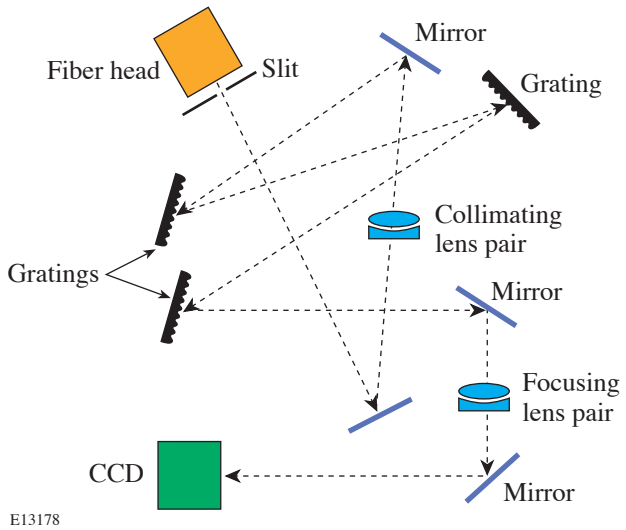

Figure 101.49
The layout of the spectrometer. The light from the fiber bundles passes through a slit array and a pair of collimating lenses before reflecting off of four mirrors and three gratings. A second pair of lenses focuses the light onto a CCD (charge-coupled device).

The resolution of the spectrometer would be limited by the 0.4-mm width of the bar unless the field of view is further limited. Unlike the adjustable slit commonly employed in spectrometers, the resolution of this instrument is selected from a fixed set of slit widths. The manifold sits behind a metallized fused-silica plate. The side of the plate facing the fiber manifold is coated with chromium. The backside is antireflection (AR) coated for UV light. The chromium was photolithographically etched with three sets of slits. Each set contained four slit openings: 10, 20, 40, and 60 μm. The plate sits on a computer-controlled linear stage that allows the selection of a single slit opening for all channels. The diffusing bars provide a uniform light source for illuminating the slit. The bars are at least six times larger than the slit width. By recording the slit opening for each shot, the response of the instrument can be photometrically calibrated.

Table 101.V gives the position and properties of each optical element in the path between the fiber manifold and the CCD (charge-coupled-device) detector. After passing through the slit, the light reflects off of a flat dielectric mirror. Four mirrors are used in the instrument to create a folded optical path. The folded path enables us to compress the instrument, with a total optical path length of greater than 5 m, onto a breadboard 1.2 m on an edge.

The optical system has a total demagnification factor of 0.87; therefore the slits at the input of the system appear smaller at the detector plane. The imaging is done with refractive optics.[9] Four lenses are arranged in two pairs: a collimating pair and a focusing pair. The focus can be adjusted by means of a micrometer that controls the separation of each pair of lenses. Many spectrometers use reflective optics to image the light through the instruments to avoid chromatic aberrations associated with the refractive elements; however, this instrument has a limited spectral range of 0.6 nm centered about 351 nm. Over this spectral range, spectral dispersion in the fused silica can be ignored. The index of refraction changes by less than one part in 10^5 over this wavelength range. For the optical system described here, the point-spread function at the CCD detector, due to chromatic aberration, was calculated at three wavelengths (350.7 nm, 351.0 nm, and 351.3 nm) and found to be 11 μm, 6 μm, and 12 μm, respectively, on axis. This means the resolution changes across the spectral range from 1.8 pm to 1.4 pm to 1.9 pm. The advantage of using refractive optics is that the imaging can be done on axis, which allows a wider field of view (FOV) than off-axis imaging. The large FOV is needed because the spatial extent of the fiber manifold is 21×25 mm^2. The effective width of the 21-mm dimension

expands to approximately 29 mm when wavelength dispersion of the full bandwidth is taken into account.

The spectral resolution of the system is achieved by using three 110×110-mm^2, 3600-line/mm holographic gratings. At a wavelength of 351 nm, the first-order diffraction efficiency is 38.8%. Based on a simulation of the spectrometer in OSLO,[10] a combination of the three gratings produces a total dispersion at the CCD detector in wavelength units per spatial distance of 9.1×10^{-2} pm/μm.

The CCD detector is a scientific-grade, 2048×2048 back-illuminated, thinned array.[11] The pixel pitch is 13.5 μm.[12] To increase the sensitivity and eliminate any interference effects, the array has no protective window; therefore, the CCD is mounted in vacuum to protect the chip from degradation. Light enters the vacuum chamber through a window mounted at 25° to the optic axis so that any back-reflections from the CCD surface are removed from the FOV of the detector. The CCD is cooled to –30°C to reduce dark noise. The smallest slit size should image to approximately 8.7 μm at the detector plane,

Table 101.V: Specification of the optical system.

Optical Element	Position	Size (diameter for circular edge for square)	Specifications	Transmission
Slit	0.1 mm		10, 20, 40, 60 μm Cr, AR	
Mirror	801.1 mm	150 mm on edge	HR 351 23° surface roughness 2.5 nm	0.995
Plano-concave collimation lens	1001.1 mm	192-mm diam × 30 mm thick	Radius 1 = ∞ Radius 2 = 368 mm	0.98
Convex-convex collimation lens	1105.2 mm	192-mm diam × 40 mm thick	Radius 1 = 524 mm Radius 2 = 473 mm	0.98
Mirror	1575.2 mm	150 mm on edge	HR 351 27° surface roughness 2.5 nm	0.995
Diffraction grating	2255.2 mm	110 mm	3600 gr/mm gold @ 45.5°	0.388
Diffraction grating	3015.2 mm	110 mm	3600 gr/mm gold @ 45.5°	0.388
Diffraction grating	3795.2 mm	110 mm	3600 gr/mm gold @ 45.5°	0.388
Mirror	4625.2 mm	150 mm on edge	HR 351 37° surface roughness 2.5 nm	0.995
Convex-convex focusing lens	4715.2 mm	192-mm diam × 40 mm thick	Radius 1 = 401 mm Radius 2 = 549 mm	0.98
Concave-plano focusing lens	4830.4 mm	192-mm diam × 30 mm thick	Radius 1 = 357 mm Radius 2 = ∞	0.98
Mirror	5050.4 mm	150 mm on edge	HR 351 45° surface roughness 2.5 nm	0.995
Vacuum window	5666.4 mm	50.8-mm diam × 5 mm thick	25° relative to normal incidence	0.992
CCD camera	5709.4 mm			0.17 (Q.E.)

which is less than the pixel pitch. Ideally, the image of a slit can illuminate just one pixel; however, the slit width must be convolved with the point-spread function listed above to determine the instrument resolution.

Instrument Performance

The multichannel spectrometer is now operational on the OMEGA laser system, and the instrument performance can be compared with the design specifications. Figure 101.50 shows the image of an acquired laser shot. The first operational issue is calibrating the wavelength. The middle channel of the middle column can be illuminated with the light from a neon pencil lamp.[13] This channel is on the optical axis and has very small optical aberrations due to imperfections in the imaging system. In this configuration, four Ne I lines are visible.[14] A least-squares fit to those wavelengths yields an absolute wavelength calibration for the middle column and a relative calibration for the two outside columns.[15] The experimentally measured dispersion was 8.6×10^{-2} pm/μm, giving 1.16 pm/pixel. This is 6% lower than the modeled value listed above and indicates a slight offset in the position of lenses, which decreases the magnification. When the neon lamp illuminates the outside columns, not all of the lines are visible. To determine the absolute calibration of the outside columns, the OMEGA laser is fired without the SSD bandwidth turned on. Under these conditions, all channels have the same narrow line spectrum. Adjusting the offset of the outside columns to match the center column gives an absolute wavelength calibration for all channels. The validity of the absolute wavelength calibration is tied to the precision to which the plate with the slit arrays can be reproducibility positioned. Since the illumination source is uniform, variations in the slit position translate to apparent shifts in the absolute wavelengths. The motorized, linear-translation stage can be reset to the same position to within 20 μm, which implies that the wavelength calibration is accurate to approximately 2 pm after the slits are changed. To obtain the highest accuracy, the wavelength should be recalibrated every time the slit width is adjusted.

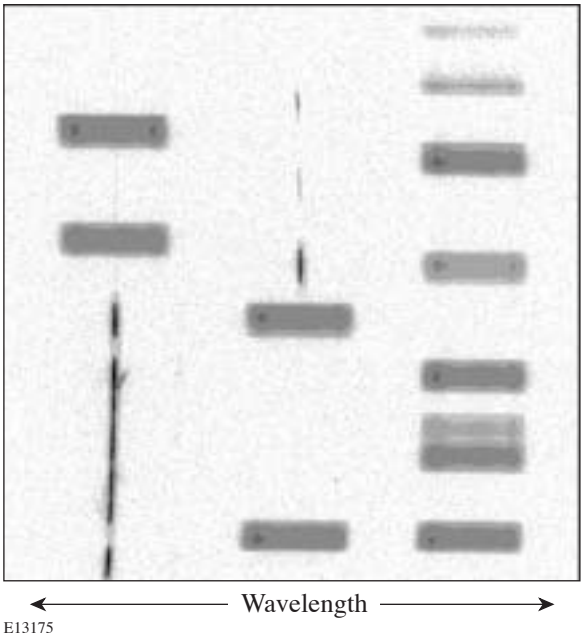

Figure 101.50
A UV-spectrometer CCD image from shot 37038 showing 23 of 60 beams with and without SSD. The density is logarithmic. The SSD beams, represented by large rectangular spectra, have approximately the same energy and 80 times the bandwidth of the narrow-linewidth beams.

Aberrations within the imaging system of the spectrometer have been reduced to bring all channels within specifications. Channels near the optical axis exceed the performance requirements of the system. With SSD turned off, these channels will record a spectral full width at half maximum (FWHM) of 2.5 pm for laser energies that vary by a factor of 36 for 1-ns square pulses. The laser that seeds all sixty beams has a nearly transform-limited bandwidth, which has a measured UV-equivalent linewidth of less than 0.3 pm (the calculated linewidth of this laser is 4×10^{-4} pm). The independence of the spectral FWHM on laser energy implies that there is no *B*-integral broadening of the laser linewidth and the inputs to the spectrometer have the same spectral width as the seed laser; therefore, the measured linewidth is the intrinsic response of the instrument. For subnanosecond pulses, this is not the case. Figure 101.51 illustrates that the instrument performance is sufficient to observe *B*-integral broadening when it occurs. Two normalized spectra are shown: the wider spectrum is of a 100-ps pulse, the second spectrum is from a low-energy, 2-ns laser shot, which represents the instrument-limited response. As the position of the channels moves away from the optic axis, line-spread function increases. At the edges of the FOV of the CCD, the minimum FWHM is 6 pm. This resolution is sufficient for tuning the frequency-conversion crystals.

In addition to broadening, the optical system introduces curvature to the wavelength field. The straight slits in the object plane map to curves in the image plane, which deviate quadratically with distance from the center of the FOV. The maximum deviation at 14 mm from the optic axis is 300 μm. With additional fine-tuning of the alignment, it might be possible to remove these aberrations. It was decided, however, that since the aberrations were sufficiently well characterized,

it was easier to remove them using image-processing algorithms than to realign the spectrometer.

The optical transmission through the spectrometer was measured by removing the fibers from the input to the spectrometer and recording the amount of light emerging from the fiber with a calibrated energy meter. The fiber was again connected to the spectrometer, and the total CCD analog-to-digital units (CCD_ADU) were recorded. The CCD_ADU total was converted to joules using the manufacturer's supplied quantum efficiency of the camera. A typical transmission value was $1.6 \times 10^{-5} \pm 0.5 \times 10^{-5}$, with most of the variation associated with the alignment of the fibers in the external fiber bundle with a similar internal fiber bundle that connects to the manifold. The transmission loses are dominated by the 10-μm slit aperture on the 400-μm source (transmission = 2.5%) and the mismatch between the *f*/2.5 numerical aperture of the fibers coupling into the *f*/10 of the collimating lens, which gives an effective transmission of 6%. The product of these transmissibilities is multiplied by the product of all the transmission factors listed in Table 101.V to estimate the transmission through the spectrometer as 2.1×10^{-5}. The light from a single channel that is transmitted to the CCD is very uniform in the spatial direction because of the homogenizer in the fiber manifold. There are 570 columns in each of the 63 spectra, and each of those 570 is the average of approximately 100 spatial pixels, all of which are nearly identical. The signal-to-noise ratio (SNR) at each point (the average over the column) is just the average divided by the standard deviation times the square root of the number of points averaged.[16] In a single image there are 35,910 individual measurements of the SNR. Figure 101.52 is a plot of the SNR as a function of the average signal in CCD_ADU. This data was taken with SSD on and a 20-μm slit. The peak SNR is 100 at an average signal of 300 ADU. Typical SSD spectra can be characterized as a flattop at 80% of the peak and a peak-to-valley modulation of 40% of the peak value. Over this range, most of the spectra have an SNR of 70 to 100. The SNR drops to 1 when the average pixel value is 1.4 ADU, so the dynamic range of this instrument is about 200. The solid line in Fig. 101.52 represents the SNR if the data followed Poisson statistics. At low signal counts, the SNR falls below this line due to the read noise of the CCD.

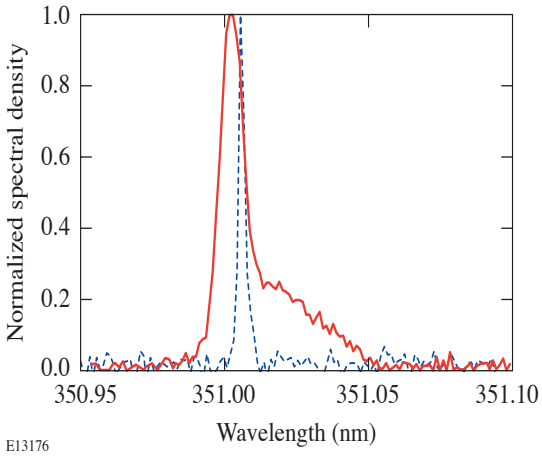

Figure 101.51
The dashed curve represents a 9-J, 2-ns pulse on beam 61 (shot 35921). Under these conditions, the spectral width is expected to be transform limited. This curve represents the instrument response to a single frequency. The solid curve shows the broadening and spectral shift associated with a 50-J, 100-ps pulse (shot 36701).

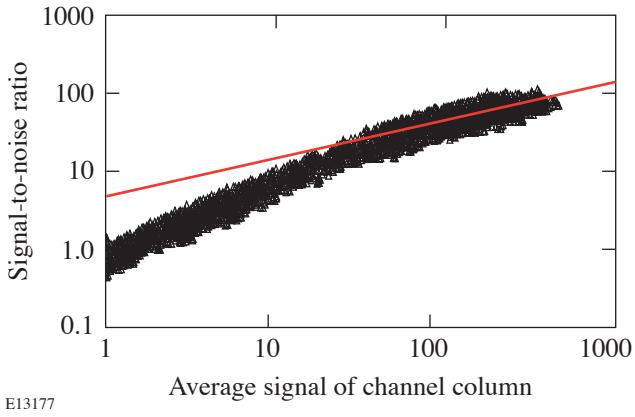

Figure 101.52
The SNR ratio for each point in the image was calculated by dividing the average CCD_ADU count in a 1-pixel-wide segment of a 100-pixel-high channel by the standard deviation of that same set of pixels times the square root of the number of pixels. These values are plotted as triangles. The solid line is the expected SNR of data following Poisson statistics.

A separate instrument records the energy of the UV light before it enters the fiber. The total CCD_ADU for each channel has been correlated with this number, and the ratio is constant to within 8.5%. This is the precision to which the photometric calibration can be trusted. The precision is limited by crosstalk between the channels. Decreasing the channel width will decrease the crosstalk at the expense of the SNR.

Preliminary measurements with this instrument have verified that SSD spectra vary from beam to beam. A protocol is being developed to remove this variation by adjusting the angular tuning of the frequency-tripling KDP crystals. In

addition, the instrument is being used to study the spectral broadening that occurs in the OMEGA laser system when the pulse duration is less than 100 ps. The spectral shifts are closely tied to the rise and fall times of the pulse.

This spectrometer can prove to be a useful diagnostic instrument on large multibeam ICF laser systems such as LLE's OMEGA laser, the National Ignition Facility at Lawrence Livermore National Laboratory,[17] and the Le MegaJoule Laser in France,[18] where the bandwidth is deliberately added to the laser spectrum for spatial smoothing or for suppression of nonlinear processes such as stimulated Brillion scattering. The spectrometer's unique design employing refractive optics makes it suitable for imaging spectroscopic applications that deal with relatively narrow spectroscopic ranges such as laser line broadening or for resolving a specific atomic transition.

ACKNOWLEDGMENT

This work was supported by the U.S. Department of Energy Office of Inertial Confinement Fusion under Cooperative Agreement No. DE-FC52-92SF19460, the University of Rochester, and the New York State Energy Research and Development Authority. The support of DOE does not constitute an endorsement by DOE of the views expressed in this article.

REFERENCES

1. T. R. Boehly, D. L. Brown, R. S. Craxton, R. L. Keck, J. P. Knauer, J. H. Kelly, T. J. Kessler, S. A. Kumpan, S. J. Loucks, S. A. Letzring, F. J. Marshall, R. L. McCrory, S. F. B. Morse, W. Seka, J. M. Soures, and C. P. Verdon, Opt. Commun. **133**, 495 (1997).
2. F. J. Marshall, J. A. Delettrez, R. Epstein, R. Forties, R. L. Keck, J. H. Kelly, P. W. McKenty, S. P. Regan, and L. J. Waxer, Phys. Plasmas **11**, 251 (2004).
3. M. D. Skeldon, Rev. Sci. Instrum. **71**, 3559 (2000).
4. S. Skupsky, R. W. Short, T. Kessler, R. S. Craxton, S. Letzring, and J. M. Soures, J. Appl. Phys. **66**, 3456 (1989).
5. R. S. Craxton, Opt. Commun. **34**, 474 (1980).
6. A. Babushkin, R. S. Craxton, S. Oskoui, M. J. Guardalben, R. L. Keck, and W. Seka, Opt. Lett. **23**, 927 (1998).
7. Y. R. Shen, *The Principles of Nonlinear Optics* (Wiley, New York, 1984), pp. 324–329.
8. Polymicro Technologies, Polymicro FVP 300 330 370, 2003, http://www.polymicro.com (4 August 2004).
9. J. P. Knauer, E. Pasch, G. Kühner, and the W7-AS Team, Rev. Sci. Instrum. **74**, 1679 (2003).
10. *OSLO User's Guide*, Version 5 (Sinclair Optics, Pittsford, NY 14534, 1996) (http://www.sinopt.com).
11. Spectral Instruments, Tucson, AZ 85745 (see http://www.specinst.com/files/datasheets/4204-.pdf).
12. e2v technologies, Elmsford, NY 10523-1482 (see http://e2vtechnologies.com).
13. T. Han *et al*., Rev. Sci. Instrum. **74**, 2973 (2003).
14. NIST Atomic Spectra Database, NIST Standard Reference Database #78, 1999, http://physics.nist.gov/cgi-bin/AtData/main_asd (4 August 2004).
15. M. Born and E. Wolf, *Principles of Optics: Electromagnetic Theory of Propagation, Interference and Diffraction of Light*, 6th ed. (Pergamon Press, Oxford, 1980), p. 436.
16. W. R. Donaldson, R. Boni, R. L. Keck, and P. A. Jaanimagi, Rev. Sci. Instrum. **73**, 2606 (2002).
17. E. I. Moses *et al*., in *Optical Engineering at the Lawrence Livermore National Laboratory*, edited by T. T. Saito and M. A. Lane (SPIE, Bellingham, WA, 2003), Vol. 5001, pp. 1–15.
18. G. Thiell *et al*., Fusion Sci. Technol. **43**, 478 (2003).

Quantum Efficiency and Noise-Equivalent Power of Nanostructured, NbN, Single-Photon Detectors in the Wavelength Range from Visible to Infrared

Introduction

Single-photon-detection schemes based on sensitive and ultrafast optical quantum detectors gain their dominance in various single-photonics applications. The development of superconducting single-photon detectors (SSPD's), based on ultrathin, submicron-width NbN structures has already been reported.[1–4] SSPD's are ultrafast and sensitive for ultraviolet, visible, and infrared (IR) photons. They exhibit very low dark counts and require no active or passive quenching. As recently demonstrated, SSPD's exhibit real-time counting rates of above 2 GHz and a <20-ps timing jitter.[5,6] The SSPD operation principle has been introduced within a phenomenological hot-electron photoresponse model.[1,7] In this article, the results of our research on the latest generation of SSPD's are presented, including their quantum efficiency (QE) and the noise-equivalent power (NEP) in the wavelength range between 0.5 and 5.6 μm, and their dependencies on an operating temperature in the 2.0- to 4.2-K range. The main emphasis is on the very low-temperature (2.0-K) performance of our SSPD's.

Device Fabrication

NbN superconducting films used for the fabrication of SSPD's had a thickness of 4.0 nm and were deposited on sapphire substrates by dc reactive magnetron sputtering in an Ar and N_2 gas mixture. The films were characterized by a surface resistance R_S = 500 Ω/square, a critical temperature T_c = 10 to 11 K, a superconducting transition width $\Delta T_c \sim$ 0.3 K, and a critical current density $j_c = 6$ to 7×10^6 A/cm^2 at 4.2 K. During our deposition process, the sapphire substrate with *c*-cut crystalline orientation was heated up to 900°C, leading to an epitaxial growth of the NbN thin film. Our detectors had a meander-type geometry that covered a 10 × 10-μm^2 area and had a filling factor (the ratio of the area occupied by the superconducting meander to the device nominal area) of up to 0.5. The width of the superconducting stripe was typically 100 to 120 nm, but it could be as low as 80 nm. The devices were fabricated using the process based on direct electron-beam lithography and reactive ion etching.

A detailed description of our technological operations was presented in a recent publication.[8] During the electron-beam lithography process, the areas under which the superconductor was removed were exposed in the resist. The minimal width of the superconducting stripe did not depend directly on the electron-beam diameter; rather, it was largely determined by the electron scattering in the photoresist. The resist PMMA 950 K was used and later removed from the superconductor using the reactive ion-etching process. The choice of the 80-nm resist thickness ensured a reliable protection of the superconducting film. Significant reductions of resist thickness allowed us to fabricate meanders with a filling factor of up to 0.5 and superconducting stripes as narrow as 80 nm (Fig. 101.53).

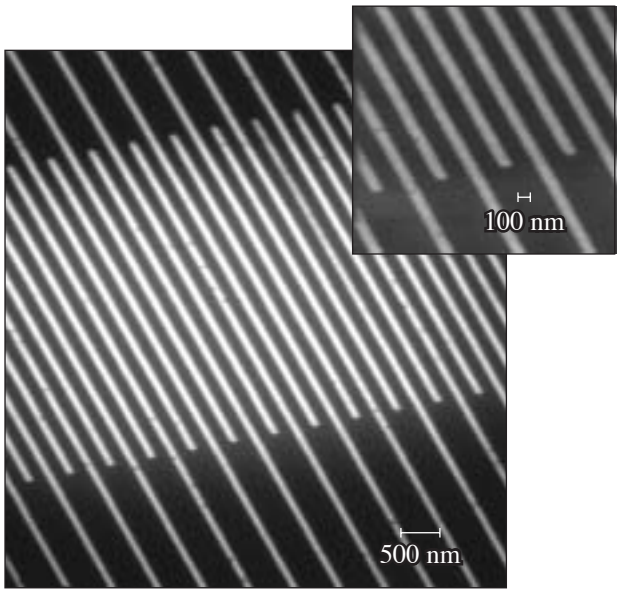

Z2704

Figure 101.53
SEM (scanning electron microscope) image of an SSPD (NbN is black). The inset shows the meander structure in detail.

To test the impact of the NbN film processing on its superconducting properties, the temperature dependence of the resistance of the patterned SSPD was measured and compared to the original NbN film. The T_c and ΔT_c of the reactive ion-etched devices and the original films were practically the same within 0.1-K accuracy. This latter fact proves the optimal character of our technological process since no negative impact on the NbN SSPD was observed. In addition, it confirmed the very high quality of our initial, ultrathin NbN films.

Experimental Setup

A schematic diagram of our experimental setup is shown in Fig. 101.54. The SSPD was wire-bonded to a coplanar transmission line and then connected to a very stable, constant-voltage bias source and the output circuitry through a coaxial cryogenic bias-tee. The constant-voltage operation regime ensured a rapid return to the superconducting state after the photon detection of the SSPD and prevented self-heating of the device. The entire assembly was placed on a cold plate, inside an optical cryostat. The SSPD voltage response was amplified by a room-temperature, 40-dB-gain, 1- to 2-GHz-bandwidth amplifier and then fed to a pulse counter for statistical analysis.

Light sources consisted of a set of continuous-wave (cw) laser diodes covering the range from 0.56 μm to 1.55 μm and pulsed laser diodes delivering 40- to 60-ps-wide pulses at a repetition rate of 1 to 103 kHz at 637-nm, 845-nm, and 1554-nm wavelengths. A grating monochromator for generating IR (1- to 5.6-μm-wavelength) radiation was also used.

Photons from the lasers were delivered to the detector either by propagating in free space or by an optical fiber. In each case, the input radiation was focused and attenuated down to the picowatt power level or below. Sapphire input windows were used for measurements in the 0.6- to 3.0-μm-wavelength range and silicon windows for measurements in the 1.2- to 5.6-μm-wavelength range. Cold sapphire or silicon filters were placed inside the cryostat to cut parasitic room-temperature background radiation.

Experimental Results and Discussion

QE is defined as the ratio of the detection events registered by the counter N_{reg} to the number of incident photons N_{inc} for a given time interval per the device area:

$$QE = N_{\text{reg}} / N_{\text{inc}} . \quad (1)$$

In cw measurements, the N_{inc} value was determined from the power incident on the device's nominal active area of 100 μm^2 measured by a power meter. The power of our laser sources was always measured separately by calibrated optical attenuators. In experiments with pulsed sources, experimental QE was simply the probability of photon counting, measured at the one-photon-per-pulse level, incident upon the SSPD nominal area and expressed in percent.

Figure 101.55 shows that our most recent advances in SSPD fabrication technology led to the greatly improved stripe uniformity and resulted in significant QE enhancement.

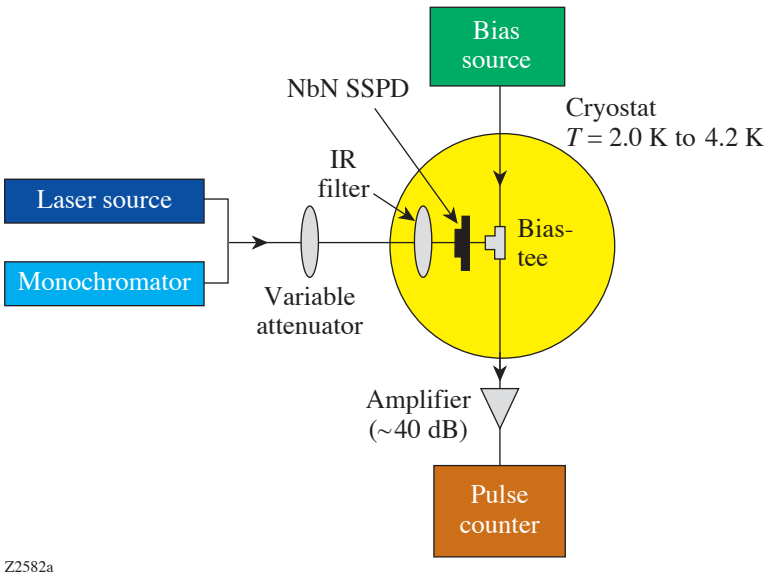

Figure 101.54
Experimental setup.

Figure 101.55 presents the QE's dependence on normalized bias current I_b/I_c at two different operating temperatures. At 4.2 K, QE for visible-light photons reaches an ~30% value. One can also note in Fig. 101.55 an evidence of QE saturation at the 0.56-μm wavelength at 4.2 K. The saturation-like behavior is, however, more obvious looking at the 2-K, 0.56-μm data. Furthermore, for visible light, the decrease in operating temperature below 4.2 K led to no improvement in QE; therefore, the observed saturation means that in the visible range, our SSPD detects every photon absorbed by the superconducting NbN film.

From an application point of view, the telecommunication 1.3-μm and 1.55-μm wavelengths are the most interesting. The QE at these wavelengths at 2 K is also presented in Fig. 101.55. One can see that at 1.3 μm, the QE reaches 30% saturation value, while at 1.55 μm, the maximum QE is 17%. At 4.2 K, the QE for IR light is quite far from saturation. For example, the maximum QE at 1.55 μm at 4.2 K is only 3.7% and only for I_b approaching I_c (Fig. 101.55).

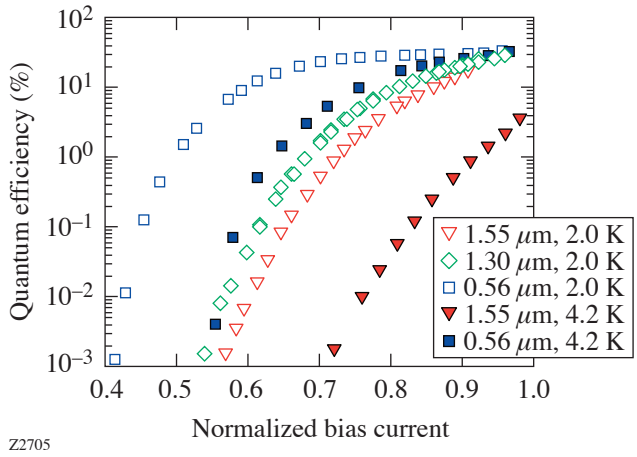

Figure 101.55
Quantum efficiency measured at different wavelengths at 4.2-K and 2.0-K operating temperatures.

Figure 101.56 presents the dark-count rate R versus I_b/I_c. R is determined as a number of spurious counts per second when the SSPD input is completely blocked by a cold metal shield inside the cryostat. Without the shield or cold filter, e.g., when the device was directly connected to the fiber, the SSPD was exposed to 300-K background radiation, which manifested itself as extrinsic dark counts. The $R(I_b)$ dependence

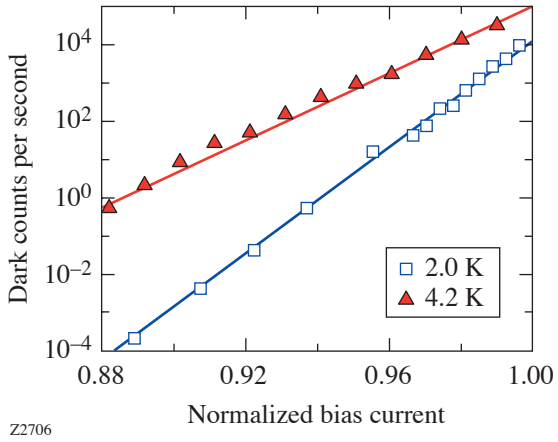

Figure 101.56
SSPD dark counts as a function of the normalized bias current measured at 4.2 K and 2.0 K.

demonstrates the activation law in the whole biasing range used in our experiments $(0.87 < I_b/I_c < 0.99)$:

$$R = a \times \exp\left(b\frac{I_b}{I_c}\right), \tag{2}$$

where a and b are constants. The activation-type behavior of $R(I_b)$ extends up to over seven orders of magnitude. The minimum measured R was as low as 2×10^{-4} s^{-1} and was limited by the duration of the experiment, i.e., accumulating several dark counts took about 8 h.

An optimal operation regime of the SSPD is a trade-off between QE and R. The maximum value of QE corresponds to rather high (~1000 s^{-1} or above) R. Quantitatively this interplay between QE and R can be presented in terms of the noise-equivalent power (NEP), which can be defined for quantum detectors as

$$\text{NEP} = \frac{h\nu}{\text{QE}}\sqrt{2R}, \tag{3}$$

where $h\nu$ is photon energy. The open symbols in Fig. 101.57 show the results of the NEP calculation using Eq. (3) and experimentally measured QE (Fig. 101.55) at 1.3 μm and 1.55 μm and R (Fig. 101.56) values. Only the lowest points at 2.0 K (for $I_b/I_c < 0.88$) were calculated using extrapolated values of R.

As one can see, at 2.0 K for photons at the telecommunication wavelengths, our SSPD's exhibit QE > 10% and simultaneously reach an NEP level as low as 5×10^{-21} W/Hz$^{1/2}$. To our knowledge, this is the best performance for any currently available single-photon detector.

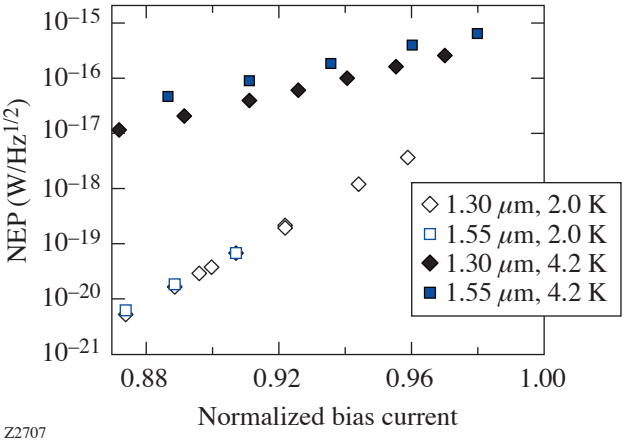

Figure 101.57
The SSPD NEP at 4.2 K (closed symbols) and 2.0 K (open symbols), calculated for 1.30 μm (diamonds) and 1.55 μm (squares) using the experimental R and QE values from Figs. 101.55 and 101.56, respectively.

The spectral characteristics of the NbN SSPD's using radiation from the monochromator (see Fig. 101.54) have been investigated in the IR 0.9- to 5.6-μm-wavelength range at different operating temperatures (2.9 to 4.3 K) and bias currents. In our best devices, single-photon counting was observed up to 5.6-μm wavelength. Figure 101.58 shows that the spectral sensitivity has exponential character and strongly depends on I_b. The highest detection probabilities are measured for I_b values very close to I_c. The decrease in operating temperature for a given I_b/I_c improves QE and also extends the SSPD's single-photon–counting capabilities farther into the IR wavelength range.

Conclusions

The performance of our latest-generation SSPD's tested at 2.0 K has been presented. The very low-temperature operation extends the single-photon–counting capabilities of our detectors to 5.6-μm IR wavelength. Simultaneously, at 2 K, the QE of our devices reached ~30% saturation, which corresponds to the photon absorption in a 4-nm-thick NbN film. Finally, the 2-K temperature environment resulted in a drastic (over two orders of magnitude as compared to the 4.2-K operation) decrease in the detector dark counts. The QE increase and the R decrease led to NEP values at 2 K as low as 5×10^{-21} W/Hz$^{1/2}$ at the IR wavelength.

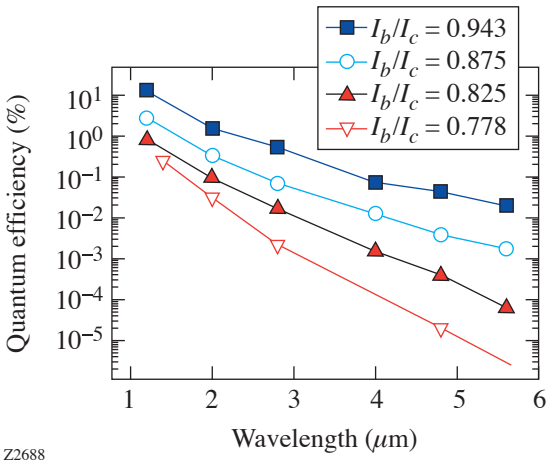

Figure 101.58
QE spectral dependencies, measured for a NbN SSPD at 3 K at different bias currents (I_c = 29.7 at 3 K). Solid lines are guides for the eye.

The demonstrated SSPD performance at 2 K shows that in the IR range, the SSPD's significantly outperform the best semiconductor devices and photomultiplier tubes. The SSPD's have already found practical applications for the debugging of very large-scale, integrated Si complementary metal-oxide-semiconductor circuits,[9] and they are of great interest in other areas, such as single-molecule fluorescence and high-resolution astronomy.

For applications in the areas of fiber-based and fiberless (free-space) optical quantum communications, quantum metrology, quantum key distribution, and linear optical quantum computation, it is interesting to compare the NbN SSPD with its superconducting counterparts. The other superconducting radiation detectors,[10] such as superconducting tunnel junctions (STJ)[11] and superconducting transition edge sensors (STES),[12] exhibit a very slow (kHz-range) photoresponse speed, and their jitter in the photon-counting mode is difficult to determine. The fundamental reason for the slow speed of these detectors is that they are bolometric (thermometer-like) devices based on superconductors with very low (below 1 K) T_c, which is dictated by the desire to reach the lowest-possible intrinsic noise levels and NEP; therefore, STJ's and STES's are not optimal for very high-speed quantum communication. The

STES's, however, are photon-number–resolving devices with very high (>80%) QE values, which makes them very attractive for quantum metrology and optical quantum computations.[13]

ACKNOWLEDGMENT

This work was funded by RFBR grant 03-02-17697 (Moscow), CRDF grant RE2-2529-MO-03 (Moscow and Rochester), and US AFOSR grant FA9550-04-1-0123 (Rochester). Additional support was provided by a MIT Lincoln Laboratory grant.

REFERENCES

1. G. N. Gol'tsman, O. Okunev, G. Chulkova, A. Lipatov, A. Semenov, K. Smirnov, B. Voronov, A. Dzardanov, C. Williams, and R. Sobolewski, Appl. Phys. Lett. **79**, 705 (2001).

2. A. Verevkin, J. Zhang, R. Sobolewski, A. Lipatov, O. Okunev, G. Chulkova, A. Korneev, K. Smirnov, G. N. Gol'tsman, and A. Semenov, Appl. Phys. Lett. **80**, 4687 (2002).

3. R. Sobolewski, A. Verevkin, G. N. Gol'tsman, A. Lipatov, and K. Wilsher, IEEE Trans. Appl. Supercond. **13**, 1151 (2003).

4. J. Zhang, W. Slysz, A. Verevkin, O. Okunev, G. Chulkova, A. Korneev, A. Lipatov, G. N. Gol'tsman, and R. Sobolewski, IEEE Trans. Appl. Supercond. **13**, 180 (2003).

5. A. Verevkin, A. Pearlman, W. Slysz, J. Zhang, M. Currie, A. Korneev, G. Chulkova, O. Okunev, P. Kouminov, K. Smirnov, B. Voronov, G. N. Gol'tsman, and R. Sobolewski, J. Mod. Opt. **51**, 1447 (2004).

6. A. Korneev, P. Kouminov, V. Matvienko, G. Chulkova, K. Smirnov, B. Voronov, G. N. Gol'tsman, M. Currie, W. Lo, K. Wilsher, J. Zhang, W. Slysz, A. Pearlman, A. Verevkin, and R. Sobolewski, Appl. Phys. Lett. **84**, 5338 (2004).

7. A. D. Semenov, G. N. Gol'tsman, and A. A. Korneev, Physica C **351**, 349 (2001).

8. G. N. Gol'tsman, K. Smirnov, P. Kouminov, B. Voronov, N. Kaurova, V. Drakinsky, J. Zhang, A. Verevkin, and R. Sobolewski, IEEE Trans. Appl. Supercond. **13**, 192 (2003).

9. J. Zhang, N. Boiadjieva, G. Chulkova, H. Deslandes, G. N. Gol'tsman, A. Korneev, P. Kouminov, M. Leibowitz, W. Lo, R. Malinsky, O. Okunev, A. Pearlman, W. SBysz, K. Smirnov, C. Tsao, A. Verevkin, B. Voronov, K. Wilsher, and R. Sobolewski, Electron. Lett. **39**, 1086 (2003).

10. A. D. Semenov, G. N. Gol'tsman, and R. Sobolewski, Supercond. Sci. Technol. **15**, R1 (2002).

11. J. H. J. de Bruijne *et al.*, Opt. Eng. **41**, 1158 (2002).

12. B. Cabrera *et al.*, Appl. Phys. Lett. **73**, 735 (1998).

13. A. J. Miller *et al.*, Appl. Phys. Lett. **83**, 791 (2003).

Measurement of Preheat due to Fast Electrons in Laser Implosions of Cryogenic Deuterium Targets

Introduction

The fraction of the incident laser energy that is deposited by energetic electrons as preheat in the cryogenic fuel of imploded spherical targets has been measured for the first time. Preheat due to fast electrons has long been identified as a contributing factor in performance degradation in laser-imploded fusion targets.[1] Fast-electron preheat reduces the fuel compressibility, thereby reducing the ignition margin. Theoretical designs for direct-drive fusion experiments on the National Ignition Facility (NIF)[2] use shock preheat to control the isentrope of the ablation surface and the fuel by varying the incident laser pulse shape. However, additional preheat due to fast electrons can be detrimental to the target gain. Detailed simulations have shown that the fraction of the laser energy dumped as total preheat in the cryogenic DT fuel has to be well below 0.1% for the preheat problem to have a negligible impact on target performance.[3] This fraction is the key parameter in assessing the severity of preheat and is the quantity determined in this work, based on the measured hard-x-ray (HXR) continuum on the OMEGA[4] laser system. In an earlier work,[5] the source of the fast electrons has been identified as the two-plasmon-decay instability, but the determination of preheat level is independent of this identification. Measuring the fast-electron preheat is particularly important because the calculation of the fast-electron source is difficult and is not included in most hydrodynamic target simulations. The present measurements of preheat in cryogenic-fuel targets on the OMEGA laser system are relevant to future high-gain direct-drive implosions on the NIF since the laser irradiation, $\sim 10^{15}$ W/cm^2, is similar to the design irradiance for the NIF direct-drive cryogenic targets.[2] Although the ablation density scale length (which affects the generation of fast electrons) is shorter than that of NIF targets, earlier experiments[5] on planar CH targets with scale lengths comparable to those on NIF-design targets have shown the preheat fraction to be about the same as in the present spherical experiments. Furthermore, using various combinations of phase plates and laser-beam configurations on planar targets, the experiments showed[5] that the total HXR signal scaled primarily with irradiance, not with scale length or plasma temperature. Thus, the present OMEGA preheat results can be projected to future direct-drive experiments on the NIF.

To calibrate the HXR detectors, a CH-coated molybdenum solid sphere was irradiated, and the HXR continuum and absolutely calibrated Mo-Kα line were measured simultaneously. Using the relationship between these two measured quantities (through the preheat) provided a calibration of the HXR detectors. Using this calibration, we determine, first, the preheat in thick imploding CH shells filled with deuterium gas and then the preheat in cryogenic-deuterium targets. In all these cases (including the cryogenic targets) the laser interaction and, thus, the production of fast electrons occur within the outer CH layer.

The preheat level is determined directly from the measured spectrum of the hard x rays. The only required parameters are the total hard-x-ray energy and the fast-electron temperature, both obtained from the measured spectrum. This determination bypasses the need to know the trajectories or dynamics of the fast electrons: for each fast electron interacting with the target, there is a direct ratio between the cross section for slowing down collisions (which constitute preheat) and the cross section to emit continuum or Kα radiation. Thus, the observed radiation (of either kind) leads directly to the preheat level. These assertions are strongly supported by the transport simulation results shown below.

Preheat in Thick CH Shells

The HXR signal for a series of deuterium-gas–filled, thick CH shells as a function of laser irradiance has been published,[5] but without a determination of the preheat level. The CH shells were 27 μm thick, 900 to 1100 μm in diameter, and filled with 20 atm of deuterium gas. They were irradiated with 60 beams at 351-nm wavelength, of 1-ns square pulse, and irradiance in the range of 6 to 9 $\times$ 10^{14} W/cm^2. The beam parameters specified here were also used for the molybdenum and the cryogenic targets described below. In the case of thick CH shells, the fast electrons interact mostly with cold CH. The

slowing down and radiation by electrons passing through the deuterium fill gas is negligible. We simulate the transport of fast electrons and emission of bremsstrahlung radiation within the CH by a multigroup transport code[6] that assumes the initial electron energy distribution function to be Maxwellian (this assumption is based on 2-D simulations of the two-plasmon-decay instability[7]). The number of fast electrons is immaterial for the calculation of the ratio of preheat to x-ray emission. The collisions causing the slowing down are calculated from the stopping-power and range tables of the National Institute of Standards and Technology (NIST),[8] which are based on Bethe's dE/dx formula[9] and the density correction of Sternheimer.[10] The energy loss rate due to bremsstrahlung is given by the Heitler relativistic formula.[11]

Figure 101.59 shows the results of these calculations. The curve marked "transport" is the result of transporting the multigroup distribution of initial temperature T through the total CH shell thickness. The curve marked "dE/dx ratio" is the ratio of the energy-loss rates for slowing-down collisions and for bremsstrahlung emission of electrons of a single energy E. The major factor determining the shape of these curves (and their differences) is the fact that the slowing-down rate is approximately proportional to $1/E$. The two curves differ in two respects: the transport curve is the result of integration over the thickness of the target and it refers to an initially Maxwellian energy distribution, whereas the dE/dx curve refers to the local rates and to a single energy. At the limit of very high temperature, where transport is unimportant, the second factor dominates: since in a Maxwellian energy spectrum there are more electrons below the energy $E = T$ (where the slowing-down rate is higher) than above it, the preheat for the transport curve is higher than for the dE/dx-ratio curve. For lower temperatures the same effect dominates only in a thin layer below the target surface; farther in, more and more of the slow electrons lose all their energy and the distribution is left with only higher-energy electrons, for which the slowing-down rate is lower.

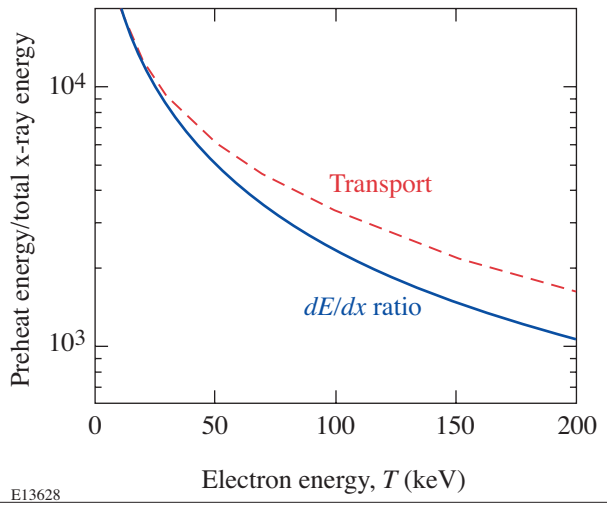

Figure 101.59
Calculated ratio of preheat energy to total hard-x-ray energy for CH shells. The curve marked "transport" is the result of multigroup fast-electron transport through the 27-μm-thick shell, for an initially Maxwellian distribution of temperature T. The curve marked "dE/dx ratio" is the ratio of the energy-loss rates for stopping-power collisions and for bremsstrahlung emission for electrons of a single energy E. The abscissa values for the two curves refer to fast-electron temperature (for the transport curve) and electron energy (for the dE/dx-ratio curve).

The purpose of comparing the two curves in Fig. 101.59 is to show that the role of scattering (which was neglected here) is relatively unimportant for the calculation of the ratio of preheat to x-ray emission. Thus, the dE/dx ratio can be viewed as the result of transport in the limit of a very thin shell for which scattering is negligible. The inclusion of scattering in the transport, by extending the electron paths, would increase both the preheat and the HXR energy by the same factor. Furthermore, varying the shell thickness leaves the ratio of preheat to total HXR energy virtually unchanged, which again supports the omission of scattering. An additional confirmation of this assertion is provided by the molybdenum results below. Thus, by relating the preheat to the observed HXR signal, we bypass all questions related to the fast-electron paths. The slowing down from the NIST tables pertains to cold material. This assumption is true for most of the CH shell throughout the duration of the laser pulse. Furthermore, using a slowing-down formula for ionized material yields only slightly different results (see below). Thus, using the NIST tables for the total CH shell is adequate. The transport curve in Fig. 101.59 is used to determine the preheat fraction for the imploding CH shells. The fast-electron temperature for each target shot was determined from the slope of the HXR spectrum;[5] for the narrow range of laser irradiance $I \sim 6$ to 9×10^{14} W/cm^2, the fast-electron temperature changes in the range of 60 to 80 keV. The temperature was determined[5] with a precision of ±15%, which translates to a precision of about ±10% in the preheat fraction in this temperature range.

To determine the preheat energy, the HXR energy must be measured absolutely. To that end, we irradiated a CH-coated molybdenum solid sphere where the preheat was measured simultaneously through the HXR continuum and the (absolutely calibrated) Mo-Kα line. Most of the HXR emission

(and all the Kα emission) comes from the molybdenum. Molybdenum was chosen to minimize the contribution of thermal x rays to the excitation of the Kα line. Previous experiments on planar targets[6] with Kα lines of energy around 5 keV showed that the contribution of radiation to the production of Kα lines was comparable to that of fast electrons (in all cases the laser interacts only with the CH coating). To differentiate between the two contributions, dual-element (V and Ti) targets were used, and the Kα lines were observed from both sides of the target. Since that solution is not available with spherical targets, we chose a much-higher-Z element. Only radiation above the Mo-K edge, at 20 keV, can contribute to the excitation of the Mo-Kα line. At that energy, the thermal x-ray spectrum is several orders of magnitude lower than at 5 keV. Figure 101.60 shows a film lineout of the Kα line of molybdenum from a CH-coated molybdenum sphere. The target consisted of a 1.07-mm-diam Mo sphere coated with 12 μm of CH and was irradiated at 7.7×10^{14} W/cm^2. As expected, the continuum intensity underlying the Kα line is too weak to measure This confirms the assertion that the Kα line is excited exclusively by fast electrons (neither can it be excited by the hard x rays, whose energy is found to be lower than that of the Kα line).

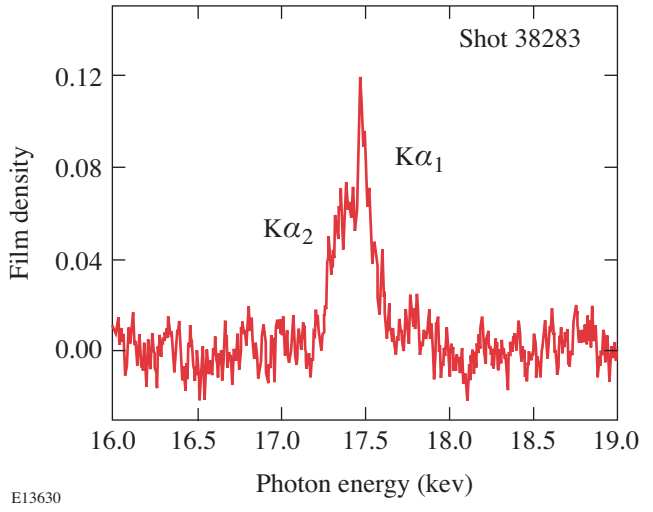

Figure 101.60
Measured Kα line of molybdenum from CH-coated molybdenum sphere.

The measured Kα line on film is converted to energy using the crystal and film calibrations. For the crystal used [polished and etched LiF (2,0,0)], our calibration[12] agrees well with the results of Toh *et al.*[13] and Gilfrich *et al.*[14] The published calibration for the Kodak direct-exposure film (DEF) was used[15] with the film-processing procedure closely followed. Above the Br K edge (at 13.475 keV) the film density is almost exactly linear with x-ray flux, which greatly simplifies the film conversion. The total energy emitted by the target in the Kα line per unit solid angle is given by $E_l L/R$, where E_l is the energy incident on the film per unit length along the line, R is the crystal integrated reflectivity at the Kα energy, and L is the distance from target to film along the spectral ray.

To relate the intensity of the Mo-Kα line to the fast-electron energy, we use the multigroup code for the transport of the fast electrons with the inclusion of the rate for excitation of the Kα line. The photoionization rate of K-shell electrons, which leads to Kα emission, is given by the semi-empirical cross section of Powell.[16] In addition, the code calculates the transport of the Kα line emission out of the target. The results, with and without the inclusion of the Kα opacity, are shown in Fig. 101.61(a). Using the curve marked "with opacity" and the measured Kα emission, the preheat can be determined. The HXR emission in molybdenum is calculated in the same way as for the CH targets, and the results are shown in Fig. 101.61(b). As in Fig. 101.59, the abscissa designates electron temperature for the transport curve and electron energy for the dE/dx-ratio curve.

We can gain additional confidence in the curves of Fig. 101.61(b), and, by implication, those of Fig. 101.59, by comparing them with the known efficiency ε of an x-ray tube with a molybdenum anode. The input power that accelerates the electrons in the tube is converted mainly to heating the anode (equivalent to preheat in our case), with a small fraction converted to x rays, mostly continuum. The power P of x-ray continuum emission is given by the empirical relation[17] $P = K(Z) \times Z \times I \times V^2$, where V and I are the accelerating voltage and the tube current, respectively, and K depends weakly on the atomic charge Z. Thus, the ratio of heating to radiation is $\varepsilon^{-1} = [Z \times V \times K(Z)]^{-1}$. For molybdenum, the empirical value[17] of K is ~0.85×10^{-6} keV^{-1}. Plotting ε^{-1} as a function of V results in the dotted curve for the Mo tube in Fig. 101.61(b) (where the electron energy is given by V). Good agreement with the theoretical curves is seen. This provides an additional confirmation that the modeling of preheat-to-radiation ratio, in particular the neglect of scattering, is correct.

Using both Figs. 101.61(a) and 101.61(b) for the same molybdenum target shot, we derive the calibration of the HXR detector against the absolute energy of the Mo-Kα line. The resulting calibration, in units of x-ray energy per electrical charge of the time-integrated HXR signal, is $C = 0.018$ mJ/pC. This calibration factor depends weakly on the fast-electron temperature. To determine this dependence, we averaged the

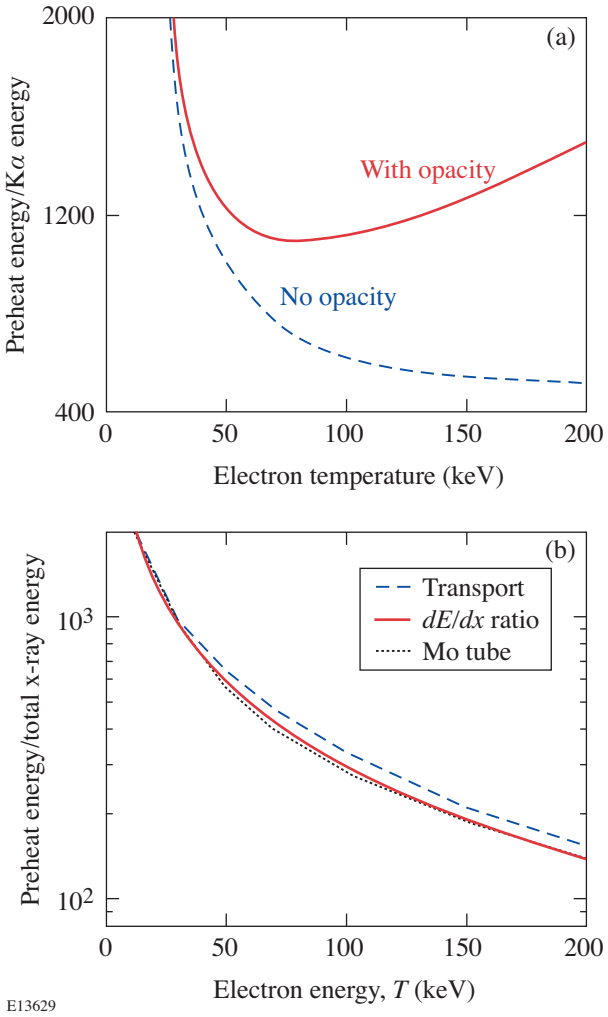

Figure 101.61
Calculations for a molybdenum target. (a) Ratio of preheat energy and emission energy in the Mo-Kα line, calculated by a multigroup electron transport through a molybdenum sphere. The curve marked "with opacity" includes the transport of the Kα line through the target. (b) The transport curve (dashed) and the dE/dx ratio curve (solid) are equivalent to the two curves in Fig. 101.59. The dotted curve is the inverse of the empirical x-ray efficiency of an x-ray tube with a Mo anode (the abscissa for the latter curve is given by the tube voltage).

relative detector sensitivity[18] over the HXR spectrum for each temperature. The uncertainty in the calibration factor is determined by that of the Kα energy, which is estimated to be ±20%. This adds to the effect of temperature uncertainty discussed above to yield a total uncertainty in the preheat of ±30%.

The final values of preheat as a fraction of the laser energy for the thick (27-μm) CH shells are shown as open circles in Fig. 101.62. Also shown as a solid circle marked "Mo" is the preheat in the CH-coated molybdenum target. In that case, the preheat energy can be equated with the initial energy in fast electrons that travel through the target since their range is much smaller than the radius of the molybdenum sphere and almost all the incident energy is converted to preheat. This energy can also be equated with the initial energy E_{init} in fast electrons that travel through a 27-μm-thick CH shell at the same irradiance ($I_0 = 7.7 \times 10^{14}$ W/cm^2) since, in the two cases, a laser of the same irradiance and pulse shape interacts with a spherical CH layer of the same radius. For the measured fast-electron temperature at irradiance I_0, the transport code calculates the fraction of E_{init} absorbed as preheat when an electron distribution of temperature T travels through a 27-μm-thick CH shell. The result is shown by the solid circle at the end of the arrow, and it agrees with the measured preheat for CH shells (i.e., it lies on the curve). This agreement indicates that the fast electrons traverse the shell only once, otherwise the point would lie below the curve. The possible reflection of electrons back into the target, due to a surrounding electric field, is an important factor in the study of fast-electron dynamics. The question of reflection, however, is not germane to the determination of the preheat level.

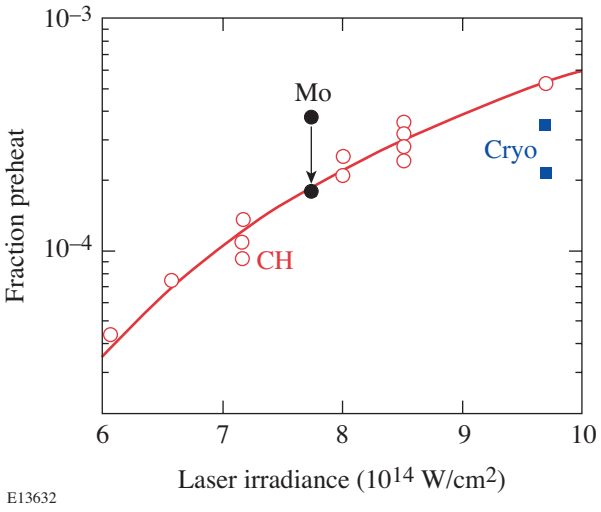

Figure 101.62
Preheat energy as a fraction of the incident laser energy deduced from the hard-x-ray measurements. Open circles: deuterium-gas–filled thick CH shells; point marked "Mo": CH-coated molybdenum sphere; solid squares: cryogenic-deuterium–filled CH shells. For the point at the end of the arrow see the text.

Preheat in Cryogenic Targets

A series of laser implosion experiments of cryogenic-deuterium targets were conducted recently and are described

in detail in Ref. 19. The preheat level for a few typical shots from this series was determined based on the HXR measured signals. The targets were ~3.5-μm-thick CH shells, filled with about 1000 atm of deuterium, which upon solidification yielded ~100-μm-thick solid deuterium layer on the inner surface of the CH shell. The laser energy was ~22.6 kJ in a 1-ns square pulse. Other details (target quality, etc.) are discussed in Ref. 19.

The determination of preheat in cryogenic targets is more involved than that for thick CH shells. First, because the cryogenic fuel is not cold, the formula for electron slowing down in a plasma rather than in a cold material must be used. Furthermore, most of the measured HXR signal is emitted by the CH layer, not the DD fuel. This is in spite of the fact that most of the electron slowing down occurs in the deuterium fuel. Therefore, to find the fraction of the HXR signal coming from the fuel, the successive transport of electrons through the CH and fuel layers is computed.

The slowing down of electrons in a plasma has two contributions: binary collisions and collective interactions (i.e., excitation of plasma waves). In the kinetic formulations of the problem, the division between the two regimes is marked by an impact parameter that is smaller or larger than the Debye length L_D. In the continuum (or dielectric) formulations of the problem, the division is marked by a density modulation wave number k that is larger or smaller than $k_D = 1/L_D$. The effect of the plasma ions is negligible for the high projectile velocities considered here.[20] The addition of the two electron collision terms for high projectile velocities yields[20]

$$(-dE/dx) = \left(2\pi e^4 N_e / E_0\right) \ln\left(1.52\ E_0/\hbar\omega_p\right),$$

where the plasma frequency is given by $\omega_p = \left(4\pi e^2 N_e/m\right)^{1/2}$. The Debye length dependence has canceled out because the argument of the logarithm in the binary-collision term is $\left(L_D/1.47 b_{\min}\right)$, where b is the impact parameter, whereas in the collective-collision term it is $\left(1.123\ V_0/\omega_p L_D\right)$, where V_0 is the projectile velocity; thus, by adding the two terms, the Debye length cancels out. This is an indication that the result is independent of the degree of degeneracy, which was also shown directly by Maynard and Deutsch.[21] The issue of using single-particle slowing-down formulas in this work was addressed in detail in the Appendix of Ref. 6; the main justification for neglecting collective effects is that the preheat is measured from HXR emission rather than deduced from the motion of the electrons that produce it. The result is very similar to the Bethe stopping-power formula[9] with the main difference being that the average ionization energy in the Bethe formula is replaced by $\hbar\omega_p$. For the deuterium fuel used in these experiments, the two equations yield very similar results.

The transport of electrons in these targets is calculated using the density profiles calculated by the one-dimensional (1-D) *LILAC* hydrodynamic code.[22] Throughout the laser pulse, the quarter-critical density surface (the region where the fast electrons are generated) remains within the CH layer. The fraction of the total HXR signal emitted by the deuterium fuel increases slightly during the laser pulse. The time-integrated HXR emission from the fuel is ~1/4 of the total HXR signal. The transport through the fuel layer can be used to generate preheat curves similar to those of Figs. 101.59 and 101.60(b), for various assumed fast-electron temperatures. Figure 101.63 shows the energy ratio of preheat and HXR computed for two instances during the laser pulse. The ratio is seen to change very little during the laser pulse. It also changes very little if the *LILAC* density profiles are replaced by constant-density profiles of the same total mass. Thus, because the preheat and HXR depend mostly on the areal density of material traversed (in addition to the number and spectrum of the fast electrons), the results are relatively insensitive to the precision of 1-D code simulations. Finally, the resulting preheat level for two cryogenic shots is shown as solid squares in Fig. 101.62. The results for all other cryogenic targets in this series (all at about the same laser irradiance) fall within the range spanned by

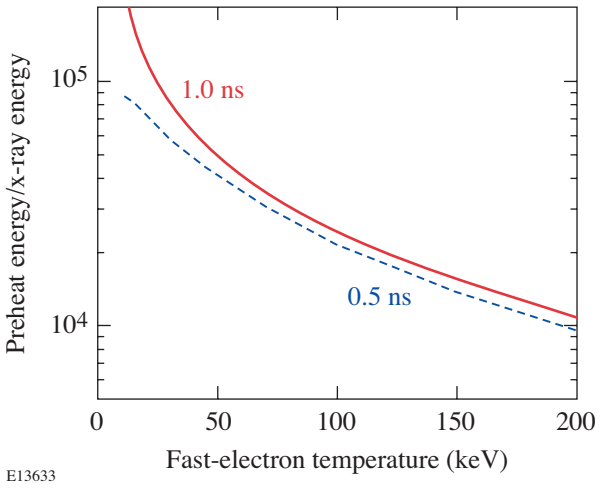

Figure 101.63
Calculated ratio of preheat energy and total hard-x-ray energy in the cryogenic-deuterium fuel. The electron transport code used the electron-density profiles calculated by *LILAC*. Shown is the ratio at two instances during the 1-ns laser pulse.

these two points. The preheat in the cryogenic fuel is smaller than that in the thick CH shells mainly because the electron areal density in the former is ~1/3 smaller than that in the latter.

As seen in Fig. 101.62, the preheat fraction is well below 0.1%. This indicates that preheat in these cryogenic target implosions will have a negligible impact on target performance. Since direct-drive target designs employ some shock preheating to reduce the growth of hydrodynamic instability (by adjusting the laser pulse shape), a reduction of the designed shock heating level could compensate for the preheat due to fast electrons. As explained in the introduction, these considerations are expected to hold equally for future direct-drive experiments on the NIF.

ACKNOWLEDGMENT

This work was supported by the U.S. Department of Energy Office of Inertial Confinement Fusion under Cooperative Agreement No. DE-FC52-92SF19460, the University of Rochester, and the New York State Energy Research and Development Authority. The support of the Department of Energy (DOE) does not constitute an endorsement by DOE of the views expressed in this article.

REFERENCES

1. J. D. Lindl, *Inertial Confinement Fusion: The Quest for Ignition and Energy Gain Using Indirect Drive* (Springer-Verlag, New York, 1998), Chap. 11.
2. P. W. McKenty, V. N. Goncharov, R. P. J. Town, S. Skupsky, R. Betti, and R. L. McCrory, Phys. Plasmas **8**, 2315 (2001).
3. Laboratory for Laser Energetics LLE Review **79**, 121, NTIS document No. DOE/SF/19460-317 (1999). Copies may be obtained from the National Technical Information Service, Springfield, VA 22161.
4. T. R. Boehly, R. S. Craxton, T. H. Hinterman, J. H. Kelly, T. J. Kessler, S. A. Kumpan, S. A. Letzring, R. L. McCrory, S. F. B. Morse, W. Seka, S. Skupsky, J. M. Soures, and C. P. Verdon, Rev. Sci. Instrum. **66**, 508 (1995).
5. C. Stoeckl, R. E. Bahr, B. Yaakobi, W. Seka, S. P. Regan, R. S. Craxton, J. A. Delettrez, R. W. Short, J. Myatt, A. V. Maximov, and H. Baldis, Phys. Rev. Lett. **90**, 235002 (2003).
6. B. Yaakobi, C. Stoeckl, T. Boehly, D. D. Meyerhofer, and W. Seka, Phys. Plasmas **7**, 3714 (2000).
7. A. B. Langdon, B. F. Lasinski, and W. L. Kruer, Phys. Rev. Lett. **43**, 133 (1979).
8. M. J. Berger, J. S. Coursey, and M. A. Zucker, *ESTAR*, *PSTAR*, and *ASTAR*: Computer Programs for Calculating Stopping-Power and Range Tables for Electrons, Protons, and Helium Ions (version 1.2.2). [Online] Available: http://physics.nist.gov/Star [2005, February 25]. National Institute of Standards and Technology, Gaithersburg, MD.
9. H. Bethe, Ann. Phys. **5**, 325 (1930); Z. Phys. **76**, 293 (1932).
10. R. M. Sternheimer, Phys. Rev. **88**, 851 (1952).
11. W. Heitler, *The Quantum Theory of Radiation*, 2nd ed., The International Series of Monographs on Physics (Oxford University Press, London, 1947).
12. A. J. Burek and B. Yaakobi, *Final Report to the National Bureau of Standards Contract* NB81NAHA2032, Appendix A, NTIS document No. DE83015439 (1983). Copies may be ordered from the National Technical Information Service, Springfield, VA 22161.
13. K. Toh, T. Ui, and E. Asada, in *Advances in X-Ray Analysis*, edited by C. S. Barrett, P. K. Predecki, and D. E. Leyden (Plenum Press, New York, 1985), Vol. 28, pp. 119–126.
14. J. V. Gilfrich, D. B. Brown, and P. G. Burkhalter, Appl. Spectrosc. **29**, 322 (1975).
15. B. L. Henke, E. M. Gullikson, and J. C. Davis, At. Data Nucl. Data Tables **54**, 181 (1993).
16. C. J. Powell, Rev. Mod. Phys. **48**, 33 (1976).
17. N. A. Dyson, *X-Rays in Atomic and Nuclear Physics*, 2nd ed. (Cambridge University Press, Cambridge, England, 1990), p. 47.
18. C. Stoeckl, V. Yu. Glebov, D. D. Meyerhofer, W. Seka, B. Yaakobi, R. P. J. Town, and J. D. Zuegel, Rev. Sci. Instrum. **72**, 1197 (2001).
19. P. W. McKenty, T. C. Sangster, M. Alexander, R. Betti, R. S. Craxton, J. A. Delettrez, L. Elasky, R. Epstein, A. Frank, V. Yu. Glebov, V. N. Goncharov, D. R. Harding, S. Jin, J. P. Knauer, R. L. Keck, S. J. Loucks, L. D. Lund, R. L. McCrory, F. J. Marshall, D. D. Meyerhofer, S. P. Regan, P. B. Radha, S. Roberts, W. Seka, S. Skupsky, V. A. Smalyuk, J. M. Soures, K. A. Thorp, M. Wozniak, J. A. Frenje, C. K. Li, R. D. Petrasso, F. H. Séguin, K. A. Fletcher, S. Padalino, C. Freeman, N. Izumi, J. A. Koch, R. A. Lerche, M. J. Moran, T. W. Phillips, G. J. Schmid, and C. Sorce, Phys. Plasmas **11**, 2790 (2004).
20. J. D. Jackson, *Classical Electrodynamics* (Wiley, New York, 1962).
21. G. Maynard and C. Deutsch, Phys. Rev. A, Gen. Phys. **26**, 665 (1982).
22. R. Epstein, S. Skupsky, and J. Delettrez, J. Quant. Spectrosc. Radiat. Transfer **35**, 131 (1986).

Publications and Conference Presentations

Publications

A. C. A. Chen, S. Culligan, Y. Geng, S. H. Chen, K. P. Klubek, K. M. Vaeth, and C. W. Tang, "Glassy Nematic Conjugated Oligomers: Materials for Organic Light-Emitting Diodes," in *Liquid Crystals VIII*, edited by I.-C. Khoo (SPIE, Bellingham, WA, 2004), Vol. 5518, pp. 77–91.

S. H. Chen, "Multifunctional Glassy Liquid Crystals for Photonics," J. SID **12**, 205 (2004).

R. Epstein, "On the Bell–Plesset Effects: The Effects of Uniform Compression and Geometrical Convergence on the Classical Rayleigh–Taylor Instability," Phys. Plasmas **11**, 5114 (2004).

S. Ghosh, R. Boni, and P. A. Jaanimagi, "Optical and X-Ray Streak Camera Gain Measurements," Rev. Sci. Instrum. **75**, 3956 (2004).

V. Yu. Glebov, C. Stoeckl, T. C. Sangster, S. Roberts, G. J. Schmid, R. A. Lerche, and M. J. Moran, "Prototypes of National Ignition Facility Neutron Time-of-Flight Detectors Tested on OMEGA," Rev. Sci. Instrum. **75**, 3559 (2004).

S. H. Glenzer, P. Arnold, G. Bardsley, R. L. Berger, G. Bonanno, T. Borger, D. E. Bower, M. Bowers, R. Bryant, S. Buckman, S. C. Burkhart, K. Campbell, M. P. Chrisp, B. I. Cohen, C. Constantin, F. Cooper, J. Cox, E. Dewald, L. Divol, S. Dixit, J. Duncan, D. Eder, J. Edwards, G. Erbert, B. Felker, J. Fornes, G. Frieders, D. H. Froula, S. D. Gardner, C. Gates, M. Gonzalez, S. Grace, G. Gregori, A. Greenwood, R. Griffith, T. Hall, B. A. Hammel, C. Haynam, G. Heestand, M. Henesian, G. Hermes, D. Hinkel, J. Holder, F. Holner, G. Holtmeier, W. Hsing, S. Huber, T. James, S. Johnson, O. S. Jones, D. Kalantar, J. H. Kamperschroer, R. Kauffman, T. Kelleher, J. Knight, R. K. Kirkwood, W. L. Kruer, W. Labiak, O. L. Landen, A. B. Langdon, S. Langer, D. Latray, A. Lee, F. D. Lee, D. Lund, B. MacGowan, S. Marshall, J. McBride, T. McCarville, L. McGrew, A. J. Mackinnon, S. Mahavandi, K. Manes, C. Marshall, J. Menapace, E. Mertens, N. Meezan, G. Miller, S. Montelongo, J. D. Moody, E. Moses, D. Munro, J. Murray, J. Neumann, M. Newton, E. Ng, C. Niemann, A. Nikitin, P. Opsahl, E. Padilla, T. Parham, G. Parrish, C. Petty, M. Polk, C. Powell, I. Reinbachs, V. Rekow, R. Rinnert, B. Riordan, M. Rhodes, V. Roberts, H. Robey, G. Ross, S. Sailors, R. Saunders, M. Schmitt, M. B. Schneider, S. Shiromizu, M. Spaeth, A. Stephens, B. Still, L. J. Suter, G. Teitbohl, M. Tobin, J. Tuck, B. M. Van Winterghem, R. Vidal, D. Voloshin, R. Wallace, P. Wegner, P. Whitman, E. A. Williams, K. Williams, K. Winward, K. Work, B. Young, P. E. Young, P. Zapata, R. E. Bahr, W. Seka, J. Fernandez, D. Montgomery, and H. Rose, "Progress in Long Scale Length Laser–Plasma Interactions," Nucl. Fusion **44**, S185 (2004).

V. N. Goncharov and G. Li, "Effect of Electric Fields on Electron Thermal Transport in Laser-Produced Plasmas," Phys. Plasmas **11**, 5680 (2004).

O. V. Gotchev, P. A. Jaanimagi, J. P. Knauer, F. J. Marshall, and D. D. Meyerhofer, "KB–PJX—A Streaked Imager Based on a Versatile X-Ray Microscope Coupled to a High-Current Streak Tube," Rev. Sci. Instrum. **75**, 4063 (2004) (invited).

P. A. Jaanimagi, "Breaking the 100-fs Barrier with a Streak Camera," in *Fourth-Generation X-Ray Sources and Ultrafast X-Ray Detectors*, edited by R. O. Tatchyn, Z. Chang, J.-C. Kieffer, and J. B. Hastings (SPIE, Bellingham, WA, 2004), Vol. 5194, pp. 171–182.

S. D. Jacobs, "International Innovations in Optical Finishing," in *Current Developments in Lens Design and Optical Engineering V*, edited by P. Z. Mouroulis, W. J. Smith, and R. B. Johnson (SPIE, Bellingham, WA, 2004), Vol. 5523, pp. 264–272 (invited).

S. D. Jacobs and E. Kowaluk, "Glass Art 'Sparkles' at OSA–OF&T's First Contest and Auction," OSA Focal Point Newsletter, Winter 2004.

J. P. Knauer and N. C. Gindele, "Temporal and Spectral Deconvolution of Data from Diamond, Photoconductive Devices," Rev. Sci. Instrum. **75**, 3714 (2004).

J. A. Koch, T. W. Barbee, Jr., S. Dalhed, S. Haan, N. Izumi, R. W. Lee, L. A. Welser, R. C. Mancini, F. J. Marshall, D. Meyerhofer, T. C. Sangster, V. A. Smalyuk, J. M. Soures, L. Klein, and I. Golovkin, "Core Temperature and Density Gradients in ICF," in *Atomic Processes in Plasmas: 14th APS Topical Conference on Atomic Processes in Plasmas*, edited by J. S. Cohen, S. Mazevet, and D. P. Kilcrease (American Institute of Physics, New York, 2004), pp. 53–60.

T. Z. Kosc, K. L. Marshall, A. Trajkovska-Petkoska, R. Varshneya, and S. D. Jacobs, "Development of Polymer Cholesteric Liquid Crystal Flakes for Electro-Optic Applications," Opt. Photonic News **15**, 33 (2004).

J.-C. Lin, M. Z. Yates, A. Trajkovska-Petkoska, and S. D. Jacobs, "Electric-Field–Driven Assembly of Oriented Molecular-Sieve Films," Adv. Mater. **16**, 1944 (2004).

F. J. Marshall, J. A. Oertel, and P. J. Walsh, "Framed, 16-Image, Kirkpatrick–Baez Microscope for Laser–Plasma X-Ray Emission," Rev. Sci. Instrum. **75**, 4045 (2004).

K. L. Marshall, E. Kimball, S. McNamara, T. Z. Kosc, A. Trajkovska-Petkoska, and S. D. Jacobs, "Electro-Optical Behavior of Polymer Cholesteric Liquid Crystal Flake/Fluid Suspensions in a Microencapsulation Matrix," in *Liquid Crystals VIII*, edited by I.-C. Khoo (SPIE, Bellingham, WA, 2004), Vol. 5518, pp. 170–181.

R. L. McCrory, "Recent Progress in Inertial Confinement Fusion in the United States," Nucl. Fusion **44**, S123 (2004).

C. Niemann, G. Antonini, S. Compton, S. H. Glenzer, D. Hargrove, J. D. Moody, R. K. Kirkwood, V. Rekow, J. Satariano, C. Sorce, W. Armstrong, R. Bahr, R. Keck, G. Pien, W. Seka, and K. Thorp, "Transmitted Laser Beam Diagnostic at the OMEGA Laser Facility," Rev. Sci. Instrum. **75**, 4171 (2004).

A. V. Okishev and J. D. Zuegel, "Highly Stable, All-Solid-State Nd:YLF Regenerative Amplifier," Appl. Opt. **43**, 6180 (2004).

R. Rey-de-Castro, D. Wang, X. Zheng, A. Verevkin, R. Sobolewski, M. Mikulics, R. Adam, P. Kordoš, and A. Mycielski, "Subpicosecond Faraday Effect in $Cd_{1-x}Mn_xTe$ and Its Application in Magneto-Optical Sampling," Appl. Phys. Lett. **85**, 3806 (2004).

J. Sanz, R. Betti, R. Ramis, and J. Ramírez, "Nonlinear Theory of the Ablative Rayleigh–Taylor Instability," Plasma Phys. Control. Fusion **46**, B367 (2004).

R. W. Short and A. Simon, "Theory of Three-Wave Parametric Instabilities in Inhomogeneous Plasmas Revisited," Phys. Plasmas **11**, 5335 (2004).

V. A. Smalyuk, V. N. Goncharov, T. R. Boehly, J. P. Knauer, D. D. Meyerhofer, and T. C. Sangster, "Self-Consistent Determination of Rayleigh–Taylor Growth Rates and Ablation-Front Density in Planar Targets Accelerated by Laser Light," Phys. Plasmas **11**, 5038 (2004).

C. Stoeckl, W. Theobald, T. C. Sangster, M. H. Key, P. Patel, B. B. Zhang, R. Clarke, S. Karsch, and P. Norreys, "Operation of a Single-Photon–Counting X-Ray Charge-Coupled Device Camera Spectrometer in a Petawatt Environment," Rev. Sci. Instrum. **75**, 3705 (2004).

L. Zheng, J. C. Lambropoulos, and A. W. Schmid, "UV-Laser-Induced Densification of Fused Silica: A Molecular Dynamics Study," J. Non-Cryst. Solids **347**, 144 (2004).

Forthcoming Publications

V. Bagnoud, "A Front End for Multipetawatt Lasers Based on a High-Energy, High-Average-Power Optical Parametric Chirped-Pulse Amplifier," to be published in Frontiers in Optics 2004.

V. Bagnoud, M. J. Guardalben, J. Puth, J. D. Zuegel, T. Mooney, and P. Dumas, "A High-Energy, High-Average-Power Laser Using Nd:YLF Laser Rods Corrected by MRF," to be published in Applied Optics.

C. Bouvier, J. C. Lambropoulos, and S. D. Jacobs, "Fracture Toughness of ULE, Zerodur, Astrosital, and Corning 9600," to be published in Frontiers in Optics 2004.

J. Carpenter and S. D. Jacobs, "The *Middle School* Science of Liquid Crystal Mood Patches," to be published in OE Magazine.

S. Costea, S. Pisana, N. P. Kherani, F. Gaspari, T. Kosteski, W. T. Shmayda, and S. Zukotynski, "The Use of Tritium in the Study of Defects in Amorphous Silicon," to be published in the Journal of Fusion Science and Technology.

R. S. Craxton and D. W. Jacobs-Perkins, "The Saturn Target for Polar Direct Drive on the National Ignition Facility," to be published in Physical Review Letters.

R. S. Craxton, F. J. Marshall, M. Bonino, R. Epstein, P. W. McKenty, S. Skupsky, J. A. Delettrez, I. V. Igumenshchev, D. W. Jacobs-Perkins, J. P. Knauer, J. A. Marozas, P. B. Radha, and W. Seka, "Polar Direct Drive—Proof-of-Principle Experiments on OMEGA and Prospects for Ignition on the NIF," to be published in Physics of Plasmas (invited).

J. E. DeGroote, S. N. Shafrir, J. C. Lambropoulos, and S. D. Jacobs, "Surface Characterization of CVD ZnS Using Power Spectral Density," to be published in Frontiers in Optics 2004.

V. Yu. Glebov, C. Stoeckl, T. C. Sangster, S. Roberts, and G. J. Schmid, "NIF Neutron Bang-Time Detector Prototype Test on OMEGA," to be published in IEEE Transactions on Plasma Science.

G. N. Gol'tsman, A. Korneev, I. Rubtsova, I. Milostnaya, G. Chulkova, O. Minaeva, K. Smirnov, B. Voronov, W. Slysz, A. Pearlman, A. Verevkin, and R. Sobolewski, "Ultrafast Superconducting Single-Photon Detectors for Near-Infrared-Wavelength Quantum Communications," to be published in Physica Status Solidi.

L. Guazzotto, R. Betti, J. Manickam, S. Kaye, and J. L. Gauvreau, "Magnetorheological Equilibria with Toroidal and Poloidal Flow," to be published in Physics of Plasmas (invited).

D. R. Harding, F.-Y. Tsai, E. L. Alfonso, S. H. Chen, A. K. Knight, and T. N. Blanton, "Properties of Vapor-Deposited Polyimide Films," to be published in the Journal of Adhesion Science and Technology (invited).

P. A. Jaanimagi, R. Boni, D. Butler, S. Ghosh, W. R. Donaldson, and R. L. Keck, "The Streak Camera Development Program at LLE," to be published in the Proceedings of SPIE.

S. D. Jacobs, "Innovations in Optics Manufacturing," to be published in Frontiers in Optics 2004 (invited).

J. Keck, J. B. Oliver, V. Gruschow, J. Spaulding, and J. D. Howe, "Process Tuning of Silica Thin-Film Deposition," to be published in Frontiers in Optics 2004.

J. Kitaygorsky, J. Zhang, A. Verevkin, A. Sergeev, A. Korneev, V. Matvienko, P. Kouminov, K. Smirnov, B. Voronov, G. Gol'tsman, and R. Sobolewski, "Origin of Dark Counts in Nanostructured NbN Single-Photon Detectors," to be published in IEEE Transactions on Applied Superconductivity.

J. P. Knauer, K. Anderson, P. B. Radha, R. Betti, T. J. B. Collins, V. N. Goncharov, P. W. McKenty, D. D. Meyerhofer, S. P. Regan, T. C. Sangster, and V. A. Smalyuk, "Improved Target Stability Using Picket Pulses to Increase and Shape the Ablator Adiabat," to be published in Physics of Plasmas (invited).

A. Korneev, V. Matvienko, O. Minaeva, I. Milostnaya, I. Rubtsova, G. Chulkova, K. Smirnov, V. Voronov, G. Gol'tsman, W. Slysz, A. Pearlman, A. Verevkin, and R. Sobolewski, "Quantum Efficiency and Noise Equivalent Power of Nanostructured, NbN, Single-Photon Detectors in the Wavelength Range from Visible to Infrared," to be published in IEEE Transactions on Applied Superconductivity.

T. Z. Kosc, K. L. Marshall, A. Trajkovska-Petkoska, E. Kimball, and S. D. Jacobs, "Progress in the Development of Polymer Cholesteric Liquid Crystal Flakes for Display Applications," to be published in the Journal of Displays.

T. Kosteski, N. P. Kherani, W. T. Shmayda, S. Costea, and S. Zukotynski, "Nuclear Batteries Using Tritium and Thin-Film Hydrogenated Amorphous Silicon," to be published in the Journal of Fusion Science and Technology.

I. A. Kozhinova, H. J. Romanofsky, and S. D. Jacobs, "Polishing of Prepolished CVD ZnS Flats with Altered Magnetorheological (MR) Fluids," to be published in Frontiers in Optics 2004.

J. C. Lambropoulos and R. Varshneya, "Glass Material Response to the Fabrication Process: Example from Lapping," to be published in Frontiers in Optics 2004.

X. Li, Y. Xu, Š□. Chromik, V. Štrbík, P. Odier, D. De Barros, and R. Sobolewski, "Time-Resolved Carrier Dynamics in Hg-Based High-Temperature Superconducting Photodetectors," to be published in IEEE Transactions on Applied Superconductivity.

J. R. Marciante, J. I. Hirsch, D. H. Raguin, and E. T. Prince, "Polarization-Insensitive, High-Dispersion TIR Diffraction Gratings," to be published in Frontiers in Optics 2004.

J. R. Marciante, J. I. Hirsch, D. H. Raguin, and E. T. Prince, "Polarization-Insensitive, High-Dispersion Total Internal Reflection Diffraction Gratings," to be published in the Journal of the Optical Society of America A.

A. E. Marino, K. Spencer, J. E. DeGroote, and S. D. Jacobs, "Chemical Durability of Phosphate Laser Glasses," to be published in Frontiers in Optics 2004.

F. J. Marshall, R. S. Craxton, J. A. Delettrez, D. H. Edgell, L. M. Elasky, R. Epstein, V. Yu. Glebov, V. N. Goncharov, D. R. Harding, R. Janezic, J. P. Knauer, P. W. McKenty, D. D. Meyerhofer, P. B. Radha, S. P. Regan, W. Seka, V. A. Smalyuk, C. Stoeckl, J. A. Frenje, C. K. Li, R. D. Petrasso, and F. H. Séguin, "Direct-Drive, Cryogenic Target Implosions on OMEGA," to be published in Physics of Plasmas (invited).

R. L. McCrory, S. P. Regan, R. Betti, T. R. Boehly, R. S. Craxton, T. J. B. Collins, J. A. Delettrez, R. Epstein, V. Yu. Glebov, V. N. Goncharov, D. R. Harding, R. L. Keck, J. P. Knauer, S. J. Loucks, J. Marciante, J. A. Marozas, F. J. Marshall, A. Maximov, P. W. McKenty, D. D. Meyerhofer, J. Myatt, P. B. Radha, T. C. Sangster, W. Seka, S. Skupsky, V. A. Smalyuk, J. M. Soures, C. Stoeckl, B. Yaakobi, J. D. Zuegel, C. K. Li, R. D. Petrasso, F. H. Séguin, J. A. Frenje, S. Padalino, C. Freeman, and K. Fletcher, "Direct-Drive Inertial Confinement Fusion Research at the Laboratory for Laser Energetics: Charting the Path to Thermonuclear Ignition," to be published in Nuclear Fusion.

F. H. Mrakovcic, J. A. Randi, J. C. Lambropoulos, and S. D. Jacobs, "Subsurface Damage in Single-Crystal Sapphire," to be published in Frontiers in Optics 2004.

J. B. Oliver, "Thin-Film-Optics Design and Manufacturing Challenges for Large-Aperture, High-Peak-Power, Short-Pulse Lasers," to be published in Frontiers in Optics 2004 (invited).

S. Papernov and A. W. Schmid, "High-Spatial-Resolution Studies of UV-Laser Damage Morphology in SiO_2 Thin Films with Artificial Defects," to be published in the Proceedings of XXXVI Annual Symposium on Optical Materials for High Power Lasers.

J.-R. Park, W. R. Donaldson, and R. Sobolewski, "Time-Resolved Imaging of a Spatially Modulated Laser Pulse," to be published in SPIE's Proceedings of LASE 2004.

A. Pearlman, A. Cross, W. Slysz, J. Zhang, A. Verevkin, M. Currie, A. Korneev, P. Kouminov, K. Smirnov, B. Voronov, G. Gol'tsman, and R. Sobolewski, "Gigahertz Counting Rates of NbN Single-Photon Detectors for Quantum Communications," to be published in IEEE Transactions on Applied Superconductivity.

P. B. Radha, T. J. B. Collins, J. A. Delettrez, Y. Elbaz, R. Epstein, V. Yu. Glebov, V. N. Goncharov, R. L. Keck, J. P. Knauer, J. A. Marozas, F. J. Marshall, R. L. McCrory, P. W. McKenty, D. D. Meyerhofer, S. P. Regan, T. C. Sangster, W. Seka, D. Shvarts, S. Skupsky, Y. Srebro, and C. Stoeckl, "Multidimensional Analysis of Direct-Drive Plastic-Shell Implosions on the OMEGA Laser," to be published in Physics of Plasmas (invited).

P. B. Radha, V. N. Goncharov, T. J. B. Collins, J. A. Delettrez, Y. Elbaz, V. Yu. Glebov, R. L. Keck, D. E. Keller, J. P. Knauer, J. A. Marozas, F. J. Marshall, P. W. McKenty, D. D. Meyerhofer, S. P. Regan, T. C. Sangster, D. Shvarts, S. Skupsky, Y. Srebro, R. P. J. Town, and C. Stoeckl, "Two-Dimensional Simulations of Plastic-Shell, Direct-Drive Implosions on OMEGA," to be published in Physics of Plasmas.

J. A. Randi, J. C. Lambropoulos, and S. D. Jacobs, "Subsurface Damage in Single Crystalline Optical Materials," to be published in Applied Optics.

S. P. Regan, J. A. Marozas, R. S. Craxton, J. H. Kelly, W. R. Donaldson, P. A. Jaanimagi, D. Jacobs-Perkins, R. L. Keck, T. J. Kessler, D. D. Meyerhofer, T. C. Sangster, W. Seka, V. A. Smalyuk, S. Skupsky, and J. D. Zuegel, "Performance of a 1-THz-Bandwidth, 2-D Smoothing by Spectral Dispersion and Polarization Smoothing of High-Power, Solid-State Laser Beams," to be published in the Journal of the Optical Society of America B.

S. P. Regan, T. C. Sangster, D. D. Meyerhofer, K. Anderson, R. Betti, T. R. Boehly, T. J. B. Collins, R. S. Craxton, J. A. Delettrez, R. Epstein, O. V. Gotchev, V. Yu. Glebov, V. N. Goncharov, D. R. Harding, P. A. Jaanimagi, J. P. Knauer, S. J. Loucks, L. D. Lund, J. A. Marozas, F. J. Marshall, R. L. McCrory, P. W. McKenty, S. F. B. Morse, P. B. Radha, W. Seka, S. Skupsky, H. Sawada, V. A. Smalyuk, J. M. Soures, C. Stoeckl, B. Yaakobi, J. A. Frenje, C. K. Li, R. D. Petrasso, and F. H. Séguin, "Direct-Drive Inertial Confinement Fusion Implosions on OMEGA," to be published in Astrophysics and Space Science.

R. Rey-de-Castro, D. Wang, A. Verevkin, A. Mycielski, and R. Sobolewski, "$Cd_{1-x}Mn_xTe$ Semimagnetic Semiconductors for Ultrafast Spintronics and Magneto-Optics," to be published in IEEE Transactions on Nanotechnology.

A. L. Rigatti, "Cleaning Process Versus Laser Damage Threshold of Coated Optical Components," to be published in Frontiers in Optics 2004.

S. N. Shafrir, J. C. Lambropoulos, and S. D. Jacobs, "Loose Abrasive Lapping of Optical Glass with Different Lapping Plates and Its Interpretation," to be published in Frontiers in Optics 2004.

A. Trajkovska-Petkoska, R. Varshneya, T. Z. Kosc, K. L. Marshall, and S. D. Jacobs, "Enhanced Electro-Optic Behavior for Shaped PCLC Flakes Made by Soft Lithography," to be published in Advanced Functional Materials.

D. Wang, A. Verevkin, R. Sobolewski, R. Adam, A. van der Hart, and R. Franchy, "Magneto-Optical Kerr Effect Measurements and Ultrafast Coherent Spin Dynamics in Co Nano-Dots," to be published in IEEE Transactions on Nanotechnology.

T. Yasuda, K. Fujita, T. Tsutsui, Y. Geng, S. W. Culligan, and S. H. Chen, "Carrier Transport Properties of Monodisperse Glassy-Nematic Oligofluorenes in Organic Field-Effect Transistors," to be published in Chemistry of Materials.

J. D. Zuegel, "Wavefront Correction Extends the Capabilities of Large-Aperture Nd:YLF Laser Rods," to be published in Laser Focus World.

Conference Presentations

The following presentations were made at the International Conference on Ultrahigh Intensity Lasers: Development, Science, and Emerging Applications, North Lake Tahoe, NV, 3–7 October 2004:

J. Bromage, J. D. Zuegel, D. Vickery, L. J. Waxer, D. Irwin, R. Boni, R. Jungquist, and C. Stoeckl, "High-Intensity Diagnostics for OMEGA EP."

T. J. Kessler, J. Bunkenburg, H. Hu, C. Kellogg, L. S. Iwan, and W. Skulski, "Design Strategies and Technology Demonstrations for the Tiled Grating Compressor."

A. W. Schmid, T. Z. Kosc, A. Kozlov, A. L. Rigatti, and J. B. Oliver, "A Short-Pulse, Laser-Damage Update on OMEGA EP."

C. Stoeckl, "OMEGA EP: A High-Energy Petawatt Laser at LLE."

J. D. Zuegel, V. Bagnoud, I. A. Begishev, M. J. Guardalben, and J. Puth, "Performance of the OMEGA EP's Prototype-OPCPA Front End."

J. R. Marciante, J. I. Hirsh, D. H. Raguin, and E. T. Prince, "Polarization-Insensitive, High-Dispersion TIR Diffraction Gratings," Diffractive Optics and Micro-Optics, Rochester, NY, 10–13 October 2004.

The following presentations were made at Optical Fabrication and Testing, Rochester, NY, 10–13 October 2004:

C. Bouvier, J. C. Lambropoulos, and S. D. Jacobs, "Fracture Toughness of ULE, Zerodur, Astrosital, and Corning 9600."

J. E. DeGroote, S. N. Shafrir, J. C. Lambropoulos, and S. D. Jacobs, "Surface Characterization of CVD ZnS Using Power Spectral Density."

S. D. Jacobs, "Innovations in Optics Manufacturing" (invited).

J. Keck, J. B. Oliver, V. Gruschow, J. Spaulding, and J. D. Howe, "Process Tuning of Silica Thin-Film Deposition."

I. A. Kozhinova, H. J. Romanofsky, and S. D. Jacobs, "Polishing of Prepolished CVD ZnS Flats with Altered Magnetorheological (MR) Fluids."

A. E. Marino, K. Spencer, J. E. DeGroote, and S. D. Jacobs, "Chemical Durability of Phosphate Laser Glasses."

F. H. Mrakovcic, J. A. Randi, J. C. Lambropoulos, and S. D. Jacobs, "Subsurface Damage in Single-Crystal Sapphire."

J. B. Oliver, "Thin-Film-Optics Design and Manufacturing Challenges for Large-Aperture, High-Peak-Power, Short-Pulse Lasers" (invited).

S. N. Shafrir, J. C. Lambropoulos, and S. D. Jacobs, "Loose Abrasive Lapping of Optical Glass with Different Lapping Plates and Its Interpretation."

The following presentations were made at Frontiers in Optics, The 88th Annual Meeting—Laser Science XX, Rochester, NY, 10–14 October 2004:

V. Bagnoud, "A Front End for Multipetawatt Lasers Based on a High-Energy, High-Average-Power Optical Parametric Chirped-Pulse Amplifier."

S. G. Lukishova, A. W. Schmid, C. M. Supranowitz, A. J. McNamara, R. W. Boyd, and C. R. Stroud, Jr., "Dye-Doped, Liquid-Crystal, Room-Temperature, Single-Photon Source."

D. D. Meyerhofer, "Progress in Direct-Drive Inertial Confinement Fusion" (invited).

B. Yaakobi, D. D. Meyerhofer, T. R. Boehly, J. J. Rehr, B. A. Remington, P. G. Allen, S. M. Pollaine, and R. C. Albers, "Dynamic EXAFS Probing of Laser-Driven Shock Waves and Crystal-Phase Transformations" (invited).

L. D. Merkle, M. Dubinskii, L. B. Glebov, L. N. Glebova, V. I. Smirnov, S. Papernov, and A. W. Schmid, "Photo-Thermo-Refractive Glass Resistance to Laser-Induced Damage Near One Micron," 7th Annual Directed Energy Symposium, Rockville, MD, 18–21 October 2004.

D. R. Harding, M. Bobeica, and R. Q. Gram, "Target Injection Studies," 10th High Average Power Laser Meeting, Princeton, NJ, 27–27 October 2004.

B. Yaakobi, "EXAFS Study of Laser-Shocked Metals," 11th International Workshop on Radiative Properties of Hot Dense Matter, Santa Barbara, CA, 1–5 November 2004.

R. L. McCrory, S. P. Regan, S. J. Loucks, D. D. Meyerhofer, S. Skupsky, R. Betti, T. R. Boehly, R. S. Craxton, T. J. B. Collins, J. A. Delettrez, D. H. Edgell, R. Epstein, V. Yu. Glebov, V. N. Goncharov, D. R. Harding, R. L. Keck, J. P. Knauer, J. Marciante, J. A. Maraozas, F. J. Marshall, A. V. Maximov, P. W. McKenty, J. Myatt, P. B. Radha, T. C. Sangster, W. Seka, V. A. Smalyuk, J. M. Soures, C. Stoeckl, B. Yaakobi, J. D. Zuegel, C. K. Li, R. D. Petrasso, F. H. Séguin, J. A. Frenje, S. Padalino, C. Freeman, and K. Fletcher, "Direct-Drive Inertial Confinement Fusion Research at the Laboratory for Laser Energetics: Charting the Path to Thermonuclear Ignition," 20th IAEA Fusion Energy Conference, Vilamoura, Portugal, 1–6 November 2004.

The following presentations were made at the 46th Annual Meeting of the APS Division of Plasma Physics, Savannah, GA, 15–19 November 2004:

K. Anderson, R. Betti, J. P. Knauer, V. A. Smalyuk, and V. N. Goncharov, "Simulations and Experiments on Adiabat Shaping by Relaxation."

R. Betti and J. Sanz, "Nonlinear Ablative Rayleigh–Taylor Instability."

T. R. Boehly, E. Vianello, J. E. Miller, R. S. Craxton, V. N. Goncharov, I. V. Igumenshchev, D. D. Meyerhofer, D. G. Hicks, and P. M. Celliers, "Direct-Drive Shock-Timing Experiments Using Planar Targets."

M. Canavan, J. A. Frenje, C. K. Li, C. Chen, J. L. DeCiantis, J. R. Rygg, F. H. Séguin, and R. D. Petrasso, "A Modified Accelerator for ICF Diagnostic Development."

C. Chen, C. K. Li, J. A. Frenje, F. H. Séguin, R. D. Petrasso, T. C. Sangster, R. Betti, D. R. Harding, and D. D. Meyerhofer, "Monte Carlo Simulations and Planned Experiments for Studying Hot-Electron Transport in H_2 and D_2."

T. J. B. Collins, S. Skupsky, A. Frank, A. Cunningham, and A. Poludnenko, "Shock Propagation in Wetted Foam."

R. S. Craxton, F. J. Marshall, M. J. Bonino, R. Epstein, P. W. McKenty, S. Skupsky, J. A. Delettrez, I. V. Igumenshchev, D. W. Jacobs-Perkins, J. P. Knauer, J. A. Marozas, P. B. Radha, and W. Seka, "Polar Direct Drive—Proof-of-Principle Experiments on OMEGA and Prospects for Ignition on the NIF" (invited).

J. L. DeCiantis, F. H. Séguin, J. A. Frenje, C. Chen, C. K. Li, R. D. Petrasso, J. A. Delettrez, J. P. Knauer, F. J. Marshall, D. D. Meyerhofer, S. Roberts, T. C. Sangster, and C. Stoeckl, "Studying the Burn Region in ICF Implosions with Proton Emission Imaging."

J. A. Delettrez, S. Skupsky, C. Stoeckl, J. Myatt, and P. B. Radha, "Simulation of Enhanced Neutron Production for OMEGA EP Cryogenic Implosions."

D. H. Edgell, W. Seka, R. S. Craxton, L. M. Elasky, D. R. Harding, R. L. Keck, M. Pandina, M. D. Wittman, and A. Warrick, "Shadowgraphic Analysis Techniques for Cryogenic Ice-Layer Characterization at LLE."

D. H. Edgell, W. Seka, R. S. Craxton, L. M. Elasky, D. R. Harding, R. L. Keck, M. Pandina, M. D. Wittman, and A. Warrick, "Three-Dimensional Characterization of Ice Layers for Cryogenic Targets at LLE."

R. Epstein, R. S. Craxton, J. A. Delettrez, F. J. Marshall, J. A. Marozas, P. W. McKenty, P. B. Radha, and V. A. Smalyuk, "Simulations of X-Ray Core Images from OMEGA Implosions Driven with Controlled Polar Illumination."

J. A. Frenje, C. K. Li, F. H. Séguin, J. L. DeCiantis, J. R. Rygg, M. Falk, R. D. Petrasso, J. A. Delettrez, V. Yu. Glebov, C. Stoeckl, F. J. Marshall, D. D. Meyerhofer, T. C. Sangster, V. A. Smalyuk, and J. M. Soures, "Measurements of Time Evolution of Ion Temperature of D^3He Implosions on OMEGA."

M. C. Ghilea, D. D. Meyerhofer, T. C. Sangster, R. A. Lerche, and L. Disdier, "First Results from a Penumbral Imaging System Design Tool."

V. Yu. Glebov, C. Stoeckl, T. C. Sangster, C. Mileham, S. Roberts, and R. A. Lerche, "NIF Neutron Bang-Time Detector Development on OMEGA."

V. N. Goncharov, D. Li, and A. V. Maximov, "Effects of the Ponderomotive Terms in the Thermal Transport on the Hydrodynamic Flow in Inertial Confinement Fusion Experiments."

O. V. Gotchev, T. J. B. Collins, V. N. Goncharov, J. P. Knauer, D. Li, and D. D. Meyerhofer, "Mass Ablation Rate and Self-Emission Measurements in Planar Experiments."

L. Guazzotto, R. Betti, J. Manickam, S. Kaye, and J. L. Gauvreau, "Magnetorheological Equilibria with Toroidal and Poloidal Flow" (invited).

D. R. Harding, M. D. Wittman, L. M. Elasky, S. Verbridge, L. D. Lund, D. Jacobs-Perkins, W. Seka, D. H. Edgell, and D. D. Meyerhofer, "OMEGA Direct-Drive Cryogenic Deuterium Targets."

I. V. Igumenshchev, "The Role of Viscosity in Simulations of Strong Shocks in Low-Density Foams."

P. A. Jaanimagi, R. Boni, R. L. Keck, W. R. Donaldson, and D. D. Meyerhofer, "The Rochester Optical Streak System."

J. P. Knauer, K. Anderson, P. B. Radha, R. Betti, T. J. B. Collins, V. N. Goncharov, P. W. McKenty, D. D. Meyerhofer, S. P. Regan, T. C. Sangster, and V. A. Smalyuk, "Improved Target Stability Using Picket Pulses to Increase and Shape the Ablator Adiabat" (invited).

C. K. Li, C. Chen, J. A. Frenje, F. H. Séguin, R. D. Petrasso, J. A. Delettrez, R. Betti, D. D. Meyerhofer, J. Myatt, and S. Skupsky, "Linear-Energy Transfer and Blooming of Directed Energetic Electrons in Dense Hydrogenic Plasmas."

D. Li and V. N. Goncharov, "Effects of the Temporal Density Variation and Convergent Geometry on Nonlinear Bubble Evolution in Classical Rayleigh–Taylor Instability."

G. Li and V. N. Goncharov, "The Effect of Electromagnetic Fields on Electron-Thermal Transport in Laser-Produced Plasmas."

J. A. Marozas, P. B. Radha, T. J. B. Collins, P. W. McKenty, and S. Skupsky, "Evolution of the Laser-Deposition Region in Polar-Direct-Drive Simulations on the National Ignition Facility (NIF)."

F. J. Marshall, R. S. Craxton, J. A. Delettrez, D. H. Edgell, L. M. Elasky, R. Epstein, V. Yu. Glebov, V. N. Goncharov, D. R. Harding, R. Janezic, J. P. Knauer, P. W. McKenty, D. D. Meyerhofer, P. B. Radha, S. P. Regan, W. Seka, V. A. Smalyuk, C. Stoeckl, J. A. Frenje, C. K. Li, R. D. Petrasso, and F. H. Séguin, "High-Performance, Direct-Drive, Cryogenic Target Implosions on OMEGA" (invited).

A. V. Maximov, J. Myatt, R. W. Short, W. Seka, and C. Stoeckl, "Two-Plasmon-Decay Instability in Plasmas Irradiated by Incoherent Laser Beams."

D. D. Meyerhofer, B. Yaakobi, T. R. Boehly, T. J. B. Collins, H. Lorenzana, B. A. Remington, P. G. Allen, S. M. Pollaine, J. J. Rehr, and R. C. Albers, "Dynamic EXAFS Probing of Laser-Driven Shock Waves and Crystal Phase Transformations."

J. E. Miller, W. J. Armstrong, T. R. Boehly, D. D. Meyerhofer, W. Theobald, E. Vianello, J. Eggert, D. G. Hicks, and C. Sorce, "Time-Resolved Measurement of Optical Self-Emission for Shock Wave and Equation of State Studies."

J. Myatt, A. V. Maximov, R. W. Short, J. A. Delettrez, and C. Stoeckl, "Numerical Studies of MeV Electron Transport in Fast-Ignition Targets."

P. B. Radha, T. J. B. Collins, J. A. Delettrez, Y. Elbaz, R. Epstein, V. Yu. Glebov, V. N. Goncharov, R. L. Keck, J. P. Knauer, J. A. Marozas, F. J. Marshall, R. L. McCrory, P. W. McKenty, D. D. Meyerhofer, S. P. Regan, T. C. Sangster, W. Seka, D. Shvarts, S. Skupsky, Y. Srebro, and C. Stoeckl, "Multidimensional Analysis of Direct-Drive Plastic-Shell Implosions on OMEGA" (invited).

S. P. Regan, J. A. Delettrez, V. Yu. Glebov, V. N. Goncharov, J. A. Marozas, F. J. Marshall, P. W. McKenty, D. D. Meyerhofer, P. B. Radha, T. C. Sangster, V. A. Smalyuk, C. Stoeckl, J. A. Frenje, C. K. Li, R. D. Petrasso, and F. H. Séguin, "Experimental Investigation of the Effects of Irradiation Nonuniformities on the Performance of Direct-Drive Spherical Implosions."

J. R. Rygg, F. H. Séguin, C. K. Li, J. A. Frenje, J. L. DeCiantis, R. D. Petrasso, J. A. Delettrez, V. N. Goncharov, P. B. Radha, V. Yu. Glebov, D. D. Meyerhofer, and T. C. Sangster, "Inference of Imprint at Onset of Deceleration Phase Using Shock-Burn Measurements."

T. C. Sangster, J. A. Delettrez, V. Yu. Glebov, V. N. Goncharov, D. R. Harding, J. P. Knauer, F. J. Marshall, P. W. McKenty, D. D. Meyerhofer, P. B. Radha, S. P. Regan, S. Skupsky, V. A. Smalyuk, C. Stoeckl, J. A. Frenje, C. K. Li, R. D. Petrasso, and F. H. Séguin, "High-Areal-Density Cryogenic D_2 Implosions on OMEGA."

H. Sawada, S. P. Regan, T. R. Boehly, I. V. Igumenshchev, V. N. Goncharov, F. J. Marshall, B. Yaakobi, T. C. Sangster, D. D. Meyerhofer, D. Gregori, D. G. Hicks, S. G. Glenzer, and O. L. Landen, "Diagnosing Shock-Heated, Direct-Drive Plastic Targets with Spectrally Resolved X-Ray Scattering."

F. H. Séguin, J. L. DeCiantis, J. A. Frenje, C. K. Li, J. R. Rygg, C. Chen, R. D. Petrasso, V. A. Smalyuk, F. J. Marshall, J. A. Delettrez, J. P. Knauer, P. W. McKenty, D. D. Meyerhofer, S. Roberts, T. C. Sangster, K. Mikaleian, and H. S. Park, "Relationship of Asymmetries in Fusion Burn and ρR to Asymmetries in Laser Drive for ICF Implosions at OMEGA."

W. Seka, C. Stoeckl, V. N. Goncharov, R. E. Bahr, T. C. Sangster, R. S. Craxton, J. A. Delettrez, A. V. Maximov, J. Myatt, A. Simon, and R. W. Short, "Absorption Measurements in Spherical Implosions on OMEGA."

R. W. Short, "Convective Versus Absolute Two-Plasmon Decay in Inhomogeneous Plasmas."

V. A. Smalyuk, V. N. Goncharov, T. R. Boehly, D. Li, J. A. Marozas, D. D. Meyerhofer, S. P. Regan, and T. C. Sangster, "Measurements of Imprinting with Laser Beams at Various Angles of Incidence in Planar CH Foils."

J. M. Soures, F. J. Marshall, J. A. Delettrez, R. Epstein, R. Forties, V. Yu. Glebov, J. H. Kelly, T. J. Kessler, J. P. Knauer, P. W. McKenty, S. P. Regan, W. Seka, V. A. Smalyuk, C. Stoeckl, J. A. Frenje, C. K. Li, R. D. Petrasso, and F. H. Séguin, "Polar-Direct-Drive Experiments on OMEGA."

C. Stoeckl, W. Theobald, J. A. Delettrez, J. Myatt, S. P. Regan, H. Sawada, T. C. Sangster, M. H. Key, P. Patel, R. Snavely, R. Clarke, S. Karsch, and P. Norreys, "*K*-Shell Spectroscopy Using a Single-Photon–Counting X-Ray CCD in Ultrafast Laser–Plasma Interaction Experiments."

S. Sublett, J. P. Knauer, I. V. Igumenshchev, D. D. Meyerhofer, A. Frank, P. A. Keiter, R. F. Coker, B. H. Wilde, B. E. Blue, T. S. Perry, J. M. Foster, and P. A. Rosen, "Hydrodynamic Jet Experiments on OMEGA."

W. Theobald, C. Stoeckl, T. C. Sangster, J. Kuba, R. Snavely, M. H. Key, R. Heathcoate, D. Neely, and P. Norreys, "X-Ray Line Emission Spectroscopy of 100-TW-Laser-Pulse–Generated Plasmas for Backlighter Development of Cryogenic Implosion Capsules."

E. Vianello, T. R. Boehly, R. S. Craxton, V. N. Goncharov, J. E. Miller, I. V. Igumenshchev, D. D. Meyerhofer, T. C. Sangster, D. G. Hicks, and P. M. Celliers, "The Effect of Incidence Angle on Laser-Driven Shock Strengths."

C. Zhou, J. Sanz, and R. Betti, "Asymptotic Bubble Evolution in the Bell–Plesset and Ablative Rayleigh–Taylor Instabilities."

C. W. Wu and D. R. Harding, "Growth of the Open-Networked Carbon Nanostructures at Low Temperature by Microwave Plasma Electron Cyclotron Resonance Chemical Vapor Deposition," 2004 MRS Fall Meeting, Boston, MA, 29 November–3 December 2004.

S. G. Lukishova, A. W. Schmid, R. S. Knox, P. Freivald, R. W. Boyd, and C. R. Stroud, Jr., "Deterministically Polarized Single-Photon Source," Quantum Optics II, Cozumel, Mexico, 6–9 December 2004.

UNIVERSITY OF
ROCHESTER